

DOCTORAL DISSERTATION

**Investigating hydrodynamics of a mesotidal delta
channel network using advanced hydro acoustic
systems**

(高度水中音響システムを用いた中規模デルタ河川ネット
ワークの流体力学に関する調査研究)

September 2021

Department of Civil and Environmental Engineering
Graduate School of Engineering
Hiroshima University

XIAO CONG

Acknowledgements

The members of my supervisory committee deserve the best accolades and my deepest thanks for their expertise, encouragement, and support. First, I would like to thank my supervisor, Prof. Kawanisi, for with his excellent guidance, support, and patience during my doctoral studies at Hiroshima University.

During the last three years, I experienced a well research environment at Hiroshima University. I would like to thank Nakashita sensei for his help in the laboratory; Dr. Mohamad Basel Al Sawaf for his wonderful support during my field experiment and writing paper. I also thank Kaneto, Torigoe, Mori, Guo, Meddy, Hiep, Faruq, and Gillang for their helps. I also thank Prof. Arata Kaneko, Dr. Chuanzheng Zhang and Dr. Minmo Chen for their sharing knowledge in the acoustic tomography field.

In this opportunity, I would like to thank the China Scholarship Council (CSC) for supporting my doctoral program at Hiroshima University.

Finally, I would like to thank my family, my parents for their nonstop support in their entire life for me. I am particularly grateful to Yuan Yu; I am grateful to you that joined my life here. In death or life or separated or far apart, with you I made an agreement: I grasped your hand, together with you I was to grow old.

XIAO CONG

Hiroshima University, Japan

Tables of Contents

ACKNOWLEDGEMENTS	I
TABLES OF CONTENTS.....	I
LIST OF SYMBOLS	I
LIST OF ABBREVIATIONS	I
LIST OF FIGURES	I
LIST OF TABLES	I
ABSTRACT	I
CHAPTER 1: INTRODUCTION	1
1.1 Study overview	1
1.2 Literature Reviews	2
1.2.1 Interactions between river flow and tide on suspended particulate matter (SPM) dynamics	2
1.2.2 Interactions between river flow and tide on hydrodynamics	3
1.2.2 Interactions between river flow and tide on salinity dynamics	5
1.3 Research Motivations and objectives.....	5
1.4 Research methods.....	7
1.4.1 Instruments and methods	7
1.5 Research outline of the thesis	9
CHAPTER 2: SUSPENDED PARTICULATE MATTER CONCENTRATION IN RESPONSE TO TIDAL HYDRODYNAMICS IN THE OTAGAWA FLOODWAY.....	11
2.1. Introduction.....	11
2.2. Materials and methods.....	13
2.2.1 Study area.....	13
2.2.2 Instruments and methods	14
2.3. Results.....	16
2.3.1 Hydrodynamic characteristics in the Otagawa floodway ...	16
2.3.2 In-situ suspended particulate matter concentration variations and sediment size distributions	18
2.3.3 SSA results and Fast Fourier Transform (FFT) test.....	21
2.3.4 Spring-neap tidal cycle	26
2.3.5 Relationship between SPMC and water discharge	31
2.4. Discussion	34

2.4.1 Role of tidal velocity and water discharge	34
2.4.2 Capture depocenter	36
2.4.3 Occurrence of convergence zone (CZ) in the tidal floodway	38
2.5. Conclusions	40
CHAPTER 3: MAPPING TIDAL CURRENTS AT A SHALLOW TIDAL CHANNEL JUNCTION USING THE FLUVIAL ACOUSTIC TOMOGRAPHY SYSTEM.....	42
3.1. Introduction	42
3.2. Study area and methods.....	44
3.2.1 Study area.....	44
3.2.2 Instruments	45
3.2.3 Theoretical analysis of the inverse method	47
3.3. Results.....	49
3.3.1 Ray simulation results	49
3.3.2 Inverse results.....	53
3.3.3 2D residual currents and tidal ellipse distributions.....	56
3.4. Discussion	59
3.4.1 Comparisons of FAT vs. ADCP and FAT vs. CT/CTD results	59
3.4.2 Evaluation of the inverse results	64
3.4.3 River-tide interactions at the junction	67
3.4.4 2D current dynamics at the junction	70
3.5. Conclusions.....	72
CHAPTER 4: MAPPING SALINITY DISTRIBUTION AT A SHALLOW TIDAL CHANNEL JUNCTION USING THE FLUVIAL ACOUSTIC TOMOGRAPHY SYSTEM	74
4.1. Introduction.....	74
4.2. Study area and methods.....	75
4.2.1 Study area.....	75
4.2.2 Instruments and Methods.....	76
4.3. Theoretical analysis	77
4.3.1 Forward problem	77
4.3.2 Inverse problem of 2D salinity fields.....	77
4.4. Results.....	80
4.4.1 Range averaged salinity	80
4.4.2 2D salinity distributions.....	81

4.4.3 Temporal salinity variations at the junction	83
4.5. Discussions	85
4.5.1 Evaluation of the inversion results	85
4.5.2 Advection of salinity at the junction	89
4.5.3 Comparison of other estuaries	91
4.6. Conclusions.....	92
CHAPTER 5: CONTINUOUS MEASUREMENTS OF TIDAL DISCHARGE AT A SHALLOW TIDAL CHANNEL JUNCTION USING THE FLUVIAL ACOUSTIC TOMOGRAPHY SYSTEM	93
5.1. Introduction.....	93
5.2. Theoretical analysis.....	94
5.3. Results and discussion.....	95
5.3.1 Cross-sectional average velocity.....	95
5.3.2 Temporal variations of the flow direction	96
5.3.3 Temporal variations of the tidal discharge	97
5.4. Conclusions.....	99
CHAPTER 6: CONCLUSIONS AND FUTURE WORKS.....	100
6.1 Main conclusions	100
6.2 Answers for the research questions.....	102
6.3 Future work.....	102
APPENDIX.....	104
REFERENCES.....	105

List of Symbols

Symbols	
Q	Discharge (m ³ /s)
C_d	Drag coefficient
H	Water level (m)
ω	Tidal frequency
S_0	Reference salinity (psu)
g	Gravitational acceleration (m/s ²)
ρ_0	Reference density (kg/m ³)
M	Mixing indicator
T.P. m	Height above the mean sea level in Tokyo Bay
C_m	Mean sound speed (m/s)
δC	Sound speed deviation relative to C_m (m/s)
ds	Increment of the arc length along the ray
ΔR	Spatial resolution of inverse analysis (m)
A	Tomography area (m ²)
T	Temperature (°C)
S	Salinity (psu)
D	Depth (m)
Δt_i	Difference of travel time (s)
δt	Summation of travel time (s)

List of Abbreviations

Abbreviations	
SPM	Suspended Particulate Matter
SPMC	Suspended Particulate Matter Concentration
ETM	Estuary Turbidity Maximum
SSA	Singular Spectrum Analysis
RC	Reconstructed Component
TKE	Turbulence Kinetic Energy
CTD	Conductivity Temperature Depth
CT	Conductivity Temperature
FFT	Fast Fourier Transform
ADCP	Acoustic Doppler Current Profiler
FAT	Fluvial Acoustic Tomography
CAT	Coastal Acoustic Tomography
CZ	Convergence Zone
HG	Hydraulic Geometry
RE	Relative Error
MRE	Mean Relative Error
RMSE	Root Mean Square Error
RMSD	Root Mean Square Difference
mab	above the bottom
SS	Skill Score

List of Figures

- Figure 2.1** Research area and observation sites along the Otagawa floodway, Hiroshima City, Japan.....14
- Figure 2.2** Hydrodynamic data during summer at Sta. A_R from July 29 to August 16, 2007. Temporal variations in (a) river discharge at Yaguchi gauging station, (b) water depth, (c) salinity, (d) water temperature, and (e) velocity. The red and blue values indicate the flood and ebb velocities, respectively. The compact-CTD was deployed two times, firstly from July 29 to August 2 and then from August 10 to 16. The Yaguchi gauging station is located around 14.6 km from the river mouth.....17
- Figure 2.3** Hydrodynamic data during winter at Sta. A_C from January 6 to 26, 2008. Temporal variations in (a) river discharge at Yaguchi gauging station, (b) water depth, (c) salinity, (d) water temperature, and (e) velocity. The red and blue values indicate the flood and ebb velocities, respectively. The Yaguchi gauging station is located around 14.6 km from the river mouth.....18
- Figure 2.4** Depth-averaged SPMC time series and wind along the Otagawa floodway: (a) during summer at Sta. A_R from July 29 to August 16, 2007, (b) during winter at Sta. A_C from January 6 to 26, 2008, (c) during winter at Sta. B from December 22, 2007 to January 16, 2008, and (d) during winter at Sta. C from December 27, 2007 to January 10, 2008. Tidal range from Kusatsu gauging station during (e) summer and (f) winter. The shaded regions represent the spring/neap periods.....20
- Figure 2.5** Grain size variations along the Otagawa floodway.....21
- Figure 2.6** RC contributions to four SPMC time series: during summer at Sta. A_R from July 29 to August 16, 2007; during winter at Sta. A_C from January 6 to 26, 2008; during winter at Sta. B from December 22, 2007 to January 16, 2008; during winter at Sta. C from December 27, 2007 to January 10, 2008.....22

Figure 2.7 Comparisons of RCs to the temporal changes of the variables at Sta. A_R: (a) RC1 vs. velocity (the red line represents the envelope of the velocity and the gray line represents the original magnitude of the velocity), (b) RC2 vs. water depth, (c) RC2 vs. velocity, (d) regression diagram of RC1 and velocity amplitude, (e) regression diagram of RC2 and water depth, and (f) regression diagram of RC2 and velocity.....23

Figure 2.8 Comparisons of RCs to the temporal changes of the variables at Sta. A_C: (a) RC1 vs. velocity (the red line represents the envelope of the velocity and the gray line represents the original magnitude of the velocity), (b) RC2 vs. water depth, (c) RC2 vs. velocity, (d) regression diagram of RC1 and velocity amplitude, (e) regression diagram of RC2 and water depth, and (f) regression diagram of RC2 and velocity.....24

Figure 2.9 Comparisons of the RCs to the temporal changes in the variables at Stations B and C, including: (a) at Station B RC1 vs. velocity (the red line represents the envelope of the velocity and the gray line represents the original velocity), (b) at Station C RC1 vs. velocity (the red line represents the envelope of the velocity and the gray line represents the original velocity).....25

Figure 2.10 FFT power spectra of the original depth average SPMC time series.....26

Figure 2.11 Temporal variations of the velocity profiles (positive indicates flood, upstream), SPMC, and M at Sta. A_R in summer and Sta. A_C in winter during spring and neap tide. (a) Velocity, (b) SPMC, and (c) M during spring tide at Sta. A_R. (d) Velocity and (e) SPMC during neap tide at Sta. A_R. (f) Velocity, (g) SPMC, and (h) M during spring tide at Sta. A_C. (i) Velocity, (j) SPMC, and (k) M during neap tide at Sta. A_C.....29

Figure 2.12 Temporal variations of the velocity profile (positive indicates flood, upstream) and SPMC, including (a) velocity and (b) SPMC at Station B during spring tide, (c) velocity and (d) SPMC at Station C during spring tide, (e) velocity and (f) SPMC at Station B during neap tide, and (g)

velocity and (h) SPMC at Station C during neap tide.....30

Figure 2.13 (a)–(d) Scatter diagrams of SPMC and water discharge within three layers; (e)–(h) SPMC cumulative flux in three layers: (a) and (e) during summer at Sta. A_R from July 29 to August 16, 2007; (b) and (f) during winter at Sta. A_C from January 6 to 26, 2008; (c) and (g) during winter at Station B from December 22, 2007 to January 16, 2008; (d) and (h) during winter at Station C from December 27, 2007 to January 10, 2008 (positive: upstream direction, landward; negative: downstream direction, seaward).....32

Figure 2.14 Comparison of SPMC cumulative flux at Stations A, B, and C during January 7–10, 2008.....33

Figure 2.15 Bottom tidal velocity vs. water discharge and SPMC for three stations during spring/neap tide period during winter and distribution of spring/neap tidal averaged bottom layer SPMC vs. tidal range at three stations during winter.....37

Figure 2.16 Mean (red cross), median (red bars), 25–75th percentile (blue bars), and 9–91st percentile (black bars) values of each layer-average SPMC (bottom, middle, and surface) in 20 m³/s intervals of water discharge at Station A.....39

Figure 3.1 (a) Ota River; (b) bathymetry at the junction; and (c) locations of the fluvial acoustic tomography (FAT) system stations (S1-S6; black dots) and fixed Acoustic Doppler Current Profiler (ADCP; red dots) stations. Acoustic paths among the FAT stations are denoted by solid black lines. The unit T.P. m is the depth with respect to the mean water level in Tokyo Bay.....45

Figure 3.2 Synchronized fluvial acoustic tomography (FAT) system and Acoustic Doppler Current Profiler (ADCP) measurements: (a) Water level data (monitored at the Misasa gauging station) and precipitation data (acquired from the Japan Meteorological Agency); (b) observation periods of the fixed ADCP and time schedules of the successful percentages of

reciprocal sound transmission between each settled station pair. The shaded regions represent the spring/neap periods during the observation period..47

Figure 3.3 (a) Typical water temperature, salinity, and calculated sound speed profiles with a salt wedge at high water. (b)–(d) and (e)–(g) display the results (source angle, arrival time, and ray length) of ray tracing along the shortest and longest transmission lines, S1–S2 and S3–S6, respectively. 51

Figure 3.4 (a) Typical water temperature, salinity, and calculated sound speed profiles without a salt wedge at low water. (b)–(d) and (e)–(g) display the results (source angle, arrival time, ray length) of ray tracing along the shortest and longest transmission lines, S1–S2 and S3–S6, respectively..52

Figure 3.5 (a) Results of ray tracing when transducers are installed at the depth of the salt wedge for the longest station pairs (S3-S6), (b) source angle (deg) and arrival time (ms), (c) source angle (deg) and length of each ray (m). The sound speed profile is identical to that shown in Figure 3.3a. 53

Figure 3.6 Depth-averaged currents and salinity distributions for two semi-diurnal tide cycle during spring tide. The black and red arrows represent the velocities acquired by the fluvial acoustic tomography (FAT) system and the Acoustic Doppler Current Profiler (ADCP), respectively. The FAT stations are marked by black dots, and the actual acoustic transmission rays among the FAT stations are connected by solid lines. The tidal phase of each sub-figure is indicated by a black dot on the water level in the lower right corner.....54

Figure 3.7 Depth-averaged currents and salinity distributions for two semi-diurnal tide cycles during a neap tide. Black and red arrows represent the velocities acquired by the fluvial acoustic tomography (FAT) system and Acoustic Doppler Current Profiler (ADCP), respectively. FAT stations are marked by black dots, and the actual acoustic transmission rays among the FAT stations are connected by solid lines. The tidal phase of each sub-figure is indicated by a black dot on the water level.....56

Figure 3.8 Distribution of tidal ellipses for five tidal constituents obtained by harmonic analysis during the whole observation period, (a) O_1 , (b) K_1 , (c) M_2 , (d) M_4 , (e) MS_f ; and (f) the residual currents. The black arrows and ellipses are from FAT results, and the red arrow and ellipse indicate the Acoustic Doppler Current Profiler (ADCP) results.....58

Figure 3.9 Distributions of tidal ellipses for M_2 and M_4 tidal constituents, and the residual currents during spring (a–c) and neap (d–f) tides corresponding to the current distributions shown in Figures 4 and 5. The black arrows and ellipses are from FAT results, and the red arrow and ellipse indicate the Acoustic Doppler Current Profiler (ADCP) results.....58

Figure 3.10 Relationships between fluvial acoustic tomography (FAT) system and station 1 Acoustic Doppler Current Profiler (S1-ADCP): (a) and (c) eastward; (b) and (d) northward velocity components. The red, black, and grey dashed lines denote the fitting line, the 1:1 line, and the 20% relative error line, respectively. The skill score (SS), the root mean squares difference (RMSD), and the mean relative error (MRE) are given at each panel.....60

Figure 3.11 Relationships between fluvial acoustic tomography (FAT) system and station 3 Acoustic Doppler Current Profiler (S3-ADCP): (a) and (c) eastward; (b) and (d) northward velocity components. Red, black, and grey dashed lines denote the fitting line, the 1:1 line, and the 20% relative error line, respectively. The skill score (SS), the root mean squares difference (RMSD), and the mean relative error (MRE) are provided in each panel.....61

Figure 3.12 Relationships between fluvial acoustic tomography (FAT) system and station 5 Acoustic Doppler Current Profiler (S5-ADCP): (a) and (c) eastward; (b) and (d) northward velocity components. Red, black, and grey dashed lines denote the fitting line, the 1:1 line, and the 20% relative error line, respectively. The skill score (SS), the root mean squares difference (RMSD), and the mean relative error (MRE) are provided in each panel.....62

Figure 3.13 Typical depth-averaged currents from fluvial acoustic tomography (FAT) system during the StreamPro Acoustic Doppler Current Profiler (ADCP) observation period. The black and red arrows represent the velocities acquired by FAT and StreamPro ADCP, respectively. Red solid lines connecting the acoustic stations represent the StreamPro ADCP observation routes. The tidal phase of each sub-figure is indicated by a black dot on the water level. The root mean squares difference (RMSD) of the eastward and northward velocity components are given in each panel.

64

Figure 3.14 Time plots of the inverted (black lines) and observed (red dots) range averaged currents calculated along each transmission line. The skill score (SS), root mean squares difference (RMSD), and mean relative error (MRE) are provided in each panel.....

65

Figure 3.15 Uncertainty maps of inverse solutions during spring tide corresponding to the current distributions of Figure 3.6. The values of the damping factor α and the spatially averaged uncertainty of each figure are provided in the upper left corners of the respective figures.....

66

Figure 3.16 (a) Discharge at Yaguchi gauging station (blue line) and tidal discharge in the Kyu Ota River (black line), which was calculated from the two crossing transmission lines S2–S4 and S3–S6. Red lines indicate low-pass filtered data of the tidal discharge (black line) with a cut-off period of 24.4 h; (b) tidal ranges at two water level gauging stations (Eba and Misasa); (c) relationship between the daily spatially averaged amplitude and phase of M_2 , and the daily tidal range; (d) relationship between the daily spatially averaged amplitude and phase of M_4 , and the daily tidal range; (e) relationship between the daily spatially averaged amplitude and phase of M_2 , and the daily tidal discharge; (f) relationship between the daily spatially averaged amplitude and phase of M_4 , and the daily tidal discharge; (g) relationship between the daily spatially averaged amplitude ratio of M_4/M_2 and the phase of $2M_2-M_4$, and the daily tidal range; and (h) relationship between the daily spatially averaged amplitude ratio of the M_4/M_2 and the phase of $2M_2-M_4$, and the daily tidal discharge.....

69

- Figure 4.1** Time plots of the range averaged salinity calculated for the selected three transmission lines during the observation period.....80
- Figure 4.2** Time plots of the temperature and salinity obtained from the four fix stations during the observation period.....81
- Figure 4.3** Temporal variations of the depth-averaged velocity and salinity distribution at a 1-hour interval during spring tide. The FAT stations are marked by black dots, and the actual acoustic transmission rays among the FAT stations are connected by the solid lines. The tidal phase of each sub-figure is signaled by a black dot on the water level at the lower right corner. 82
- Figure 4.4** Temporal variations of the depth-averaged velocity and salinity distribution at a 1-hour interval during neap tide. The FAT stations are marked by black dots, and the actual acoustic transmission rays among the FAT stations are connected by the solid lines. The tidal phase of each sub-figure is signaled by a black dot on the water level at the lower right corner. 83
- Figure 4.5** (a) salinity and (b) water level variations during the semi-diurnal tidal cycle; (c) the water level data monitored at the Misasa gauging station, and precipitation data were downloaded from the Japan Meteorological Agency; (d) spatially averaged tidal excursion of the flood and ebb tide during the observation period.....85
- Figure 4.6** Relationships of salinity between fluvial acoustic tomography (FAT) system and conductivity-temperature-depth (CTD)/conductivity-temperature (CT) sensors: (a) S1-ADCP, (b) S2, (c) S3-ADCP, and (d) S5-ADCP. The skill score (SS), the root mean squares difference (RMSD), and the mean relative error (MRE) are given at each panel. S1, S2, S3, S5 are station 1, 2, 3, and 5, respectively; ADCP - Acoustic Doppler Current Profiler. Comparisons of salinity obtained from inverse results and CT/CTD results.....86
- Figure 4.7** Time plots of the inverted (black lines) and observed (red dots)

range averaged sound speed calculated along each transmission line. The skill score (SS), root mean squares difference (RMSD), and mean relative error (MRE) are provided in each panel.....	87
Figure 4.8 Uncertainty maps of inverse solutions of sound speed during spring tide corresponding to the salinity distributions given in Figure 3.6. The values of the damping factor α and the spatially averaged uncertainty of each figure are provided in the upper left corners of the respective figures.....	88
Figure 4.9 Time plots of the inverted sound speed (black line) and the sound speed calculated by the CT sensor at S2 (blue line). The skill score (SS), root mean squares difference (RMSD), and mean relative error (MRE) are provided in each panel.....	89
Figure 4.10 (a) The distribution of advection of salinity and residual currents at the junction during spring tide; (b) The distribution of salinity and residual currents at the junction during neap tide.....	90
Figure 4.11 Temporal variations of the velocity profiles (positive indicates flood, upstream) at Station S3-ADCP during spring and neap tide.....	91
Figure 5.1 (a) Schematic map of the tidal junction, (b) sketch of the tidal discharge measurement, examples of the depth-averaged tidal currents along the selected transect (c) ebb tide and (d) flood tide.....	94
Figure 5.2 Time plots of the range averaged currents for Lines S2S3, S2S4 and S3S6; the green line represents the depth averaged currents obtained at S3-ADCP. (positive indicates seaward).....	95
Figure 5.3 Time plots of the sub area currents obtained from the inverse method; the green line represents the depth averaged currents obtained at S3-ADCP. (positive indicates seaward).....	96
Figure 5.4 Histogram of the flow direction calculated from (a) the range averaged velocity of S2S4 and S3S6; (b)-(l) the inverse velocity at each	

sub area.....97

Figure 5.5 Time plots of the tidal discharge obtained from three methods (a) one transmission line S2S3; (b) two crossing transmission lines S2S4 and S3S6; (c) summation of tidal discharge at each sub area. The green dots denote the tidal discharge obtained using StreamPro ADCP.....98

Figure 5.6 Comparisons between the tidal discharge measure by FAT and StreamPro ADCP.....98

List of Tables

Table 2.1 Harmonic analysis of water level.....27

Table 4.1 Comparison of the GPS-determined and corrected distances. The Salinity offset reference to the typical environment of $H = 3$ m, $T = 10$ °C, $S = 25$79

Abstract

Investigating the hydrodynamics of tide and river flow is important to provide the best management practices for delta channels and estuarine ecosystems and understand the alteration processes of morphodynamic environments in tidal rivers, as well. This dissertation investigated the spatiotemporal variations in sediment, tidal currents and salinity, aiming to provide a clear understanding of the hydrodynamics between river flow and tides in the Ota River network system. The findings can facilitate the management of small and shallow multi-channel estuarine systems. This work is divided into two main themes: (i) sediment dynamics at a tidal controlled channel, and (ii) flow and salinity patterns at the tidal junction.

The purpose of the first theme was to investigate the behavior of suspended particulate matter concentration (SPMC) variability toward different external forcings in the tide controlled Otagawa floodway. In this study, the relative contributions of external forcings to SPMC were quantified using singular spectrum analysis (SSA). The main environmental features affecting SPMC were identified as i) spring-neap tidal oscillation, ii) ebb/flood velocities, and iii) tidal straining. Large SPMC fluctuations occurred within strong mixing and were directly related to the sediment resuspension stirred up by spring-neap tidal cycles (73.6%–81.9% contributions on SPMC variations) and ebb/flood velocities (9.6%–19.5% contributions on SPMC variations). On the seasonal scale, the river discharge is a key variable that explains the downstream flushing and promoting the occurrence of a convergence zone at the floodway. At the upstream, the spring-neap tidal oscillation dominated the mobility of suspended particulate matter (SPM) under low river discharge. Two interesting findings were revealed in this study: (i) the SPMC and SPM-transport variation responses to tidal forcing (tidal asymmetry) were dominated and modified by river discharge and (ii) the effect of river discharge on the SPMC and SPM transport did not result in a uniform state along the floodway. It is believed that these findings provide further understanding of the dynamics of suspended sediments in shallow tidal systems.

The second part of this thesis highlighted the application the fluvial

acoustic tomography system (FATs) to shallow tidal junctions for studying the flow division and spatiotemporal difference of velocity and salinity are vital to understand the hydrodynamics in multi-channel networks. Therefore, in the second theme, this study aimed to observe continuous 2D current and salinity distributions at a shallow tidal junction using six FATs for ~34.4 days. The horizontal distribution and spatiotemporal variations in the currents and salinity were efficiently estimated by the inverse method. The reciprocating patterns of salinity during the spring tide at the junction well respond with the tide. Due to the density-driven current mechanism, the salinity pattern at the junction revealed that the maximum salinity during neap tide is higher than that during the spring tide. The asymmetry geometrical shape of the junctions modified the density current and salinity behaviors, the shallower side weakened the tide velocities, the wider side prompted more flow into the shallower side, and thereby increased the amount of salinity at the wider side (higher density). The tidal velocity amplitude and the outflow velocity associated the river discharge basically controlled the recovery of salinity at the junction.

For spring tides, high salinity occurred around high water, whereas salinity was negligible at low water. During flood tides, significant landward currents flowed with the maximum speed of ~0.4 m/s at the downstream of the junction near station S4, and significant seaward currents with the maximum speed of ~0.55 m/s occurred during ebb tides at the upstream of the junction near station S3. For neap tides, the salinity pattern began to develop landward from the low water and reached the maximum salinity around the high water; salinity at the ebb slack remained high. Inverted results of FATs indicated a counter-clockwise circulation at the center of the tomography area around the low water during neap tide; some of the currents continuously flowed landward at the downstream of the junction, whereas the western branch river (Tenma River) continuously flowed with seaward currents. The behaviors of the currents did not vary considerably over the neap tidal cycle. The freshwater discharge at the junction was ~29.2% of the tidal discharge during the observation period, induced a certain extent increment and decrement of ebb and flood velocities, respectively. Furthermore, tidal harmonic analyses of the reconstructed currents were performed to clarify the interactions between river flow and tides at the tidal junction. The results reflected the increased

tidal wave deformation that occurred with the gradually increasing tidal range and demonstrated the role of the limited river flow on the tidal asymmetry at this tidal junction. These studies advance the understanding of river flow and tidal dynamics in shallow tidal junction systems.

Chapter 1: Introduction

1.1 Study overview

Multi-channel delta systems, such as the Rhine-Meuse delta [1], the Mississippi River delta [2], the Mekong delta [3], the Yangtze delta [4]–[6], the Pearl River delta [7], [8] and the Ota River delta [9]–[12], usually feature typical characteristics, where the separate channels are interrelated via the network system, leading to both longitudinal and transverse variations of water current circulation caused by the interactions between river flow and tide [8].

The estuary is, therefore, a unique environment that is mainly influenced by tidal movements and river discharge. Tides propagating in an estuary are generally a mixture of progressive waves and standing waves. River flow also influences tide during the tide propagating process. Tides carry salinity and sediment in and out of the estuary as well as mix them over the entire estuary. River flows limit the saltwater intrusion and carry land sediment out of the estuary. Capturing the nonstationary features of river flow-tide interactions and incorporating them into an analytical/numerical model to distinguish tidal from nontidal variations is difficult [13]. Thus, it remains a challenge to examine nonstationary interactions between river flow and tide.

Understanding the dynamics of river-tide interactions has important implications for managing estuarine systems. The nonstationary interactions between river flow and tide exhibit complex behavior over time and space, for instance, how does the tidal motion acts to reduce the asymmetric division of flow or sediment over the small multi-channels and how does the planform remain stability with the interactions between river flow and tide in small multi-channel systems? Thus, in this study, we investigate and explore the hydrodynamics of interactions between river flow and tide in the small multi-channel estuary with the Ota River network as a case-specific example.

1.2 Literature Reviews

Large multi-channel systems, such as the Yangtze River estuary [5], were often studied noticed because of their high discharge and sediment transport rates. In large multi-channel systems, river discharge usually are strongly and significantly alters the process of tidal propagation by reducing tidal amplitude, delaying wave propagation, and altering energy distribution between tidal frequencies [13]. River flow constrains landward saltwater intrusion by enlarging ebb currents. River discharge is also the dominant mechanisms in exporting river-supplied sediment seaward [5]. Interactions between river flow and tide in these large multi-channel networks could lead to significant water stratification, water circulation and high-turbidity areas in the estuary areas. Hydrodynamic environment in the small multi-channel systems show some differences with that in large multi-channel systems, due to the limited river flow and mesotidal characteristics [14], [15]. The most section of small multi-channel systems was affected by tides, which know as a tidal river, a realm that can extend inland tens/hundreds of kilometers [16]. Tidal rivers are a vital and nexus between physical oceanography and hydrology, received little studies [16]. Only in the last few decades that substantial research works have partially studied to investigate the interactions between river flow and tide [16].

1.2.1 Interactions between river flow and tide on suspended particulate matter (SPM) dynamics

In general, , SPM undergo various processes of resuspension, settling and advection in the estuaries [17]. SPM dynamics are mostly controlled by several forcings, such as tides, wind, sources of sediment, thermohaline fields, river flow flux [18]–[20]; as well as by biological processes [21] and human effect [22] (dredging-disposal cycles), typically for the small estuaries. In the estuaries, the most significant timescale for SPM dynamics are the tides; the alteration of high current velocities and slack water inducing a continuous change in resuspension, mixing, settling and deposition. Recently, Geleynse et al. (2011) assessed the influence of tides on river delta formation. They found that tide-influenced river deltas prograde mainly via lengthening of initially formed, relatively stable distributaries characterized by cyclicity in deposits, representing tidal

rhythmites. Hence, quantifying the contributions of different factors to SPM variability is a difficult task that has barely been studied.

Tidal hydrodynamics determine basically sediment transport in the estuaries [24]. Both estuarine gravitational circulation and tidal asymmetry are also of great importance. These complex flow patterns are largely determined by the interaction of the river flow and tidal currents. Tide-induced bottom stresses, as well as stratification, act as the main factors to control sediment resuspension, river flow constrains landward sediment transport by enlarging ebb currents. Nevertheless, river flow is unsteady and vary rapidly in the small multi-channel estuaries.

Modeling of sediment transport patterns depends heavily on some critical parameters that describe sediment resuspension and settling processes, such as critical bottom stress and settling velocity [25]. The complex and highly variable estuary environment make quantifying these parameters a formidable problem. Besides, the processes related to tidal dynamics, varied river flow and interactions between them are difficult to be simulated by numerical models. Hence, seeking effective methods to quantify the SPM variability related to environmental forcings is an imperative task that need to be studied, and additional comprehensive investigations and analyses of these factors and their interactions during different specific time scales are important for understanding the SPM mechanisms.

1.2.2 Interactions between river flow and tide on hydrodynamics

River flow influences tide by dissipating tidal energy, damping tidal amplitude, and altering tidal phases. Theoretical analysis suggests that the amplitude of an incident wave from the ocean could vary with the square root of river flow in the landward direction in a channel of constant width and depth [26], one study in the Columbia River estuary found that there exist a quasi linear relationship between tidal damping modulus and river flow [27]. Furthermore, River flow also modulates tidal interactions and the resultant generation of over-tides and compound tides. River flow attenuates tidal energy upriver while stimulating energy transfer from the principal tides to over-tides downriver. Recent research has focused on the role of tides in the division of flow over the distributaries, for example [28]–[30]. Buschman et al. (2010) and Sassi et al. (2011) used a numerical

model to study the interactions between river flow and tide in small multi-channel networks, their model results showed that the tide can have a significant influence on river discharge division over delta distributaries, and the interactions between river flow and tide can create differential water level setup in neighboring channels. This would favor the allocation of river discharge to smaller channels that would receive a comparatively small portion of the river discharge in absence of the tide. Leonardi et al. (2015) suggested that even very small tides can strongly impact the velocity field at distributary mouths, irrespective of the river discharge regime. Their studies showed that the tide have a significant influence on river discharge division and flow patterns over delta distributaries.

Most of research reviewed in above were relied on the numerical models and capture only part of the dynamic in the multi-channel estuaries. Numerical models are an alternative method of analysis, offering insight in the physical mechanisms underlying the interaction between river flow and the tide from the governing shallow water equations with a lot of assumed conditions. However, in small multi-channel estuaries, at each specific channel, numerical models could not effectively reproduce the hydrodynamics of river flow and tide. Tidal processes generally are complex and highly dynamic due to the effect of extreme shallow water depths in the tidal flats and tidal channels. Complexities can also arise because during low water levels, some of the channels may be blocked, resulting in ponding of water, occurrence of transient shallow wave induced currents [31]. Besides, river flow was unsteady and vary rapidly in the small multi-channel estuaries. These processes are difficult to be simulated by numerical models, therefore, deeper and comprehensive understanding of the interactions in small multi-channel systems by field observations are need.

Hence, enhancing our insight of the interaction between river flow and tide in small multi-channel networks has vital importance for the protection and management of estuarine environment since the interplay is closely related to sediment transport, flow patterns and divisions, and water utilization [32]. Advanced methods of analysis and observations are also required so that we can widely and deeply understand the interactions between river flow and tide.

1.2.2 Interactions between river flow and tide on salinity dynamics

Savenije (2005) presented a comprehensive theory for the modelling of steady state and unsteady state salinity patterns in estuaries. It is based on the analysis of 17 estuaries world-wide, although it seems that it can be applied to predict the salinity distribution in many estuaries, when the basic information on topography, tide and river discharge is known. But this theory was derived for single channel estuaries and for estuaries where the tide experiences only modest damping or amplification, it cannot be well applied in small multi-channel estuaries. For a multi-channel estuary, the tide processes exhibit different characteristics in each channel, the river flow also flows asymmetry in each channel.

Geyer and MacCready (2014) reported that the salinity of the estuary and the associated salinity gradient varies owing to the variations in the river flow, the exchange flow, and tidally induced processes. The river flow has a simple impact on the salinity patterns, the increased river flow pushes the salt intrusion seaward and increases salinity gradient. However, the increases salinity gradient is complicated by the response of the exchange flow between river flow and tide, tidal induced transport process.

The application of advanced measurements (e.g., FATs) would benefit the future salinity research. Investigations of the salinity field structure would benefit the understanding of the lateral structure processes. A more accurate map of salinity parameter space would promote the development of prediction models.

1.3 Research Motivations and objectives

Mixing owing to gravitational circulation can play a dominant role in a single-branch and stratified estuary, but in a single-branch and well-mixed estuary, tidal pumping can be the most important mixing mechanism [32]. In multi-channel estuaries, the similar phenomenon happens, however, in a more complex way due to the complicated topography and bifurcations [32]. Tides propagating in the multi-channel estuaries are usually a mixture of progressive waves and standing waves [35]. The river discharge acts to redistribute and dissipate tidal energy. Tides carry salinity and sediment import and output of the tidal channels with the effect of river discharge as well as mix them over the entire estuary. Therefore, the effects of the

interaction between river flow and tide on flow patterns, salinity and sediment movement need to be clarified in multi-channel systems.

Firstly, sediment concentration in multi-channel estuary fluctuates spatially and temporally. The transport and trapping of sediments in estuaries is controlled by various factors, e.g., river flow, tidal dynamics, flow patterns, salinity stratification [36]. In mesotidal estuaries, sediment trapping and convergence are mostly formed at the landward limit of the saltwater wedge, which develops when river flow and landward saline water meet [34]. The sediment transport is strongly affected by i) the estuarine circulation due to the movement of salt fronts and ii) turbulent mixing due to the variations in intertidal stratification. To systematically analyze the interactions between river flow and tide in multi-channel estuary, prior information about the spatiotemporal variability of the suspended sediment responding to the interactions is essential [12]. Tidal currents and tidal asymmetry play important roles in sediment mobility; however, sediment mobility is directly related to river discharge. Nevertheless, in the Otagawa floodway (tidal control), how the river flow-tide interactions determine the fate of suspended sediment with the controlled river flow is a remaining issue that need to be studied.

Secondly, examining the structures of tidal currents in tidal rivers is of great importance as tidal rivers are extensive in length and area. The stage-discharge relationships in small tidal rivers are not reliable as they are subject to unsteady flow conditions, the velocity distributions in the cross-section are complex and unsteady due to the combination of the river flow and the saltwater intrusion. Studies relying on 2D data with a visual means of determining the spatiotemporal difference of velocity are helpful to better understand the process of tidal currents. Traditional observation methods comprising fixed or moving-boat ADCPs are only capable of acquiring velocity behaviors at one/several sites or sections, thus it is difficult to detect the rapid processes of tidal current patterns by using them. However, the horizontal distribution and spatiotemporal variation of velocities can be efficiently reconstructed by the inverse method using the fluvial acoustic tomography system (FATs). Hence, continuous and long-term monitoring of 2D tidal current patterns at a shallow tidal junction with FATs are helpful to better study the interactions between river flow and tide on flow patterns, while also providing a visual means of determining flow

division and spatiotemporal differences of velocity.

Thirdly, saltwater can intrude upstream due to the difference in density between the freshwater and the seawater, and due to the tidal movement [36]. The salinity intrusion itself can reach a great distance from the river mouth, especially when the river flow is small. The Ota River network is an ideal research area with mesotidal characteristic and limited river discharge. The spatial and temporal distribution of salinity can significantly affect residual currents through the gravitational and tidal straining circulation. An enhanced understanding of saltwater dynamics under the interactions in multi-channel estuaries is essential.

Hence, tracing these variations temporally and geographically is important to achieve a clear understanding of the dynamics between river flow and tide, and the knowledge can facilitate the management of estuarine systems.

In view of these, the objectives of this thesis are:

- To reveal the sediment dynamics in response to the interactions between river flow and tide and track the convergence zone between river flow and tide in a tide-controlled channel based on investigating the spatiotemporal variations of suspended sediment.
- To demonstrate the flow patterns under the response process of the interactions between river flow and tide at the tidal junction based on investigating the spatiotemporal variations of currents at the tidal junction using six Fluvial Acoustic Tomography Systems.
- To understand the tide-induced variability in the density field at the tidal junction based on investigating the spatiotemporal variations of salinity at the tidal junction using six Fluvial Acoustic Tomography Systems.

1.4 Research methods

1.4.1 Instruments and methods

Aquadopp Profiler

The Aquadopp Profiler is an acoustic tool with a wide range of applications, including ocean, estuary, or river. The instrument is usually used in real-time applications but also includes all parts required for self-contained deployment with data stored to an internal data logger. In chapter

2, three 2 MHz ADCPs (Aquadopp Profiler, Nortek) were installed to measure the 3D velocities and backscatter intensity in the water column. The backscatter intensity of ADCP have been used to estimate the SPMC by using the basic SPM modeling equations. SSA (Singular Spectrum Analysis) is similar to principal component analysis [37] and applied to the SPMC series data in chapter 2. This method can extract the necessary information related to environmental parameters from short/long time series data without previous knowledge of the nonlinear hydrodynamics. During the field observations, the conductivity-temperature-depth sensor (Compact-CTD, JFE Advantech) was set around 0.4 m above the riverbed to collect depth, salinity, temperature data. The details of these are shown in Chapter 2.

Fluvial Acoustic Tomography system (FATs)

Ocean acoustic tomography (OAT) has been suggested as a potential oceanographic technique to investigate mesoscale oceanic phenomena [38]. Since after, the Coastal acoustic tomography (CAT) was designed to extend the applications of OAT in coastal areas for continuous monitoring of tidal currents [39]. However, CAT uses high-power signals with frequencies < 10 kHz to measure the sound travel time (in the order of kilometers) between two stations in coastal waters. The fluvial acoustic tomography (FAT) system is a promoted application that can be utilized in reasonably shallow waters to investigate shallow currents in riverine and tidal environments [9], [40]. In chapter 3 and 4, six FATs with a 30-kHz central frequency were deployed at the tidal junction. The 2D currents and salinity were acquired by inverse method, as we described detailly in Chapter 3 and 4. During the observation period, three ADCPs were installed to observe the velocities and validate the inverted 2D velocities; two CT sensors and two compact-CTD were also deployed to measure the salinity and temperature near the bottom. The details of these are shown in Chapter 3 and 4.

StreamPro ADCP

StreamPro ADCP offers a preferred solution for making discharge measurements in small and medium streams. The StreamPro ADCP is an accurate, rapid-sampling current profiling system designed to operate from a moving boat. It was used in Chapter 3 and 5, to measure flow velocity and tidal discharge at the junction, and to validate the inverted 2D

velocities and the tidal discharge results.

1.5 Research outline of the thesis

This thesis is largely based on several field measurements were performed at the Ota River network. These measurements are presented in the following chapters and included detailed time series of suspended sediment concentrations, tidal currents, salinity, and tidal discharge.

In Chapter 2, we used field measurements to evaluate the impacts of river flow-tide interactions on the longitudinal variations and transport of suspended sediments in a long mesotidal floodway (Otagawa floodway), the westernmost branch of the Ota River network. The main purpose of this chapter was to quantify the effects of tidal forcings on the Suspended particulate matter concentration (SPMC) variability in a tide-controlled channel, in order to shed light on SPMC dynamics in response to tidal hydrodynamics. This chapter has been reproduced with minor change from, *Xiao, C., Kawanisi, K., & Al Sawaf, M. B. (2020). Suspended particulate matter concentration in response to tidal hydrodynamics in a long mesotidal floodway. Estuarine, Coastal and Shelf Science, 233, 106525.*

In Chapter 3, six Fluvial Acoustic Tomography systems (FATs) were applied to investigate the tidal currents at a tidal junction, in the middle section of the Ota River network. This chapter aims to characterize the tidal regime in terms of a continuous 2D tidal current field, tidal asymmetry, tidal dampening, the evolution of tidal constituents, and the propagation of tides at the shallow tidal junction by using the inverse currents. We intend to collect several pieces of evidence to demonstrate the response process of the interactions between river flow and tide at the tidal junction.

In Chapter 4, six Fluvial Acoustic Tomography systems (FATs) were applied to investigate the salinity distributions at a tidal junction, in the middle section of the Ota River network. The spatial and temporal distribution of salinity can significantly affect residual water currents through the gravitational and tidal straining circulation. This chapter aims to characterize the tidal regime in terms of a continuous 2D salinity field and aims to further understand the tide-induced variability in the density field and turbulent mixing characteristics at the tidal junction.

The chapters 3 and 4 have been reproduced with some change from, *Xiao, C., Kawanisi, K., Torigoe, R., Al Sawaf, M.B., Mapping tidal current*

and salinity at a shallow tidal channel junction using the fluvial acoustic tomography system, Estuarine, Coastal and Shelf Science (2021), doi: <https://doi.org/10.1016/j.ecss.2021.107440>.

In chapter 5, the inverse velocities were employed to estimate the tidal discharge at the tidal junction. The stage-discharge relationships in small tidal rivers are not reliable as they are subject to unsteady flow conditions, moreover, the velocity distribution in the cross-section is complex and unsteady due to the combination of the runoff and the saltwater intrusion. Hence, continuous high-quality measurement of tidal discharge in tidal estuaries is need and scientific.

Lastly, chapter 6 provides a summary and a discussion of future directions on these topics.

Chapter 2: Suspended particulate matter concentration in response to tidal hydrodynamics in the Otagawa floodway

2.1. Introduction

The dynamics of suspended particulate matter (SPM) are intricate in estuarine systems and significantly vary with time and spatial scale. The distribution of SPM in a water column results from the combined processes of erosion, deposition, and transport. Moreover, the suspended particulate matter concentration (SPMC) is modified by the overall variations of multiple controlling factors [17]. Hence, additional comprehensive investigations and analyses of these factors and their interactions during different specific time scales are vital for understanding the transport mechanisms of SPM.

Environmental forcings related to SPMC in estuarine environments have been well investigated [18], [41]–[43]. Forcings can be divided into two main categories: (1) deterministic (tidal cycle, tidal range) [44] and (2) stochastic (runoff, wind) constituents [18]. These categories are characterized by multiscale, unstable, and nonlinear dynamic processes. Hence, quantifying the contributions of different driving factors to SPMC variability is a difficult task that has barely been studied. Schoellhamer (2002) and French et al. (2008) applied the singular spectrum analysis (SSA) method to quantify the suspended sediment concentration variability related to environmental forcings in San Francisco Bay and Blyth Estuary, respectively. The SSA method was applied to high-frequency time-series data, however, these studies were restricted to single cross-sections of the systems and lacked a detailed analysis of seasonal differences of controlled forcings.

To analyze sediment transport dynamics and the spatiotemporal variability of the responses of suspended particles to tidal hydrodynamics thoroughly, prior information about the SPMC is essential. However, it is difficult to measure these rapid fluctuating characteristics in riverine environments. Traditional techniques for laboratory analysis of SPMC

often rely on periodic in-situ water sampling [17]. Expectedly, these approaches may be satisfactory for many applications but still have limitations, especially in estuaries, owing to uncertain characteristics of suspended particles. However, gathering water samples may be not sufficient to characterize the behavior of suspended particles over a long time, due to the variations in the transport of suspended materials brought by changes in tidal velocity, tidal range, and wind effects.

In large-scale studies, acoustic Doppler current profilers (ADCPs) have been used for decades to measure currents. In recent years, the amplitudes of back-scattered signals have been used to detect the SPMC [46], [47]. Furthermore, there have been recent studies on measuring suspended sediments by using swath bathymetry systems [48]. In smaller-scale studies, noteworthy, advanced efforts have been made through the use of sound backscatter to study near-bed sediment transport processes [49]. Acoustic profilers are being developed for near-bed studies and can estimate both suspended sediment concentrations and current profiles with high spatial–temporal resolutions and provide necessary information about bedform variations.

Estuarine systems have several problems associated with maintenance with respect to factors such as dredging, port development, and regulation of incoming river flow. For example, in the case of the Yangtze river, the annual mean discharge is $2.93 \times 10^4 \text{ m}^3/\text{s}$, and the annual mean suspended sediment load is 4.9×10^8 tons [24]. Tidal currents and tidal asymmetry play important roles in sediment mobility, however, sediment mobility is directly related to water discharge. In the case of Otagawa estuary, Hiroshima, Japan, tidal hydrodynamics primarily determine the fate of suspended sediment in the case of limited runoff [50], [51]. As an example, in the Rotterdam Waterway estuary, nearly 75% of the fine sediment is imported from the sea by tides [52].

In this study, we aimed to reveal sediment dynamics under tidal hydrodynamics with low river discharge. Several fundamental issues related to tidal hydrodynamics remain unanswered, such as the main factors that contribute to sediment exchange processes between the bed and overlying water. Therefore, tracing these variations temporally and geographically is important to achieve a clear understanding of sediment dynamics, and knowledge of sediment dynamics can facilitate the

management of estuarine systems. The main purpose of this study was to quantify the effects of tidal forcings on the SPMC variability in a tide-controlled channel, in order to shed light on SPMC dynamics in response to tidal hydrodynamics. The remainder of this paper is structured as follows. The descriptions of the study area and methods for data processing are given in Section 2.2. The results and discussion are provided in Sections 2.3 and 2.4, respectively. Finally, the conclusions are presented in Section 2.5.

2.2. Materials and methods

2.2.1 Study area

The Otagawa estuary is composed of a shallow and tide-controlled delta with several channels. The maximal tidal compartment range reaches up to around 13 km from the river mouth [53]. The Ota River divides into two main branches nearly 9 km upstream from the river mouth. Rows of Gion sluice gates control the volume of the runoff. In the case of normal operation, two gates are closed and only one gate is slightly opened to release water with a controlled cross-section of 32 m×0.3 m. During flood events (when the discharge at Yaguchi station is greater than 400 m³/s), all of the sluice gates are completely opened and the freshwater runoff from the Gion sluice gates is designed to be about half of the total river discharge. The geometry of the sluice gates and the accumulated sediment around the gates along with asymmetric tidal currents produce an unstable and complicated flow system. The flow pattern varies considerably with both the tidal phase and the amount of runoff flowing through the gates.

Razaz et al. (2015) pointed out that tidal straining and bathymetry are the main sources of flocculation in the Otagawa floodway. Kawanisi et al. (2008) discussed the effects of river discharge, tidal range, and wind on the transport of sediment. They revealed that there was suspended sediment transport upstream within the spring tide. The upstream transport increased with increasing tidal range and decreased with increasing distance from the mouth. At the flood events, the suspended sediment was transported downstream. A long-term discharge monitoring campaign was conducted using the fluvial acoustic tomography (FAT) system, showing that around 20% of the total Ota River discharge flowed into the floodway on normal

days and that it received up to 50% of the total runoff during flood events [9]. Furthermore, it was reported that the maximum tidal current velocities during flood and ebb were around 0.65 m/s and 0.5 m/s, respectively, and during the spring tide the peak tidal range reached 4 m at the river mouth [53]. In general, due to the limited runoff under normal conditions and mesotidal inflow from Hiroshima Bay, the estuarine circulation in the Otagawa floodway is moderate.

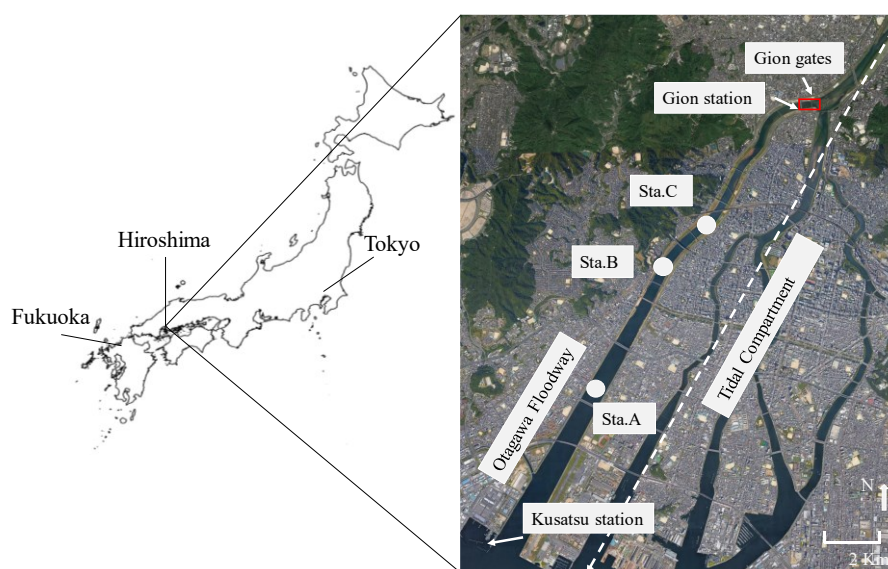


Figure 2.1 Research area and observation sites along the Otagawa floodway, Hiroshima City, Japan.

2.2.2 Instruments and methods

Three locations along the floodway in the Ota estuary were selected as observation sites. Stations A, B, and C were located 2.8 km, 4.8 km, and 6.0 km upstream from the river mouth, respectively, as illustrated in Figure 2.1. Several field observations were performed on the Otagawa floodway at different periods. At station A, measurements of hydrodynamics and sediment variables were performed during two periods: from July 29 to August 16, 2007 and from January 6 to 27, 2008. During the observation periods, a 2 MHz ADCP (Aquadopp Profiler, Nortek) was installed to measure the 3D velocities and backscatter intensity in the water column, with a 20 min sampling interval and average interval of 180 s. The bin size was set as 0.1 m, the bin number was 55, and the blank distance was 0.05 m. During summer, the ADCP was installed about 30 m away from the

right bank (simply expressed as Sta. A_R) and it was set upward in the water column. During winter, the ADCP was installed at the center of the channel (simply expressed as Sta. A_C) and it was set downward from the water surface. During both field observations, a conductivity–temperature–depth sensor (Compact-CTD, JFE Advantech) was set around 0.4 m above the riverbed to collect depth, salinity, temperature, turbidity, and chlorophyll-a data every 20 min during each observation period to identify the basic features of the estuary. At stations B and C, the ADCP sampling strategies were the same as those at station A. The observations at stations B and C were performed from December 22, 2007 to January 16, 2008 and from December 27, 2007 to January 10, 2008, respectively. In-situ water samples were suctioned during the observation period for ADCP backscatter calibration. Eight samples for particle size analysis were also collected, on December 12, 2007. The sample sites were located 0.5, 1.5, 2.5, 2.8, 3.5, 4.9, 7.0, and 8.0 km upstream from the mouth.

The SPM acoustic model of scattering has been employed by different researchers [55]. In this work, the basic SPM modeling equations were used to calculate the concentration. For further details on this SPM acoustic model, readers can refer to Kawanisi et al. (2008), Latosinski et al. (2014), etc. The relationship between the acoustical backscatter intensity of ADCP and the water sample concentration was established, and the obtained coefficients of regression R^2 were 0.70, 0.69, and 0.65 at Stations A, B and C, respectively. Moura et al. (2011) discussed the observation of SPM using different acoustic instruments in a shallow estuarine system with a low SPMC, reporting that the coefficients varied from 0.6 to 0.9. In this study, the validation results are appropriate for use in SPMC variation analysis.

SSA is similar to principal component analysis [37]. This method is capable of extracting the necessary information related to environmental parameters from short/long time series data without previous knowledge of the nonlinear hydrodynamics [56]. The SSA method is based on the concept of sliding a window of width M down a time series to obtain an autocorrelation matrix [57]. Then, eigenvectors (empirical orthogonal functions) and eigenvalues (k) of the lagged autocorrelation matrix are calculated. Afterwards, the random raw series data can be decomposed into several simpler periodic time series spectra, i.e., the so-called reconstructed

components (RCs). The RCs are calculated by multiplying eigenvectors times their corresponding principal components. Each contribution per variance is presented in terms of its eigenvalues k . Most of the variability is contained in the first RCs, and the remaining RCs consist of noise signals. For further details, readers can refer to Jalón-Rojas et al. (2016).

2.3. Results

2.3.1 Hydrodynamic characteristics in the Otagawa floodway

The seasonal differences in river discharge, water depth, salinity, water temperature, and current velocity profiles during summer from July 29 to August 16 (Sta. A_R) and during winter from January 6 to 26 (Sta. A_C) are shown in Figures 2.2 and 2.3, respectively. In summer, the compact-CTD was deployed two times, firstly from July 29 to August 2 and then from August 10 to 16. In this work, we did not compare the variations between two different water discharge measurement methods (FATS and the Rating Curves method). In fact, there exist some differences between the two discharge methods (i.e., FATS and Rating Curves) in the short term (a few hours). Nonetheless, it was demonstrated that the low-frequency variations of water discharge were similar [59], [60]. In this study, the discharge from Gion gates was not available. Razaz (2010) showed the relationship between the discharge from Gion gates (Q_{Gion}) and Yaguchi (Q_{Yaguchi}) station, and in this research, we referred to this relationship to convert Q_{Yaguchi} into Q_{Gion} for further assessment. Hence, in the related figures, the main labels are shown and marked according to the discharge values recorded at Yaguchi station. In summer, the water discharge (Q_{Yaguchi}) was higher, with maximum values up to 400 m³/s ($Q_{\text{Gion}} = 242$ m³/s) (Figure 2.2a). In contrast, during winter, the maximum discharge (Q_{Yaguchi}) was around 130 m³/s ($Q_{\text{Gion}} = 27$ m³/s) (Figure 2.3a). Moreover, a clear sign of tidal excursion is visible in the water depth time series across the surveyed periods. Owing to the saltwater intrusion from Hiroshima Bay, the water has higher salinity at deeper levels. The water is warmer at deeper levels during winter, while during summer, the lower water is colder than the upper water. During low water depth, intermittent variations of salinity and temperature were occurred as a result of tidal straining, as revealed in Figures 2.2c, 2.2d, 2.3c, and 2.3d. Field data from

summer and winter revealed the reciprocating tidal current in the floodway and indicated a strong flood-ebb tidal cycle (Figures 2.2e and 2.3e). Apparently, the ebb current was greater than the flood velocity during neap tide, whereas the vertical velocity gradients during spring tide were minimal. In general, the hydrodynamics of the Otagawa floodway are dominated by spring-neap and flood-ebb tidal cycles. Moreover, the hydrodynamics are modified by the river flow.

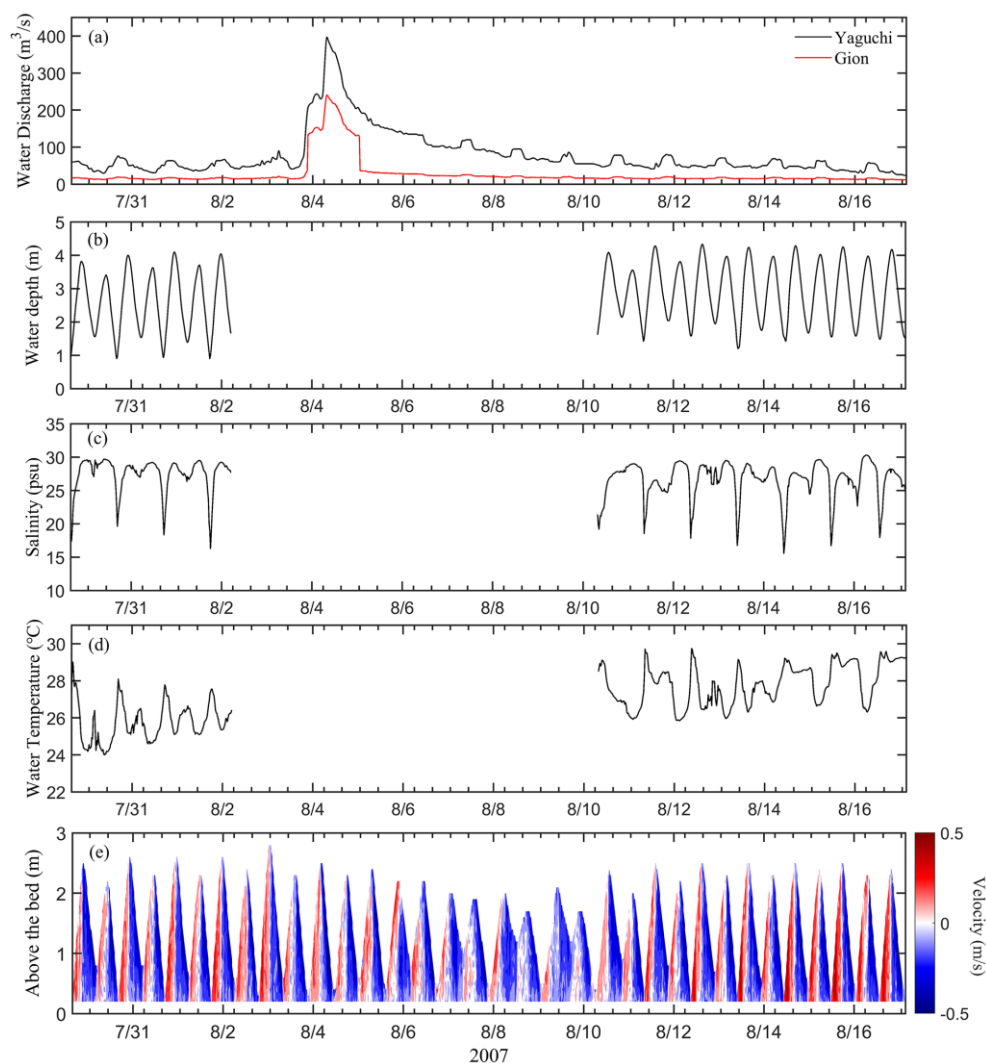


Figure 2.2 Hydrodynamic data during summer at Sta. A_R from July 29 to August 16, 2007. Temporal variations in (a) river discharge at Yaguchi gauging station, (b) water depth, (c) salinity, (d) water temperature, and (e) velocity. The red and blue values indicate the flood and ebb velocities, respectively. The compact-CTD was deployed two times, firstly from July 29 to August 2 and then from August 10 to 16. The Yaguchi gauging station is located around 14.6 km from the river mouth (not shown in Figure 2.1).

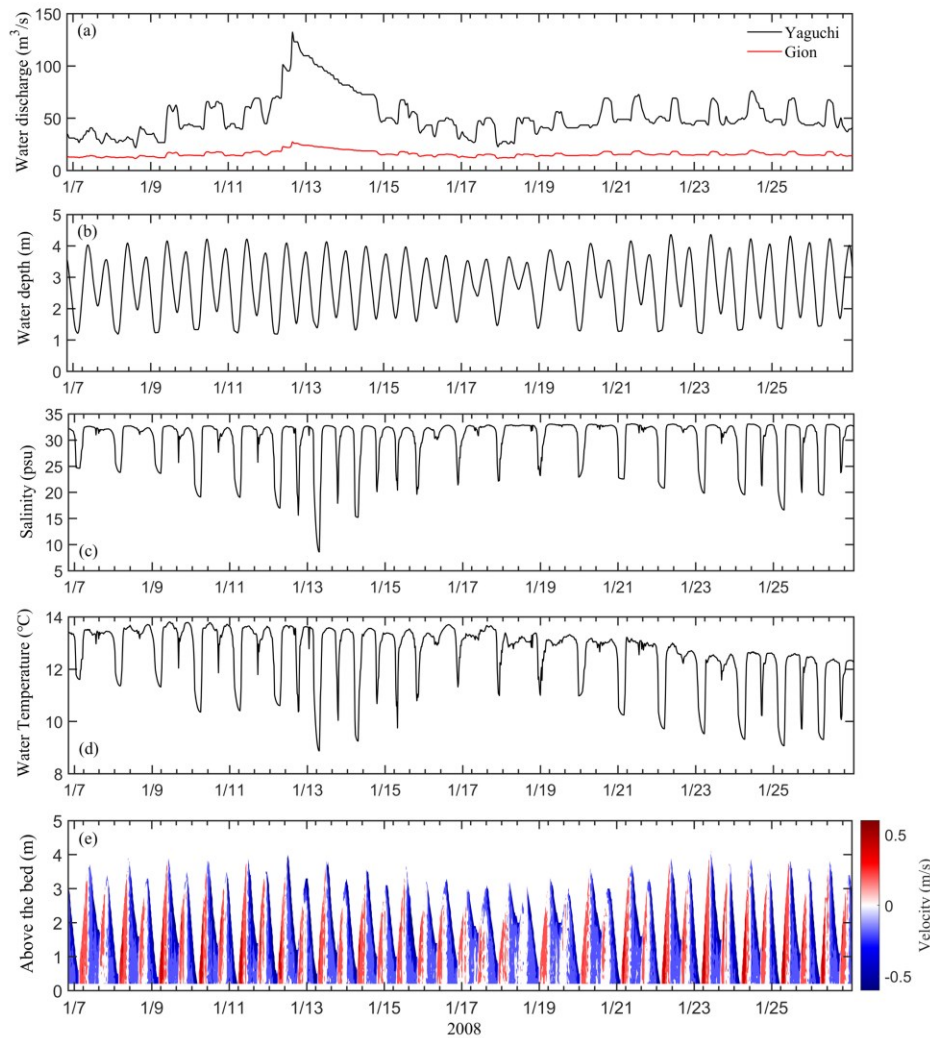


Figure 2.3 Hydrodynamic data during winter at Sta. A_C from January 6 to 26, 2008. Temporal variations in (a) river discharge at Yaguchi gauging station, (b) water depth, (c) salinity, (d) water temperature, and (e) velocity. The red and blue values indicate the flood and ebb velocities, respectively. The Yaguchi gauging station is located around 14.6 km from the river mouth (not shown in Figure 2.1).

2.3.2 In-situ suspended particulate matter concentration variations and sediment size distributions

During the observation periods, the SPMC time series were estimated from the ADCP backscatter. Hydrodynamic parameters that provide information about the variations of particles enable us to understand the mechanisms that may control the changes in SPMC during summer and winter and at different locations (spatiotemporal variations). The temporal

variations in the depth averaged SPMC are shown in Figure 2.4. During summer, the SPMC at Sta. A_R ranges from 0.5 to 100 mg/L and responds significantly to spring-neap tidal fluctuations (Figure 2.4a). In winter, the SPMC variability at Stations B and C is characterized by a local maximum and a minimum, ranging from 0.01 to 50 mg/L and corresponding to the spring and neap tides (Figures 2.4c and 2.4d). Meanwhile, the intermediate SPMC at Sta. A_C (Figure 2.4b) is about one order of magnitude larger than those at Stations B and C, with the maximum values up to 90 mg/L during the spring tide. Higher SPMC values are observable at Sta. A_C, relatively lower SPMCs appear at Sta. B, and the SPMC at Sta. C is the lowest. Generally, the qualitative variation in the SPMC is very similar to the tidal cycle pattern, which indicates the influence of tidal flow. As shown in Figures 2.2a and 2.3a, significant increases in river discharge can be observed around August 4 and January 12. Meanwhile, a higher SPMC can be captured, although not during the spring tide periods. The higher SPMC can be attributed to the influence of river runoff. Usually, SPMC fluctuations are well related to the spring-neap tidal cycle, i.e., to the higher tidal range that occurs during the spring tide. Although the spring tide is based on the lunar age, it does not entirely match the maximum tidal range. The SPMC is greater when the tidal range is maximal.

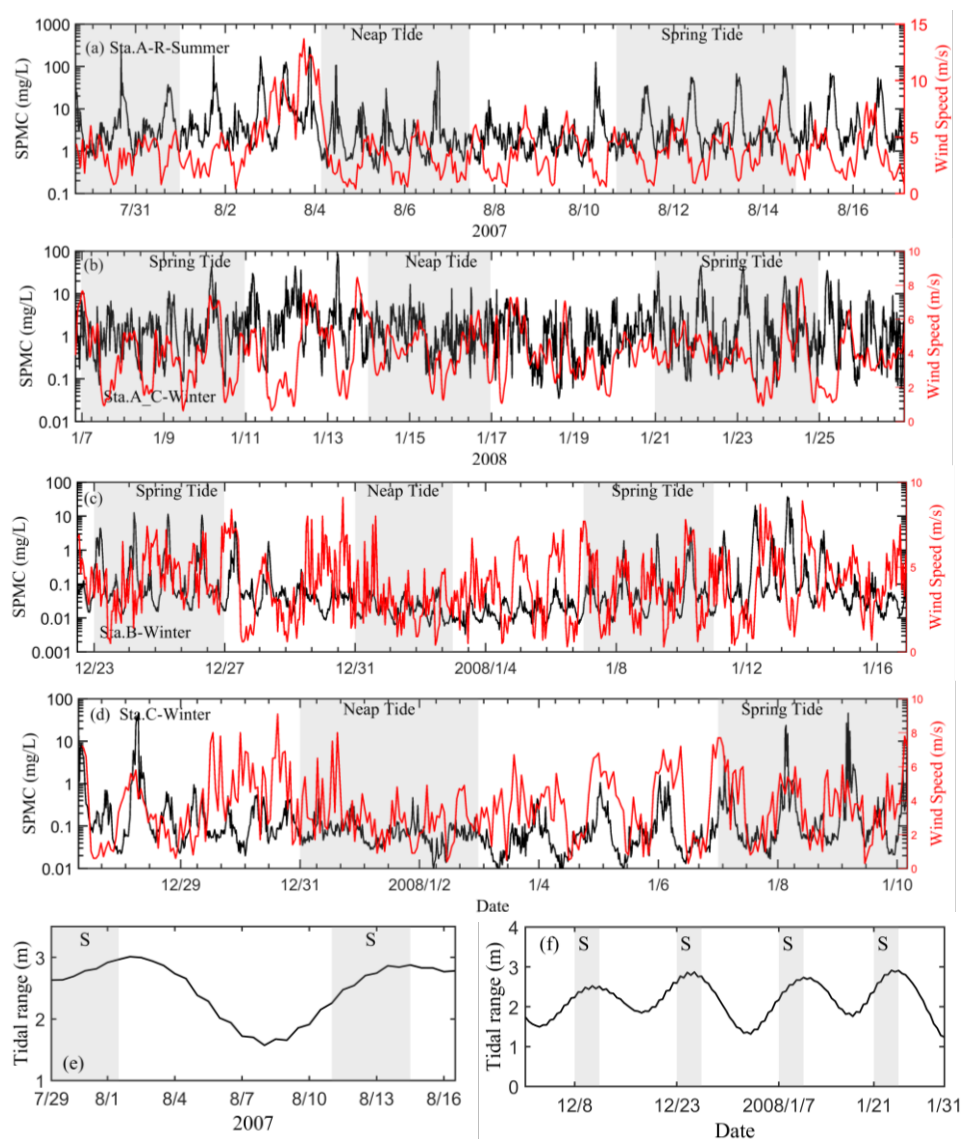


Figure 2.4 Depth-averaged SPMC time series and wind along the Otagawa floodway: (a) during summer at Sta. A_R from July 29 to August 16, 2007, (b) during winter at Sta. A_C from January 6 to 26, 2008, (c) during winter at Sta. B from December 22, 2007 to January 16, 2008, and (d) during winter at Sta. C from December 27, 2007 to January 10, 2008. Tidal range from Kusatsu gauging station during (e) summer and (f) winter. The shaded regions represent the spring/neap periods.

For further clarification, the grain size distributions in the study area were examined from eight sites selected along the floodway from the river mouth to near the Gion sluice gates, as presented in Figure 2.5. The bed materials in the Otagawa floodway, where the bed slope is about 1/3300, mainly consist of sand containing a little silt and clay. The grain size

distribution varies from upstream to the river mouth. The proportion of small particles increases closer to the river mouth. The particle size distributions can be divided into two types: (1) Type I, where the distance from the mouth is less than 3.5 km and the slope of the curve is the steepest when the volume percentage is less than 80%, which means that there are more fine particles; and (2) Type II, where the distance is greater than 3.5 km and the curve has a flatter slope when the volume percentage is less than 20%, which means that there are coarser particles; It are more difficult for the sediment to be resuspended in the water column.

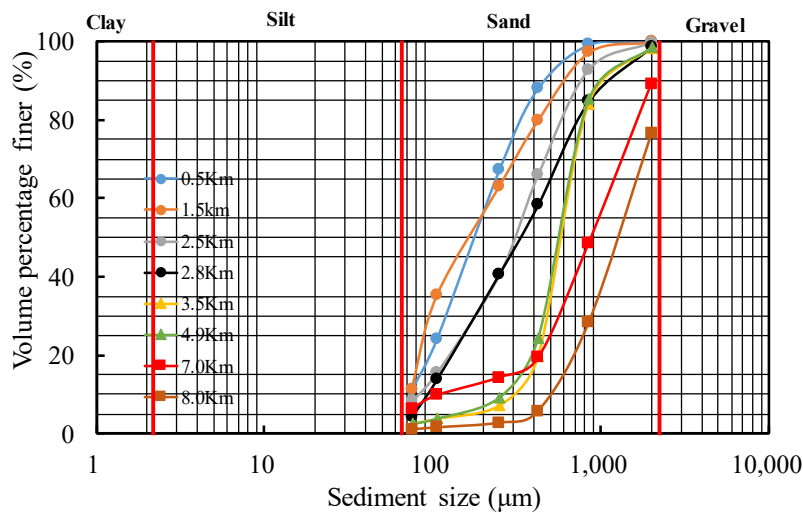


Figure 2.5 Grain size variations along the Otagawa floodway.

2.3.3 SSA results and Fast Fourier Transform (FFT) test

2.3.3.1 SSA results

As above stated, the SPMC varies remarkably in response to tides and streamflow. Unfortunately, these factors induce SPMC variability at comparable orders of magnitude and descriptive methods are not sufficient to compare their relative effects at different time scales. Compared to a qualitative interpretation, SSA is more rigorous approach for illustrating all temporal characteristics of SPMC variability and the corresponding environmental factors. SSA can be utilized not only to characterize SPMC variability, but also to determine the relative contributions of influencing factors to the total variation.

Before applying SSA, the SPMC time series was smoothly filtered

with a 1 h moving average to remove noise. There exists a small difference between the raw and filtered data. The R^2 values and root mean square errors (RMSEs) of four SPMC series of data ranged between 0.76 and 0.97 and between 0.10 and 0.27 mg/L, respectively. The SPMC data were decomposed into 10 modes by SSA (RCs, Figure 2.6). SSA was applied to the SPMC time-series data with a window size of 24 h. Once evaluated, each RC group was assigned to one or two control forcing frequencies.

At Stations B and C, RC1 contribute 96.9% and 94.5% of the data, respectively. The contributions of other modes to the SPMC variation are negligible. At Sta. A_R in summer, RC1 contributes 81.9% and RC2 accounts for 9.6% of the data, while in winter at Sta. A_C, RC1 and RC2 account for 73.6% and 19.5%, respectively. Thus, in the following discussion, we focus on analysis of the first RC at Stations B and C, and the first two RCs at Sta. A_R and Sta. A_C.

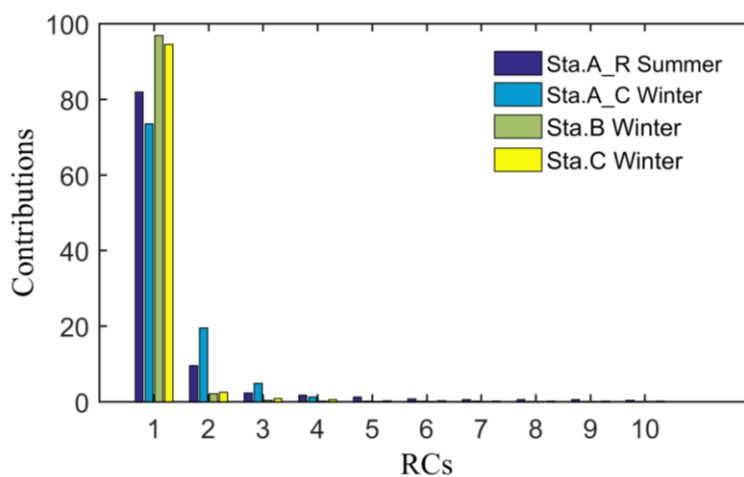


Figure 2.6 RC contributions to four SPMC time series: during summer at Sta. A_R from July 29 to August 16, 2007; during winter at Sta. A_C from January 6 to 26, 2008; during winter at Sta. B from December 22, 2007 to January 16, 2008; during winter at Sta. C from December 27, 2007 to January 10, 2008.

During summer, at Sta. A_R, RC1 accounts for 81.9% of the data, where the oscillations are similar in amplitude to the tidal velocity, and the positive RC1 values responded to the significant spring-neap tidal cycle (Figure 2.7a). RC2 accounts for 9.6% of the variation and varies negatively with the water depth and positively with the tidal current velocity (Figures

2.7b, 2.7c, 2.7e, and 2.7f), indicating the influence of the tidal velocity. According to this interpretation, it can be assumed that RC1 contains the variance of the spring-neap tidal cycle and RC2 contains the intra-tidal modification of the semidiurnal tide. Like the situation in summer, in winter at Sta. A_C, the first RC contributes 73.6% of the variation and varies positively with the spring-neap tidal cycle (Figure 2.8a), indicating the controlling role of the spring-neap tidal cycle. RC2 explains 19.5% of the variations that vary negatively with the water depth and positively with the tidal velocity (Figures 2.8b, 2.8c, 2.8e, and 2.8f).

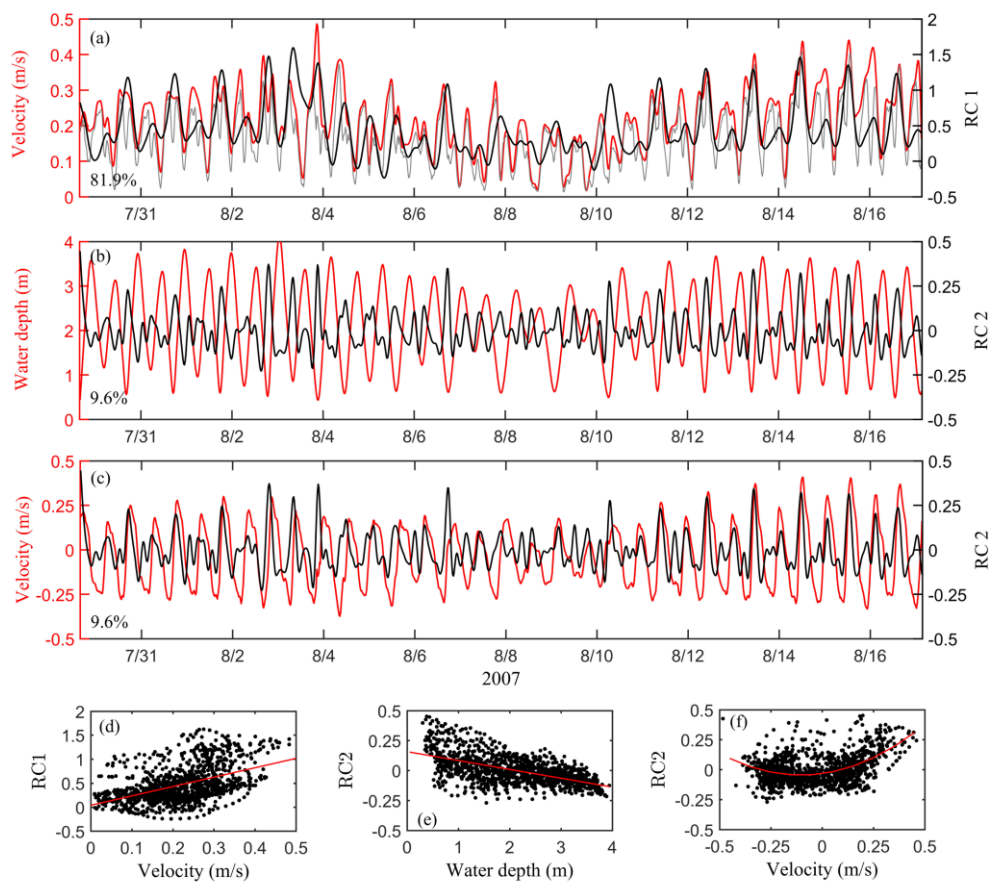


Figure 2.7 Comparisons of RCs to the temporal changes of the variables at Sta. A_R: (a) RC1 vs. velocity (the red line represents the envelope of the velocity and the gray line represents the original magnitude of the velocity), (b) RC2 vs. water depth, (c) RC2 vs. velocity, (d) regression diagram of RC1 and velocity amplitude, (e) regression diagram of RC2 and water depth, and (f) regression diagram of RC2 and velocity. The contribution of each RC to the total SPMC variability is written in the bottom left corner, and these two modes contain 91.5% of the total variance.

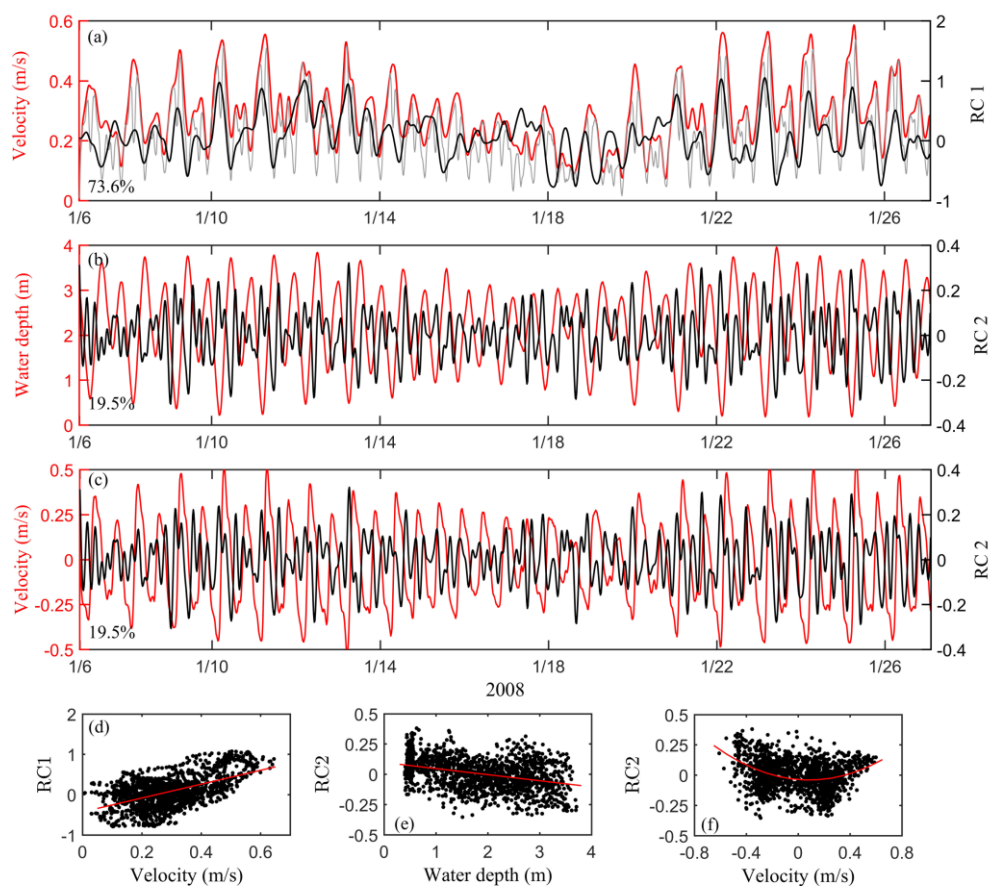


Figure 2.8 Comparisons of RCs to the temporal changes of the variables at Sta. A_C: (a) RC1 vs. velocity (the red line represents the envelope of the velocity and the gray line represents the original magnitude of the velocity), (b) RC2 vs. water depth, (c) RC2 vs. velocity, (d) regression diagram of RC1 and velocity amplitude, (e) regression diagram of RC2 and water depth, and (f) regression diagram of RC2 and velocity. The contribution of each RC to the total SPMC variability is written in the bottom left corner, and these two modes contain 93.1% of the total variance.

During winter, RC1 explains 96.9% and 94.5% of the variations at Stations B and C, respectively, and varies positively with the spring-neap tidal cycle (Figure 2.9), indicating the strong influence of the spring-neap tidal cycle. Since this component primarily describes the fluctuations of the velocity amplitude, this component can be interpreted as the spring-neap tidal cycle caused by the variations in tidal velocity, and the water column is destabilized by the tidal velocities. Thus, the bottom sediment will be resuspended by the bed shear stress and reenter the water column due to vertical diffusion.

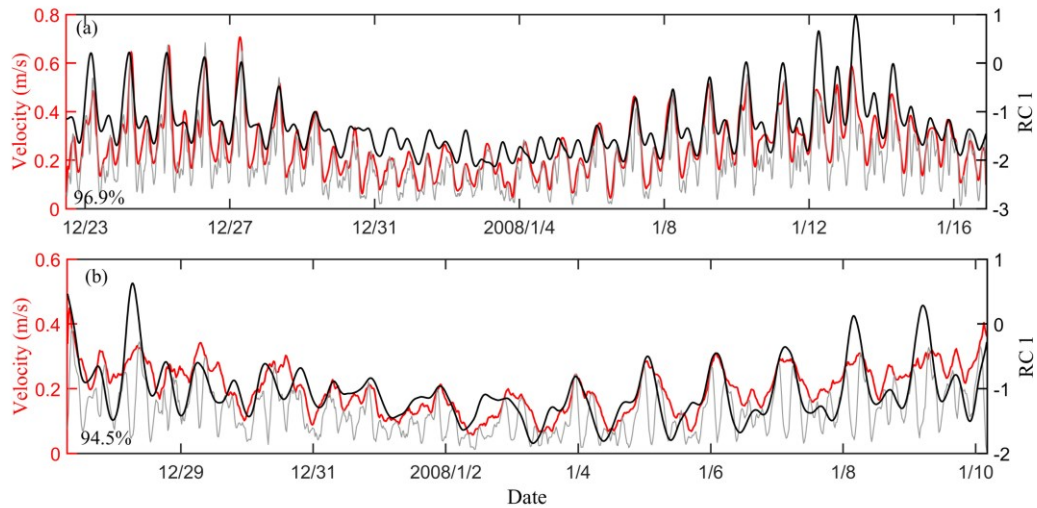


Figure 2.9 Comparisons of the RCs to the temporal changes in the variables at Stations B and C, including: (a) at Station B RC1 vs. velocity (the red line represents the envelope of the velocity and the gray line represents the original velocity), (b) at Station C RC1 vs. velocity (the red line represents the envelope of the velocity and the gray line represents the original velocity). The contribution of each RC to the total SPMC variability is written in the bottom left corner, where the first mode accounts for 96.9% and 94.5% of the SPMC variance at Stations B and C, respectively.

2.3.3.2 FFT test

Figure 2.10 illustrates the FFT power spectra of the original SPMC time series on a log-log plot. It shows that the main variability has time scales of (a) 24 h, and (b) 12 h. These time scales are easily linked to deterministic forcings: spring-neap tidal fluctuations and ebb-flood tidal flow.

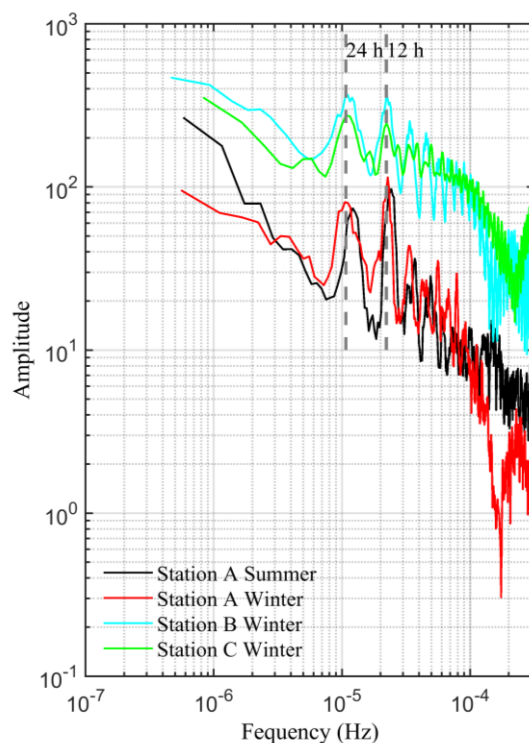


Figure 2.10 FFT power spectra of the original depth average SPMC time series.

In this study, the relative contributions of the driving forcings were investigated and their associated environmental forcings of the SPMC were demonstrated. The application of SSA and FFT confirmed the importance of tidal modulation on the SPMC during summer and winter. Additional information about these forcings will be comprehensively discussed later.

2.3.4 Spring-neap tidal cycle

The SPMC exhibits different variations during summer and winter, indicating the important role of tidal modulation. The Otagawa floodway is a tidally controlled estuarine system. The differences resulting from tidal mixing and stratification affect suspended sediment variations.

Commonly, the Simpson number is used as an indicator to demonstrate the intensity of tidal mixing [62]. The Simpson number is defined as the ratio of the potential energy change caused by tidal straining to the production rate of the turbulence kinetic energy (TKE). Therefore, the Simpson number is only useful in cases in which the horizontal gradients of the density and tidal velocity are known [63]. Neglecting the effects of the horizontal density gradients, the growth rate of the bottom

boundary layer can be parameterized similarly with the growth of a tidal velocity mixed layer. The following mixing indicator was proposed by Geyer and MacCready (2014) to count the efficiency of tidal mixing:

$$M^2 = \frac{C_d U_T^2}{\omega N H^2} \quad (1)$$

where C_d is the drag coefficient, U_T represents the amplitude of the tidal velocity, H is the water depth, ω is the tidal frequency, and

$$N = \sqrt{\frac{\beta g S_0}{H}} \quad (2)$$

where N is the buoyancy frequency and S_0 is the reference salinity. In this work, the mean salinity during each observation period was adopted as S_0 , g is the gravitational acceleration and was taken to have a constant value of 9.8 m/s^2 . $\beta = (\frac{\rho}{\rho_0} - 1)/s$ was used to estimate the instantaneous buoyancy frequency [63], where ρ is the instantaneous density, s is the instantaneous salinity, and ρ_0 is the reference density.

Tides	Amplitude (m)	Phase (°)
M_2	1.02	272.11
K_1	0.34	226.29
O_1	0.26	190.09
S_2	0.34	322.88

Table 2.1 Harmonic analysis of water level.

Applying these equations, the M values during summer and winter were calculated. Four major harmonic constants of the water level are shown in the Table 2.1. The water level data were obtained from the Kusatsu gauging station during the observation period. The M_2 tide dominated in the Otagawa floodway; thus, the estimated value of M was utilized for the M_2 tidal frequency. C_d was taken to be 0.0025 [63].

For brevity, the intra-tidal variations on the velocity and SPMC at Station A are narrated in detail, while the behaviors of the tidal current and SPMC at Stations B and C are only stated briefly.

2.3.4.1 Summer

During the spring tide, the velocity profiles at Sta. A_R indicate the

robust dominance of the semidiurnal tide. The ebb/flood velocities decrease from the surface to the bottom in the water column, and the tidal range is around 3 m (Figure 2.4e), indicating a mesotidal environment. During the flood phase, the velocities are directed upstream with maximum values reaching 0.5 m/s; in the ebb, the velocities are directed downstream with maximum values around 0.55 m/s (Figure 2.11a). The mean flood and ebb velocity durations are around 4.8 h and 7.2 h, respectively, with a 2.4 h difference in the water column. The ebb velocity and duration are greater than those during the flood tide, and the asymmetry can be attributed to the river runoff. Throughout our observations, the peaks of the bottom SPMC correspond to the peaks of the flood velocities just after the lower low water. In addition, the SPMC peaks match the peaks of M (Figures 2.11b and 2.11c). Thus, the SPMC fluctuations are enhanced by increased flood velocities and likely by the local resuspension of SPM in the water column.

During the neap tide, the tidal range at Sta. A_R decreased to around 2 m (Figure 2.4e). Compared to the maximum flood velocity during spring tide, the maximum flood velocity during neap tide (roughly 0.45 m/s) decreased by around 0.1 m/s. Meanwhile, the maximum ebb velocity was 0.55 m/s, which is almost equal to that during spring tide (Figure 2.11d). The mean flood (around 3.6 h) and ebb (around 7 h) durations exhibit a larger difference, indicating a larger tidal asymmetry. This larger asymmetry reveals the role of river discharge in summer and the weak tidal variation during neap tide. The SPMC peaks occur together with the dominant ebb velocities during the lower low water, possibly due to the river discharge transport (Figures 2.11d and 2.11e). In contrast to the spring tide, the local resuspension induced by flood currents decreases and most of the sediments stay near the bottom during the neap tide.

2.11i and 2.11j). The peak of M corresponds with the larger SPMC that appears around the lower low water, and with larger flood and ebb velocities simultaneously. It can therefore be considered that the increased tidal velocity turbulence caused a local resuspension of sediments in the water column.

The variations of the SPMCs and current velocities at Stations B and C during the spring and neap periods in winter are similar to those at Sta. A_C (Figure 2.12). During the neap period, high SPMCs are observable closer to the bed, and the SPMC peak occurs just after the low water. Meanwhile, during the spring tide, significant SPMC fluctuations occur just after the lower low water, together with the increased flood velocities.

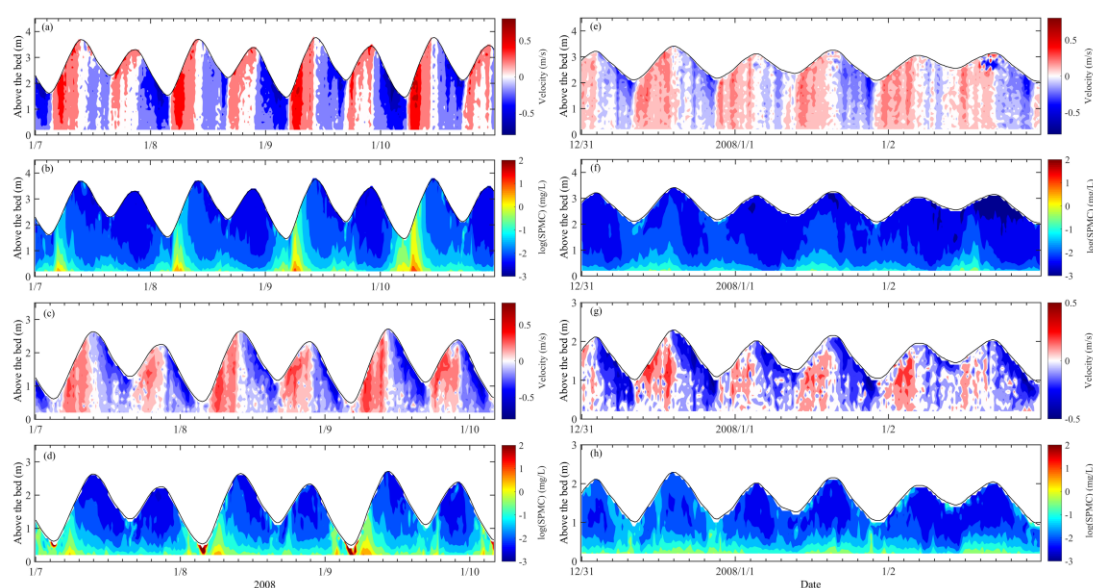


Figure 2.12 Temporal variations of the velocity profile (positive indicates flood, upstream) and SPMC, including (a) velocity and (b) SPMC at Station B during spring tide, (c) velocity and (d) SPMC at Station C during spring tide, (e) velocity and (f) SPMC at Station B during neap tide, and (g) velocity and (h) SPMC at Station C during neap tide.

The SPMC at all stations fluctuates with the ebb/flood velocities. The SPMCs are higher at the peaks of the flood and ebb tidal flows, indicating the dominance of local resuspension on the SPMC variations. The spring tides match the occurrence of higher SPMC, whereas neap tides correspond to times of lower SPMC. This behavior is a result of higher tidal velocities during spring tides, which increases the availability of SPM within the

brackish water column.

2.3.5 Relationship between SPMC and water discharge

Owing to the complex interactions between the tidal hydrodynamics, erodibility, and sedimentation, it is difficult to capture the essential information for the study of the role of tidal velocity and water discharge from Gion gates. Hence, to describe and capture the differences in the tidal transport of suspended sediments in the water column, the water column was divided into three vertical layers with similar thicknesses according to the instantaneous cell numbers of ADCP data. The average values (velocity and SPMC) within each layer (bottom, middle, and surface) were used to calculate the SPM transport.

In most cases, the river runoff is limited by the Gion sluice gates. During summer, well-mixed conditions are observable at spring tide for low river discharge $Q_{\text{Yaguchi}} < 110 \text{ m}^3/\text{s}$ ($Q_{\text{Gion}} < 24 \text{ m}^3/\text{s}$) (Figures 2.2 and 2.13c). As depicted in Figure 2.13a, the vertical SPMC distribution is scattered considerably during low discharge ($Q_{\text{Yaguchi}} < 110 \text{ m}^3/\text{s}$) and moderately during mid-flows ($110 < Q_{\text{Yaguchi}} < 250 \text{ m}^3/\text{s}$). Meanwhile, it is obvious that the SPMC varies smoothly during significant discharge periods ($Q_{\text{Yaguchi}} > 310 \text{ m}^3/\text{s}$). During winter, most of water discharge (Q_{Yaguchi}) is lower than $110 \text{ m}^3/\text{s}$ ($Q_{\text{Gion}} < 24 \text{ m}^3/\text{s}$) (Figures 2.13b–2.13d). For each station, the SPMC and discharge are weakly correlated, and the SPMC has many comparable values within each layer.

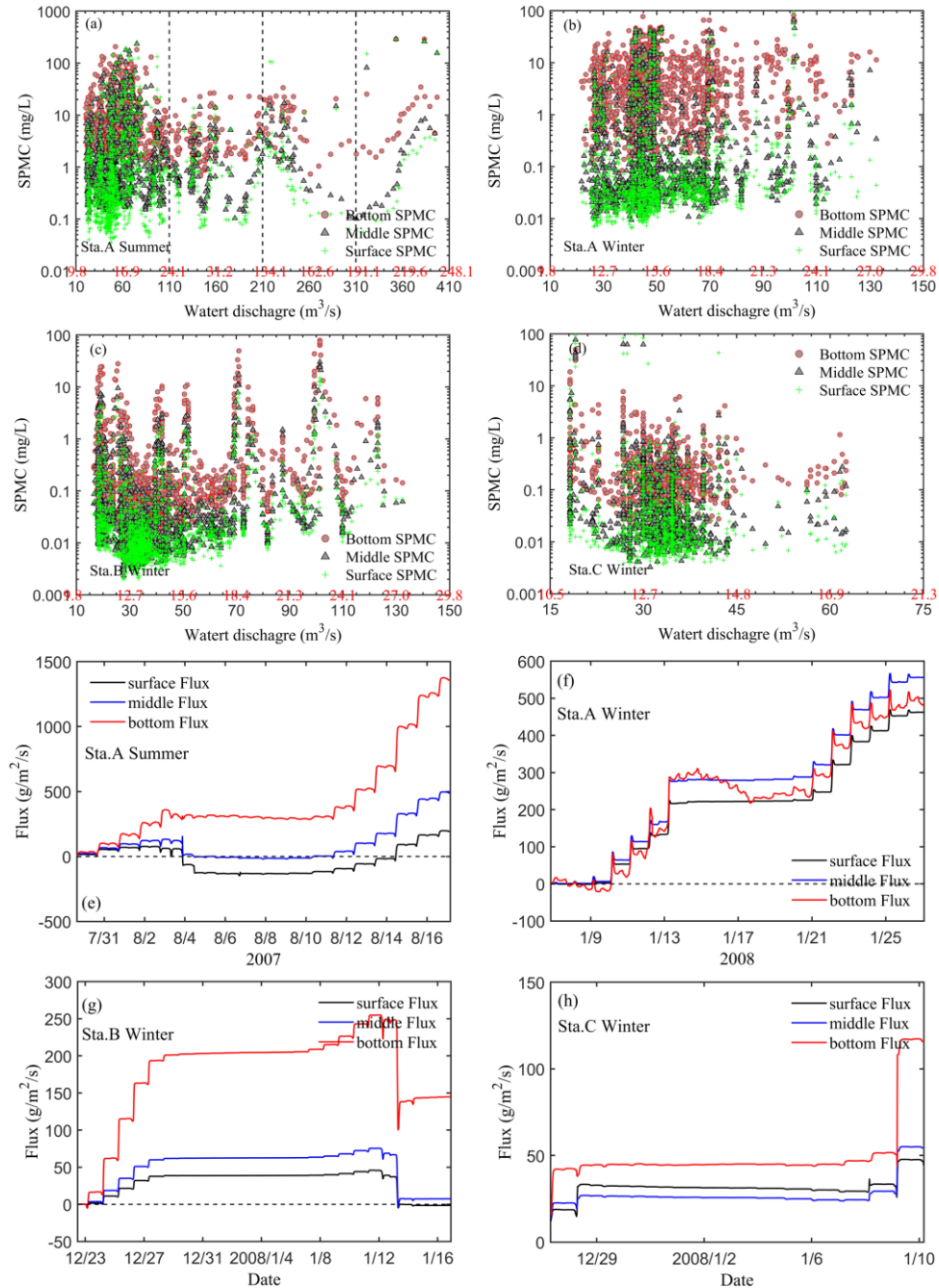


Figure 2.13 (a)–(d) Scatter diagrams of SPMC and water discharge within three layers; (e)–(h) SPMC cumulative flux in three layers: (a) and (e) during summer at Sta. A_R from July 29 to August 16, 2007; (b) and (f) during winter at Sta. A_C from January 6 to 26, 2008; (c) and (g) during winter at Station B from December 22, 2007 to January 16, 2008; (d) and (h) during winter at Station C from December 27, 2007 to January 10, 2008 (positive: upstream direction, landward; negative: downstream direction, seaward).

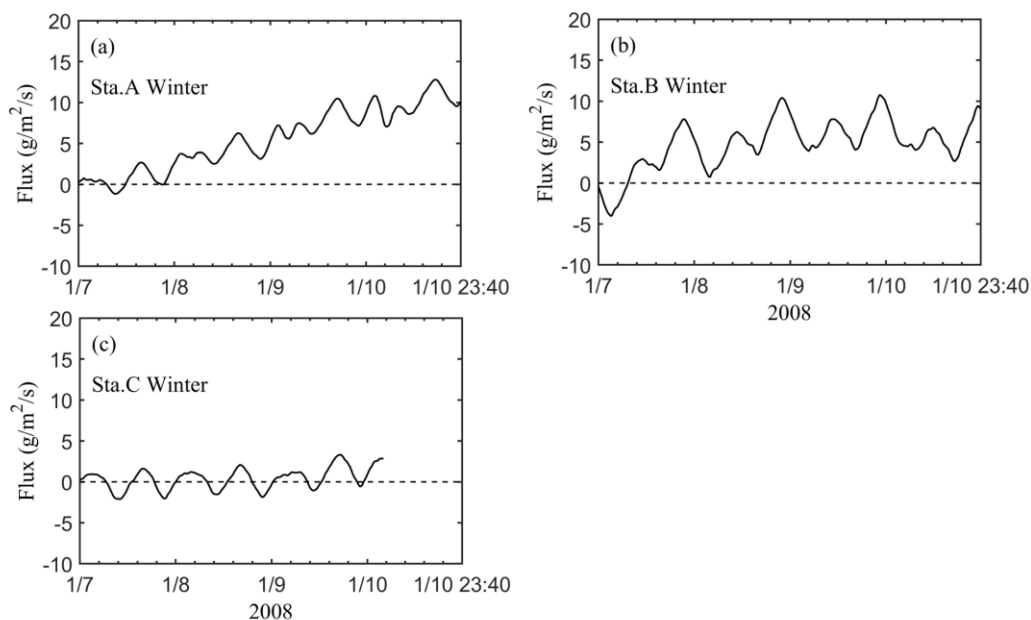


Figure 2.14 Comparison of SPMC cumulative flux at Stations A, B, and C during January 7–10, 2008.

During winter, in the case of low river discharge, Stations A, B, and C were mostly under the influence of tidal asymmetry. Tidal asymmetry causes flood velocities to be slightly dominant, and more sediments are resuspended, promoting significant upstream transport. Tidal transport at the three sites is directed upstream with magnitudes decreasing in the order of $A > B > C$, indicating that the sediment migration resulting from tidal hydrodynamics decreases from downstream to upstream (Figures 2.13f–2.13h). In contrast, during summer, significant water discharge is evident from August 4 to 6, and the role of water discharge transport is highlighted (Figure 2.13e). Seaward currents dominate during most of the tide, and the massive seaward transport of sand is produced during flood events. The significant feature is that the increased water discharge exerts an effect on suspended sediment transport and shifts the suspended sediment seaward. During winter, upstream tidal pumping at Station A dominates in the water column (Figure 2.13f). At Stations B and C, the bottom layer exhibits upstream tidal pumping during the flood tide, while in the middle and surface layers, due to the bed slope and tidal asymmetry of the flow, downstream tidal pumping exists and counteracts part of the upstream sediment flux during the ebb tide (Figures 2.13g and 2.13h).

2.4. Discussion

2.4.1 Role of tidal velocity and water discharge

Within tidal rivers, the interplay of the bed shear-stress and particle dynamics is key to understanding the effects of fluvial and marine influences on sediment transport and morphological development. In this study, we depended on the previous works that addressed flow, tide, and particle dynamics in the Otagawa floodway [51], [53] to assess the potential effects considering the river flow and tidal velocity.

2.4.1.1 Low water discharge

Processes that determine suspended particle dynamics in estuaries are functions of the turbulence intensity and suspended sediment load. The Otagawa floodway is characterized by moderate energy, low sediment concentrations, and stochastic events. The flocculation and resuspension of sediments are basically dominated by the processes associated with tidally induced shear stress followed by TKE production and dissipation [53]. The particles showed different proportions between downstream and upstream (Figure 2.5). Suspended particles are related to tidally induced shear stress at any single location, but the suspended sediment load shows a strong dependence on local sediment availability. Accordingly, the lower reach is supposed to experience more erosion and the upper reach will experience deposition.

For the low river discharge conditions, during spring tide, the mixing indicator M (Figure 2.11) shows that the mixing is enhanced, with increased tidal range and velocities, and stratification is reduced. Our observations indicate that during these periods, the SPM at the lower and middle floodway is largely controlled by cyclical processes (resuspension, deposition, mixing, and upstream transport) driven by spring-neap fluctuations and ebb/flood velocities. At neap tide and low river flow, horizontal advection governs the SPMC [64]. Uncles et al. (2002) indicated that the gravitational circulation at the lower estuary acts to concentrate the sediment at the estuary turbidity maximum (ETM), through an upstream flux of deeper suspended material. In this study, significant tidal asymmetries evidenced the importance of tidal pumping for SPM transport.

Typically, most of the suspended material deposits at slacks, and resuspension with flood velocities are limited at neap tide. Wang et al. (2019) reported that water-sediment regulation schemes can change the tidal asymmetry and sediment transport. After the construction of channel regulation mechanisms in the Yangtze Estuary, the high-SSC area was enlarged and moved offshore. The Otagawa floodway acts as a freshwater regulation scheme, and the SPMC is well associated with tides. These processes promote sediment retention in the channel and reduce supply to the coast during the low-discharge season.

2.4.1.2 High water discharge

For high river discharge, significant tidal asymmetry in ebb/flood durations and velocities was observed (Figure 2.2e). Scully and Friedrichs (2003) showed that a stronger tidal asymmetry on the ebb may act as a barrier that limits sediment suspension. This process may produce seaward pumping of suspended sediment (Figure 2.13e). Ferreira et al. (2003) found that in the Guadiana River estuary, the ETM maintains its position for river discharge up to at least $250 \text{ m}^3/\text{s}$ and suggested that the estuarine response to higher river discharge is buffered by the increasing stratification. In contrast, in the Tamar and Weser estuaries, Grabemann et al. (1997) showed that the ETM exhibited larger spatial variations and it is related to the variations with the river outflow. In light of the aforementioned ideas, it can be concluded that under high river discharge, flood currents were reduced, and freshwater inputs reinforced ebb currents (especially near the surface), causing the SPMC to increase rapidly. The observation results also indicated that when the river discharge (Q_{Yaguchi}) reached up to $400 \text{ m}^3/\text{s}$ ($Q_{\text{Gion}} = 242 \text{ m}^3/\text{s}$), the SPMC maximum was located at the lower reach and promoted a transient downstream transport (Figure 2.13). The discharge from upstream and saltwater intrusion formed a two-layer structure with reduced vertical sediment diffusion and enhanced sediment-induced stratification.

2.4.1.3 Water circulation

Estuarine circulation is a major mechanism for tidal transport in partially mixed estuaries [65]. Following the classical theory of estuarine

circulation, the bottom current is expected to flow landward in a salt wedge estuary due to the salinity gradient. The pressure gradient force $-\frac{1}{\rho_0} \frac{\partial \rho}{\partial x}$ is controlled by the combined effect of the seaward barotropic component $-g \frac{\partial \zeta}{\partial x}$ and the landward baroclinic component $-\frac{g}{\rho_0} \int_z^\zeta \frac{\partial \rho}{\partial x}$ that increase with depth. In the Otagawa floodway, with the lower river discharge $Q_{\text{Yaguchi}} < 110 \text{ m}^3/\text{s}$ ($Q_{\text{Gion}} < 24 \text{ m}^3/\text{s}$), the landward baroclinic term could suppress the seaward barotropic term. The tidal straining is critical in modifying the density structure at the saltwater wedge. Bottom water can overlap with the surface freshwater runoff via tidal straining and induced unidirectional upstream sediment transport during spring tide. On the other hand, for high river discharge $Q_{\text{Yaguchi}} > 310 \text{ m}^3/\text{s}$ ($Q_{\text{Gion}} > 191 \text{ m}^3/\text{s}$), saline water was flushed out from the upper reach. The stratification vanished around the low water and remarkable downstream transport was shown [69], with the water regime transiently transitioning from tidally dominated to river dominated conditions. In the downstream region, the saltwater wedge still existed and could intrude through flood tides. The landward baroclinic term suppressed the seaward barotropic term; therefore, stratification existed around the high water.

2.4.2 Capture depocenter

Estuarine systems that have stronger flood currents than the ebb velocities (so-called tidal asymmetry) are more likely to accumulate sediments in their upper reaches. This characteristic is the result of enhanced resuspension and transport processes that occur during the flood tide period (so-called tidal pumping). Tidal oscillation effects are strong under low discharge conditions, with magnitudes decreasing in the order of $A > B > C$ among the three stations in winter and contributing to decreased upstream sediment transport from Station A to Station C. Uncles et al. (2002) reported that long microtidal estuarine regimes can have extensive “intrinsic” SPM concentrations, and the storage mechanisms produce maximum turbidity areas in the upper reaches of numerous tidal estuaries. The long microtidal estuarine regimes are under limited low discharge situations and are left with substantial amounts of sediment materials influenced by tidal hydrodynamics that increase over the long

term.

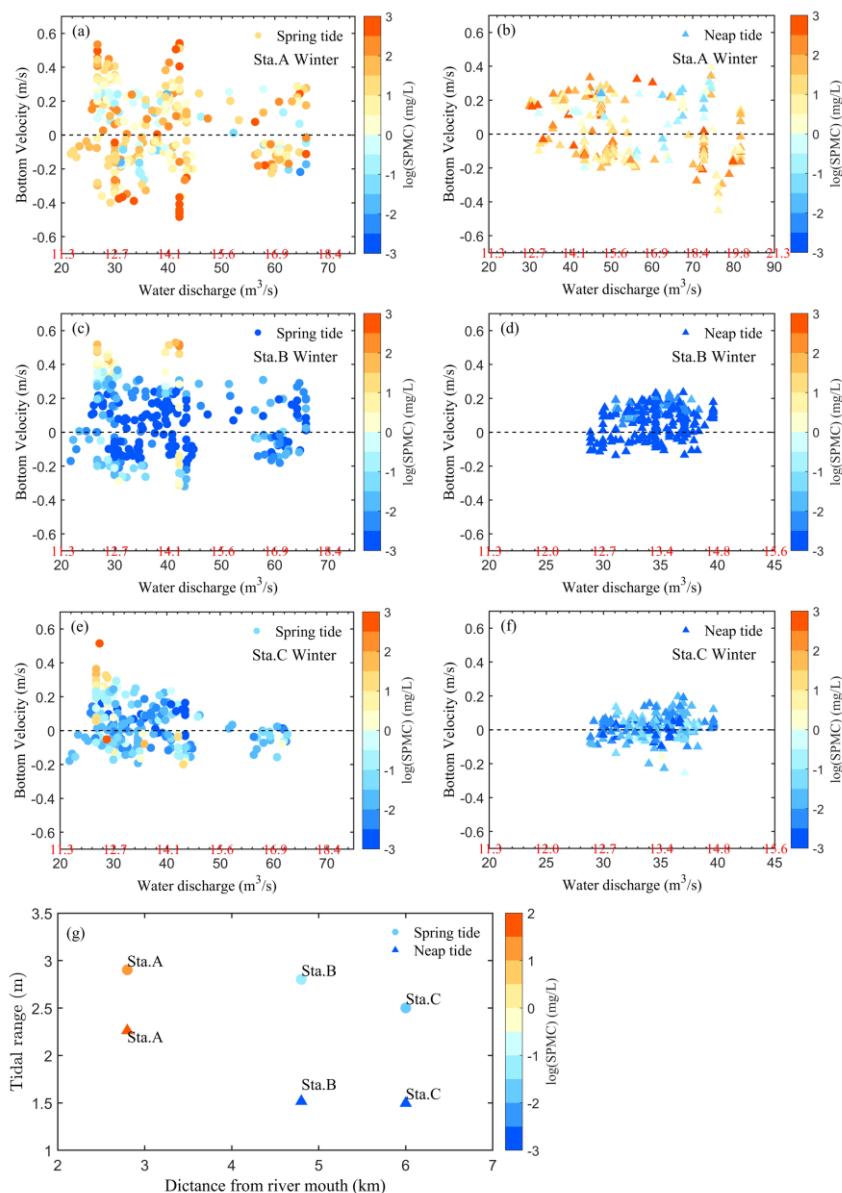


Figure 2.15 Bottom tidal velocity vs. water discharge and SPMC for three stations during spring/neap tide period during winter and distribution of spring/neap tidal averaged bottom layer SPMC vs. tidal range at three stations during winter.

A comparison of the spring/neap tidal averaged bottom layer SPMC is shown in Fig 2.15. The higher SPMC at Station A is closely associated with the bed resuspension, while the lower SPMCs at Stations B and C indicate the weak resuspension process within either spring or neap tide (Figure 2.15). The tidal range decreases with the distance from the river

mouth ($A > B > C$). During both the spring and neap tide periods, the SPMC at Station A is higher than those at both Stations B and C. The SPMC magnitudes have the relationship $A > B \approx C$. For the Otagawa floodway, considering sediment flux continuity, short-term sediment deposition occurs with the tidal pumping, most of the sediments are under the upstream transport and are deposited between Stations A and B during spring tide. On the other hand, during neap tide, most of the sediment undergoes local resuspension and settling.

The pattern of upstream transport is predominant in the lower and middle parts of the floodway during prolonged periods of low river runoff. Strong tidal asymmetry in velocity and duration can be dominant in driving sediment transport. From this work, short-term sediment deposition occurs along the area located between 2.8 km and 4.8 km from the mouth. However, the sediment load is exported to the near shore on a yearly to centennial scale [19], [70]. More frequent low-discharge events enhance aggregation, settling, and trapping within the floodway.

2.4.3 Occurrence of convergence zone (CZ) in the tidal floodway

CZ location prediction is necessary in floodways and is of particular importance in order to improve regional sediment management. In the present work, based on the seasonal and spatial properties of the SPMC that were discussed in the previous sections, it was necessary to find the CZ between tidal and river forcings that occur along the floodway. The position of the depocenter along the floodway depends mainly on the tidal and river forcings, as already discussed in section 2.4.2. Under tidal control, most of sediment deposition occurs in the area between 2.8 km and 4.8 km from the mouth. To understand the relationship between the SPMC and river flow more fully, Figure 2.16 depicts the SPMC as a function of the river discharge (in $20 \text{ m}^3/\text{s}$ intervals) at Station A

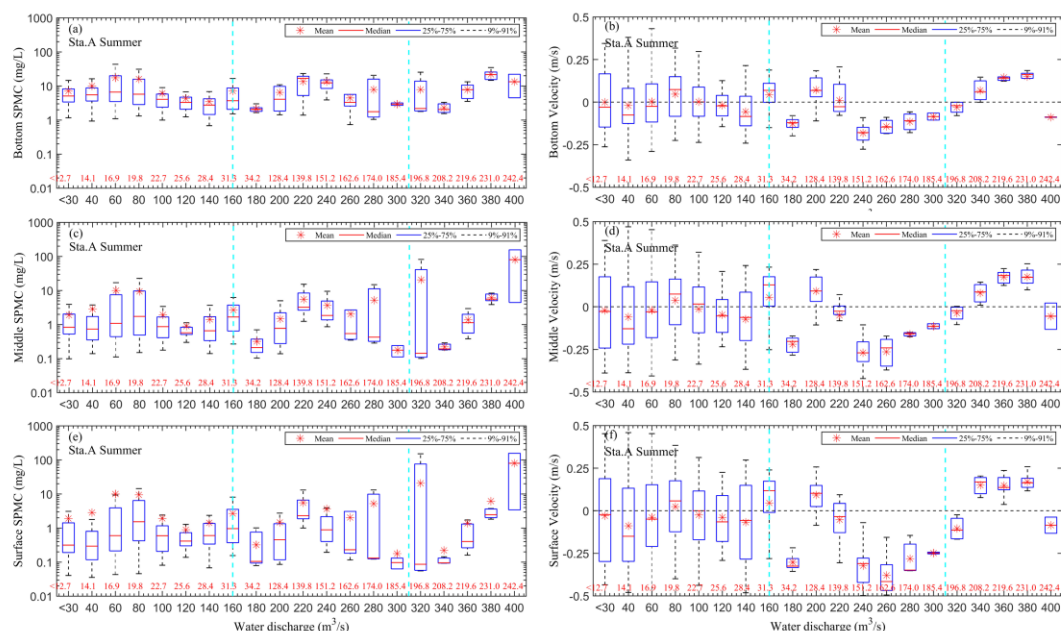


Figure 2.16 Mean (red cross), median (red bars), 25–75th percentile (blue bars), and 9–91st percentile (black bars) values of each layer-average SPMC (bottom, middle, and surface) in 20 m³/s intervals of water discharge at Station A.

Determining the precise discharge threshold of CZ installation per station is challenging due to a large SPMC variability. Differences between the velocities during the periods of decreasing and increasing river flow are also notable in the floodway (Figures 2.16b, 2.16d, and 2.16f). For discharge (Q_{Yaguchi}) less than 160 m³/s ($Q_{\text{Gion}} < 31$ m³/s), the small variations in the SPMC and velocities are associated with the highest potential for promoting CZ installation. Thus, the tidal pumping effect and river forcing converge around 2.8 km upstream from the river mouth. Discharge (Q_{Yaguchi}) greater than 160 m³/s ($Q_{\text{Gion}} > 31$ m³/s) can considerably promote CZ installation with dominant seaward currents, and large SPMC variation with one order of magnitude occurred in three layers. When discharge (Q_{Yaguchi}) greater than 310 m³/s ($Q_{\text{Gion}} > 191$ m³/s) seems to ensure complete CZ installation, significant variability from middle and surface layer SPMC is observable (blue bars varied from 0.1 to 100). Meanwhile, the SPMC is stable in the bottom layer. Within the bottom layer, the SPMC remains stable under tidal forcings, while in the middle and surface layers, the SPMCs show notable variations owing to the river forcings.

The effect of river discharge is assumed to be the primary factor in the

occurrence of CZ. However, morphological changes (natural or anthropogenic) may also contribute to the CZ intensification [22], by amplifying the tidal asymmetry and hence enhancing the trapping of sediments. The existence and importance of these changes in the floodway could cause problems with the river flow in the foreseeable future, and it is necessary to investigate these issues further.

2.5. Conclusions

The relative effects of environmental forcings on the SPMC were evaluated on a seasonal scale by SSA, which is a powerful method for determining the contributions of environmental forcings on the SPMC. In summer, the ebb/flood velocities forcing (RC2) at Sta. A_R explained 9.6% of the variance, together with the contribution of the spring-neap tide oscillation (RC1, 81.9%). In winter at Sta. A_C, when the discharge was low and controlled by the Gion gates at upstream, the spring-neap tide oscillation (RC1) contributed 73.6% of the SPMC variance, together with the 19.5% of variance from the ebb/flood velocities (RC2). In contrast, at Stations B and C, most of the variance (up to 94.5%–96.9%) was contributed by the spring-neap tidal cycle. The detailed analysis based on the spring-neap tidal cycle with raw time-series data during summer and winter at Station A revealed the effects of ebb/flood currents. Spring tides matched the occurrences of higher SPMC and significant SPM upstream transport, whereas neap tides corresponded to times of lower SPMC and insignificant SPM transport. These characteristics are the results of higher tidal velocities during spring tides, which increase the availability of SPM within the brackish water column.

In the case of limited river runoff, the domain effects of oscillations related to the spring-neap tide cycle and flood-ebb cycle (reciprocating tidal velocity) on the SPMC variability along the Otagawa floodway were highlighted. Moreover, the role of discharge transport at less than $110 \text{ m}^3/\text{s}$ ($Q_{\text{Gion}} = 24 \text{ m}^3/\text{s}$) (winter and summer) demonstrated that tidal pumping has a domain effect on sediment shifting, while significant sediment seaward shifting results from flood events. Furthermore, a sort of “convergence” between tidal and river forcings seems to occur in the floodway. Upstream transport was observed with tidal pumping in most cases, while significant seaward transport corresponded to episodic flood events.

Although this study is a case-specific example of the Otagawa floodway, the presented results and discussion demonstrate the dynamics and mobility of SPM under tidal hydrodynamics in water discharge limited by artificial sluice gates. The results obtained in this study can be considered to contribute to increasing understanding of sediment dynamics in estuarine systems.

Chapter 3: Mapping tidal currents at a shallow tidal channel junction using the fluvial acoustic tomography system

3.1. Introduction

Examining the structures of tidal currents in tidal rivers is of great importance as tidal rivers can extend tens to hundreds of kilometers inland and are extensive in length and area [16]. Large multi-channel systems, such as the Yangtze River estuary [5], are often studied because of their high discharge and sediment transport rates. Small multi-channel systems with limited river discharge and mesotidal characteristics were studied previously by Danial et al. (2019). The stage-discharge relationships in small tidal rivers are not reliable as they are subject to unsteady flow conditions, as investigated in the study by Kawanisi et al. (2010) and others [10]. Moreover, the velocity distribution in the cross-section is complex and unsteady due to the combination of the runoff and the saltwater intrusion [11]. Studies relying on 2D data with a visual means of determining the spatiotemporal difference of velocity are helpful to better understand the process of tidal currents.

River-tide interplays in small multi-channel networks modify the topography in terms of both width and depth. For one tidal channel, the average tidal friction along the channel is primarily balanced by a subtidal pressure gradient [71]. Consequently, river-tide interplays induce a water level setup, which becomes larger further upstream. For multi-channels, a mismatch occurs at the bifurcation between the water level setups. If the water level setup resulting from the river-tide interaction in one of the channels is larger than that in other channels, this would facilitate the allocation of river flows to other channels [32]. The water division at the junctions leads to variation of the hydraulic geometry (HG) in multi-channels, and gradually modifies the topography in terms of width and depth. HG is a series of empirically derived power law relationships among the width, depth, flow velocity, and the discharge conveyed by the channel. Studies on HG relationships could help to understand how the morphology

of multi-channels is affected by river and tides. Studies on tidal distributary networks usually focus on issues with numerical models, because the system is complex and it is impossible to monitor the temporal and spatial scales comprehensively [29], [30], [72]. Moreover, calibration and validation of estuarine hydrodynamic models usually utilize the water levels and velocities recorded from several gauging stations or from the deployment of Acoustic Doppler Current Profilers (ADCPs) [30]. Traditional observation methods with fixed or moving-boat ADCPs are only capable of acquiring data on the velocity behaviors at one/several sites or sections, thus it is difficult to detect the rapid processes of tidal current patterns using them. However, the horizontal distribution and spatiotemporal variation of velocities can be efficiently reconstructed by the inverse method using the fluvial acoustic tomography (FAT) system [73], which also provides continuous high-quality measurements of discharge. Tidal rivers are regions in which exchange occurs between the river flow and saltwater intrusion, and the spatial and temporal variations of salinity can significantly affect residual currents via gravitational and tidal straining circulation in the systems [34], [62]. The FAT system [9], [40] is a promoted application of coastal acoustic tomography (CAT) [39] that can be utilized in shallow waters to investigate shallow currents in riverine and tidal environments. Hence, continuous and long-term monitoring of 2D tidal current and salinity fields at a shallow tidal junction with FAT is required for scientific analysis. Series data of the 2D flow velocity are helpful to better study the HG, while also providing a visual means of determining flow division and spatiotemporal differences of velocity and salinity.

In this study, we performed a monitoring program over one month with six FAT systems at a shallow tidal junction in Hiroshima, Japan, in 2020. This research aimed to characterize the tidal regime in terms of the continuous 2D tidal current and salinity fields at the shallow tidal junction using FAT and demonstrated the response process of river-tide dynamics at the tidal junction. An enhanced understanding of the process of tidal currents propagation and flow division in small shallow tidal junction is essential to better manage multi-channel networks and to understand the river flow dynamics in multi-channels.

3.2. Study area and methods

3.2.1 Study area

The Ota River is a network with several tide-dominated channels that flows through Hiroshima, west of Japan. The Ota River bifurcates into two major branches ~9 km upstream from the mouth (Figure 3.1a). The runoff in the Otagawa floodway is controlled by rows of Gion sluice gates, whereas the runoff in Kyu Ota River is controlled by two different gates at Oshiba (Figure 3.1a): the fixed weir is 86 m wide, and three sluice gates control the width of 13.33×3 m and are continuously open throughout the year. The tidal junction studied in this work is situated in the mid-reach of the Ota River, ~2.5 km downstream from the Oshiba gates and ~5.8 km upstream from the river mouth; the junction is under the influence of saltwater intrusion and the freshwater discharge.

The shallow tidal junction involves three branches (Figure 3.1): i) upstream (Kyu Ota River) is the northern branch; ii) downstream (Kyu Ota River) is the eastern branch; iii) the Tenma River is the western branch. The lengths from the mouth to the junctions of the eastern and western branches are ~5.4 km and ~6.2 km, respectively. For the western branch, the maximum and minimum widths are ~255 m and ~47 m, respectively, with a mean width of ~150 m; for the eastern branch, the maximum and minimum widths are ~259 m and ~60 m, respectively, with a mean width of ~160 m. Danial et al. (2019) reported that the Kyu Ota River is deeper and wider than the Tenma River. Riverbed levels for the eastern and western branches were ~-3 T.P. m and ~-2 T.P. m, respectively; the unit T.P. m is the height above the mean sea level in Tokyo Bay. The northern branch is wider than both the eastern and western branches, and the riverbed level varies from -2.5 to -3.0 T.P. m. The area near the branch S5-S6 is shallow, with bed levels varying from -0.5 to -2 T.P. m (Figure 3.1b). The mean water depths recorded at three ADCPs (S1, S3, S5) during the observation period were ~1.4 m, ~1.8 m, and ~2.1 m, respectively (Figure 3.1c). In general, owing to the frequent intrusion of saline water, freshwater discharge, geometrical shape of branches, and irregular topography, the surveyed area is characterized by unsteady and complex flow distributions.

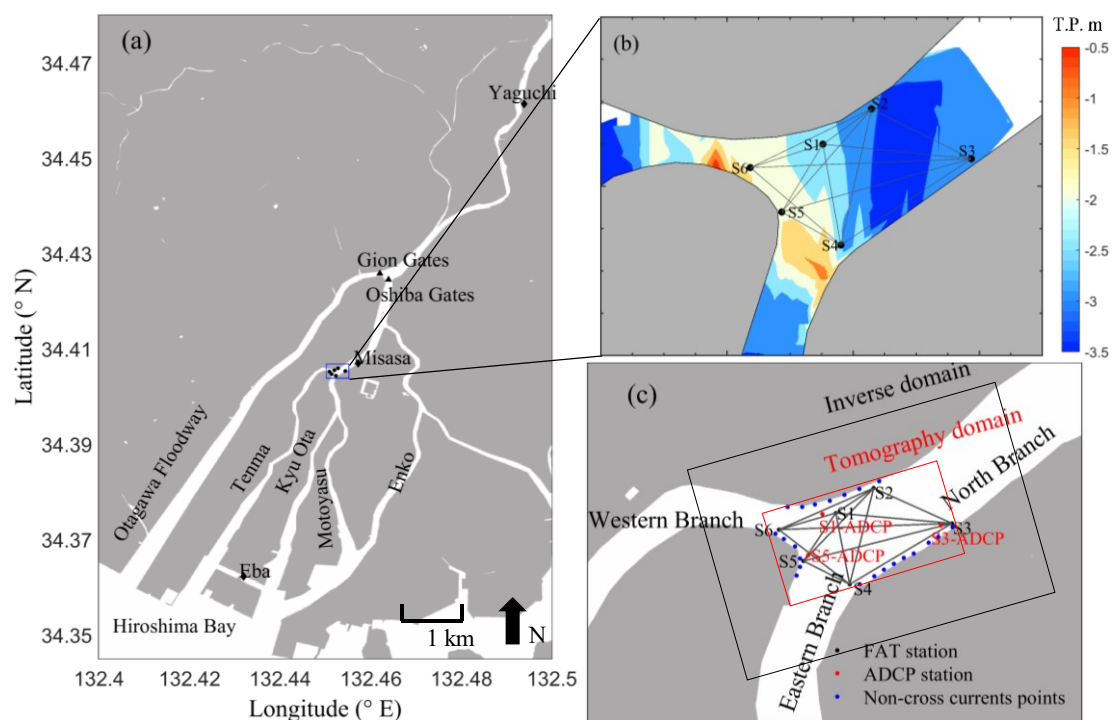


Figure 3.1 (a) Ota River; (b) bathymetry at the junction; and (c) locations of the fluvial acoustic tomography (FAT) system stations (S1-S6; black dots) and fixed Acoustic Doppler Current Profiler (ADCP; red dots) stations. Acoustic paths among the FAT stations are denoted by solid black lines. The unit T.P. m is the depth with respect to the mean water level in Tokyo Bay.

3.2.2 Instruments

FAT observations were carried out for ~ 34.4 days (February 21–March 26, 2020), which covered two fortnightly tidal cycles. Six FAT transducers were placed along the riverbanks in an area almost 310 m long and 170 m wide (Figure 3.1c). Simultaneous reciprocal transmissions were conducted along 14 transmission lines. During the observation period, acoustic signals with a 30-kHz central frequency were transmitted simultaneously from each source and were then received by the other stations every 1 min. The transmitted sound was modulated by an M-sequence with the 9th order, increasing the processing gain by ~ 27.1 dB. M-sequence is a type of pseudo-random sequence whereby the carrier signal is modulated with irregular time intervals by the phase shift of π [74].

The successful percentages of sound transmission data along 14 rays varied from 19–92% (Figure 3.2). Missing data during the observation

period were mainly induced by the irregular and shallow region, where the rays were unable to arrive at the receivers because of the transmission losses due to multiple reflections from the water surface and riverbed. The travel time difference data were smoothed by a 30-min low-pass filter to erase the effects of the high-frequency noise and was then utilized in the inverse problem to estimate the 2D current fields. The mean relative error (MRE) and root mean squares difference (RMSD) between the 1-min original and 30-min low-pass filtered travel time fluctuated as 1.5–10.1% and 0.013–0.045 ms, respectively. The RMSD values caused errors in velocity that ranged from 0.08 to 0.13 m/s for all the station pairs, with a mean sound speed of 1456 m/s and constant station-to-station distances.

Three 2-MHz ADCPs (Aquadopp Profiler, Nortek) were used to observe the velocities and validate the inverted 2D velocities, with a 1-min average interval, a 2-min sampling interval at stations S1-ADCP and S3-ADCP (Figure 1c), and a 5-min sampling interval at station S5-ADCP (Figure 1c). The bin size and blank distance were set to 0.1 m. The bin number was 50. Owing to the difference in battery life and data storage capacity of each ADCP, observations close to stations S1, S3, and S5 were only performed on February 21–March 9, February 21–March 13, and February 21–March 7, respectively. However, the locations of the ADCPs may have been inappropriate because they were located near the boundary of the tomography area.

During the observation period, S1-ADCP and S5-ADCP were attached to a conductivity–temperature–depth sensor (Compact-CTD, JFE Advantech) near the bottom (~0.1 m above the bottom [mab]) to measure salinity, temperature, and depth. S3-ADCP and station S2 (~0.1 mab) were attached to the conductivity–temperature (CT) sensor to collect salinity and temperature. Due to the difference in the battery life of each sensor, observations close to stations S1-ADCP, S2, S3-ADCP, and S5-ADCP were only performed on February 21–March 2, February 21–March 26, February 21–February 29, and February 21–February 25, respectively. Along with the FAT measurements, several routes of Teledyne RDI StreamPro ADCP were selected along four transects (S1–S3, S1–S6, S3–S5, S4–S5) to provide reference velocity data on March 6, 2020. All data were referenced to bottom tracking. Each transect was positioned across the river with each end near the banks.

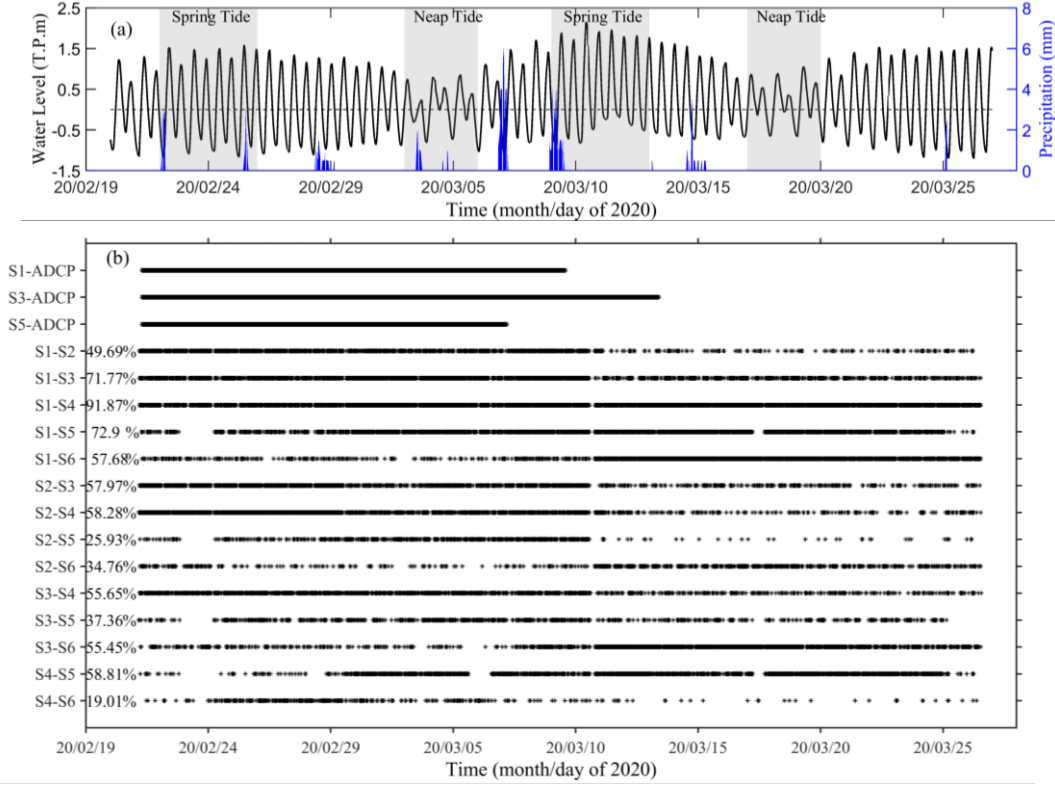


Figure 3.2 Synchronized fluvial acoustic tomography (FAT) system and Acoustic Doppler Current Profiler (ADCP) measurements: (a) Water level data (monitored at the Misasa gauging station) and precipitation data (acquired from the Japan Meteorological Agency); (b) observation periods of the fixed ADCP and time schedules of the successful percentages of reciprocal sound transmission between each settled station pair. The shaded regions represent the spring/neap periods during the observation period.

3.2.3 Theoretical analysis of the inverse method

3.2.3.1 Forward problem

Between two acoustic stations, the sound travel time along the reciprocal ray path Γ_{\pm} can be written as:

$$t_i^{\pm} = \int_{\Gamma_{\pm}} \frac{ds}{c_m + \delta C(x,y) \pm u(x,y) \cdot n_i} \quad (3)$$

where $+/-$ denotes the direction of sound propagation; C_m denotes the mean sound speed; δC denotes the sound speed deviation relative to C_m , u is the velocity; n_i is the unit vector along the ray; and ds represents the increment of the arc length along the ray. We assumed that the two-way path geometry was reciprocal and that $\Gamma_{\pm} \approx \Gamma$ in order of $|u|/C_m \ll 1$ and

$\delta C/C_m \ll 1$. The difference and summation of the travel time can be expressed by:

$$\Delta t_i = (t_i^+ - t_i^-) \approx -2 \int \frac{u \cdot n}{c_m^2} ds \quad (4)$$

Equation (4) is a couple of integral equations with unknown parameters, u , and can be solved by the inverse method.

3.2.3.2 Inverse problem of 2D currents

FAT observes the travel time of sound between the acoustic stations. By relying on the travel time differences of the acoustical station pairs, the horizontal distributions of the depth-averaged current can be effectively mapped by the inverse analysis. The inverse method has been employed in a range of previous studies on currents [73], [75]–[80]. In a simplified explanation, the inverse method introduces a stream function to reconstruct the 2D depth-averaged current field within the tomography area [81]. The inverse problem can be expressed in matrix notation as:

$$y = Ex + e. \quad (5)$$

Here, the vector y indicates the travel time difference for the actual station pairs; matrix E is the transform matrix that rests with the FAT positions in the tomography area; x represents the unknown solution vectors for the Fourier expansion of the stream function; and e is the random error vector, corresponding to the observation errors.

To consider the riverbank condition in the inverse problem, a set of linear equations $0 = \mathbf{u}(x_b, y_b) \cdot \mathbf{m}(x_b, y_b)$ were established, where \mathbf{m} represents the unit vector perpendicular to the riverbank at each given position (x_b, y_b) . These linear equations were rewritten by the stream function; these equations were then added to the rows of Eq. 5. Here, the riverbank condition was provided for 22 points distributed over each riverbank (Figure 3.1c).

Equation 3 constructs an ill-posed issue, and the matrix E becomes singular. We can obtain a generalized inverse matrix by applying the singular value decomposition method; however, the solution is unstable when small singular values exist [79]. Hence, following the damped least-squares method [75], [79], we define the objective function J and introduce a damping factor α to stabilize the solution as:

$$J = (y - Ex)^T (y - Ex) + \alpha^2 x^T x. \quad (6)$$

By minimizing J , the expected solution \tilde{x} is expressed as:

$$\tilde{x} = (E^T E + \alpha^2 I)^{-1} E^T y. \quad (7)$$

The damping factor, α , is resolved to attain an optimum size of error and solution through the L-curve method. In order to decrease the periodicity effect in the solution, the adopted inversion area was twice larger than the tomography area [81]. For the damped least-squares method, the expected error covariance matrix U (uncertainty) of the solutions can be calculated and written with regards to Yamaguchi et al. (2005).

One of the main errors is the inadequacies of the inverse method in resolving vortex fields with lengths that are smaller than the spatial resolution [73]. In this work, the maximum wavenumbers in the Fourier expansion within the inverse domain were $\frac{2\pi N}{170 \times 2} m^{-1}$. The number of truncated Fourier series coefficients (N) was considered as 3 in this study, which indicates the minimum and maximum wavelength of one cycle per ~ 18 m and ~ 32 m, respectively. The river width was ~ 150 m at the junction; hence, $N = 3$ was satisfactory to resolve eddies formed at the junction.

The spatial resolution ΔR ($\Delta R = \sqrt{\frac{A}{N}}$) is determined by the number of acoustic transmission rays within the tomography area [81]. Here, A represents the tomography area (~ 52700 m²), and N is the number of successfully transmitted rays ($N \leq 14$). The highest spatial resolution of the inversion zone was ~ 7.8 m.

3.3. Results

3.3.1 Ray simulation results

Figure 3.3 exhibits the ray patterns with a salt wedge at high water and Figure 3.4 exhibits the results without a salt wedge at low water. Figures 3.3a and 3.4a demonstrate the typical vertical profiles of salinity, temperature, and sound speed documented by the CTD at the upstream Misasa Bridge (Figure 1a) on March 21, 2020. Figures 3.4 and 3.4 demonstrate the ray patterns attained between the shortest station pairs (S1-S2, ~ 85 m) and the longest station pairs (S3-S6, ~ 322 m), respectively. Owing to saltwater intrusion, deeper water had a higher salinity and temperature. At high water, owing to the weak mixing, the water column

was divided into two separate layers. In the upper layer, which is characterized by cold freshwater, the sound speed remained constant at 1448 m/s (Figure 3.3a). Then, it increased sharply to 1475 m/s at the interface between the freshwater and salt wedge, before remaining constant in the deeper layer (Figure 3.3a). As shown in Figure 3a, at low water, the salinity was small and the temperature and sound speed remained constant at 9.9 °C and 1446.2 m/s, respectively.

Figures 3.3 and 3.4 present the results (source angle, arrival time, ray length) of the ray simulation. The travel time of each ray path acquired by ray simulation are shown in Figures 3.3c–g and 3.4c–g. At both high water and low water, rays with large source angles created multiple bottom and surface reflections and often did not arrive at the receiver. Therefore, only the rays launched with small angles were successfully traced to simulate the sound traveling processes. For high water, the rays launched with a positive angle were linked to the first arrival peak with a few surface-bottom reflections (marked with red lines; Figures 3.3b–g); the opposite occurred at low water: the rays launched with a negative angle appeared to arrive earlier (Figures 3.4b–g). To further confirm the stratification effects on sound transmission, the source and receiver were shifted to the depth at the salt wedge. The results showed two typical patterns: (1) the rays were trapped in the upper layer and (2) the rays traversed the entire section (Figure 3.5). This was the effect of the salt wedge, whereby fresher and colder water generated slower sound speeds in the upper layer, while the saltwater and warmer water resulted in higher sound speeds in the deep layer.

Hence, mounting transducers inside the salt wedge may be a means of avoiding the reflection of sound by the saltwater boundary with distinct sound speed. In this work, the transducers were mounted at a height of ~0.2 mab. The arrival time for the observed data was determined by applying cross-correlation between the M-sequence used in the transmission and the received signal. Despite the abundance of ambient noise, the influences of the irregular topography and the conspicuous signal attenuation, the cross-correlation function presented multiple sharp peaks. Based on the results of the ray simulation, the first peak points were selected here, and then the calculated difference and the summation of travel time were used as the input data for the inverse analysis.

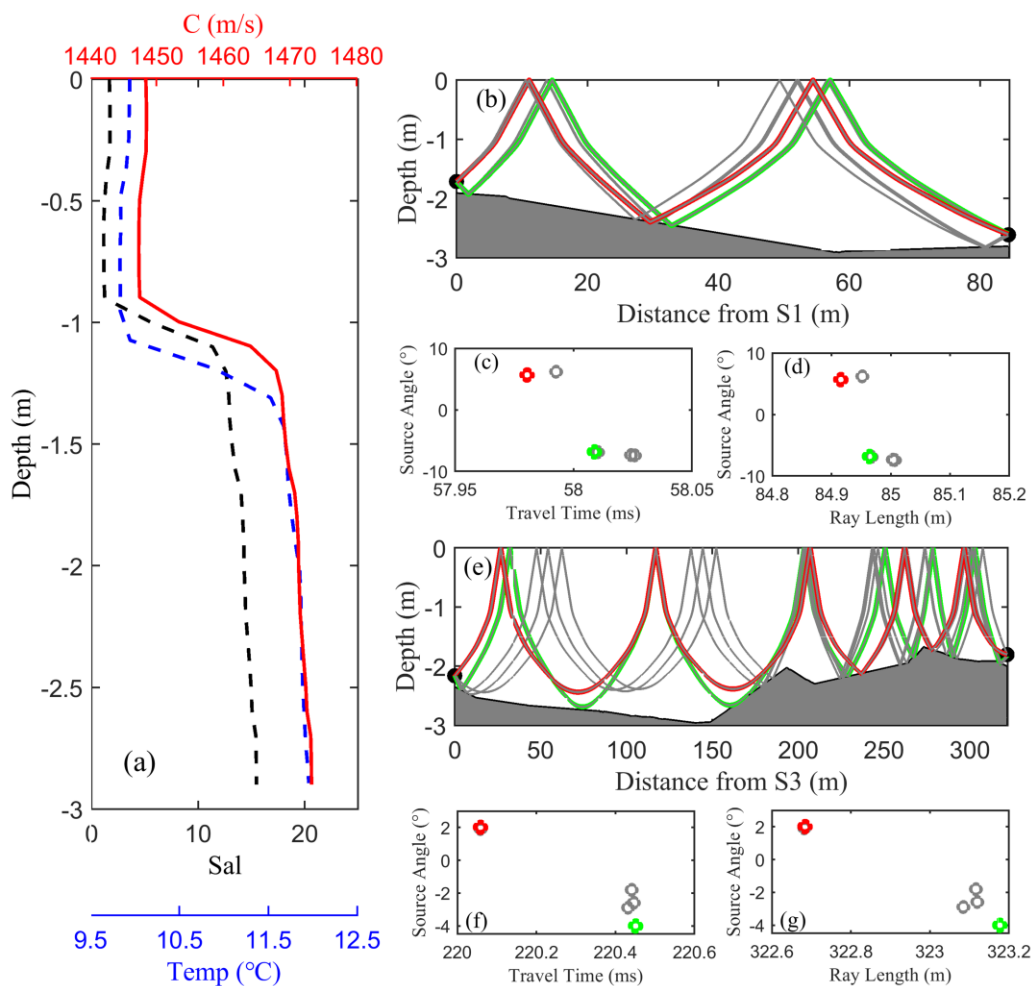


Figure 3.3 (a) Typical water temperature, salinity, and calculated sound speed profiles with a salt wedge at high water. (b)–(d) and (e)–(g) display the results (source angle, arrival time, and ray length) of ray tracing along the shortest and longest transmission lines, S1–S2 and S3–S6, respectively.

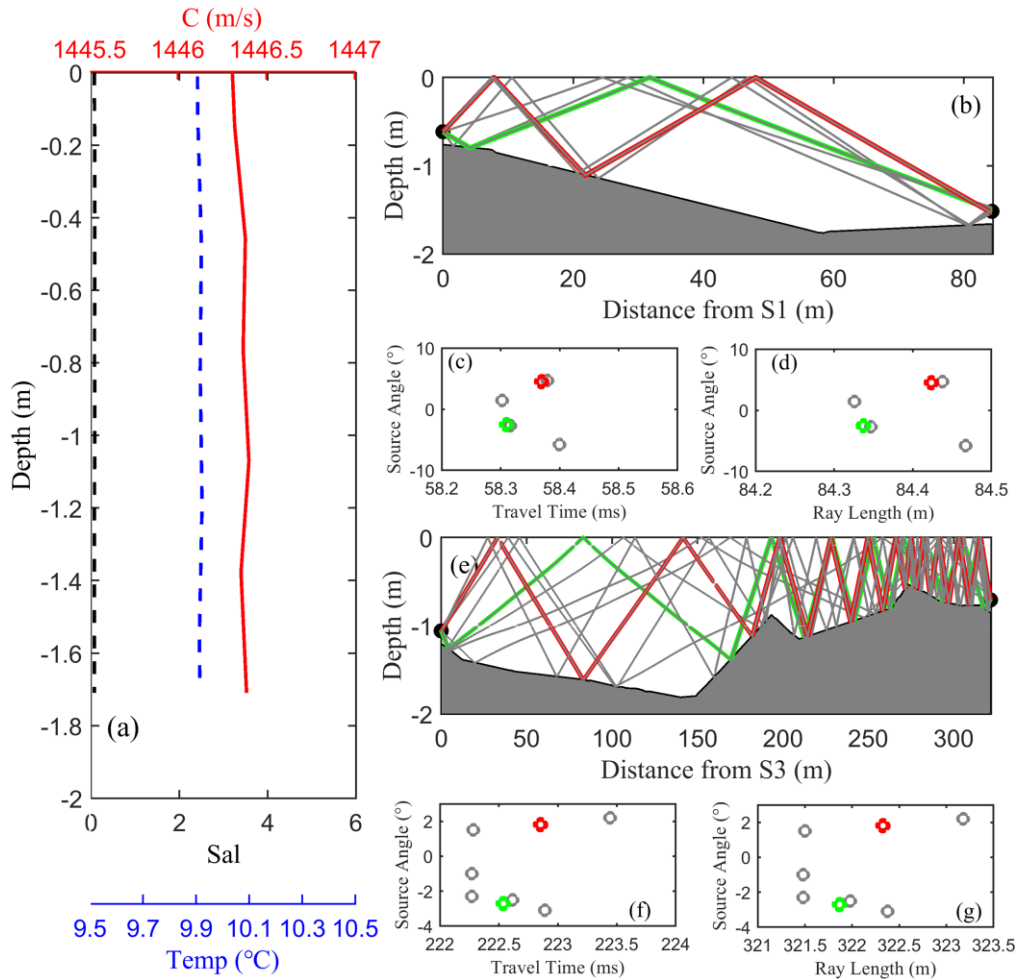


Figure 3.4 (a) Typical water temperature, salinity, and calculated sound speed profiles without a salt wedge at low water. (b)–(d) and (e)–(g) display the results (source angle, arrival time, ray length) of ray tracing along the shortest and longest transmission lines, S1–S2 and S3–S6, respectively.

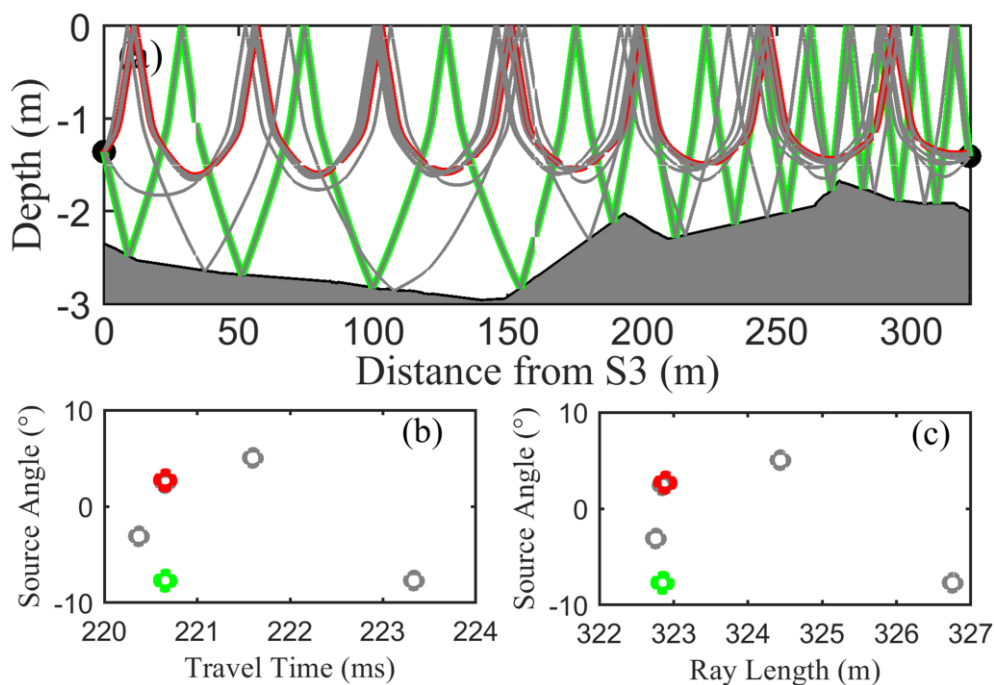


Figure 3.5 (a) Results of ray tracing when transducers are installed at the depth of the salt wedge for the longest station pairs (S3-S6), (b) source angle (deg) and arrival time (ms), (c) source angle (deg) and length of each ray (m). The sound speed profile is identical to that shown in Figure 3.3a.

3.3.2 Inverse results

3.3.2.1 2D currents and salinity distributions during spring tide

The behaviors of the depth-averaged currents and salinity during the spring tides (Figure 3.6) were reconstructed by applying the inverse approach. The flow distribution pattern responded well with the tide, and the inverted velocity directions and magnitudes exhibited higher similarities with those measured at S3-ADCP than those at S1 and S5-ADCPs. Because the tomography area is small, the spatial difference in salinity was not significant. However, the salinity distribution pattern also responded well with the tide; high salinity occurred at high water, whereas salinity was negligible at low water. From the appearance of salinity (Figure 3.6b) to it reaching the maximum (Figure 3.6c), and its seaward retreat and disappearance (Figure 3.6e), ~ 9 h were required to complete the salinity pattern.

During the flood tides, significant landward currents with a maximum

speed of ~ 0.4 m/s occurred (e.g., Figures 3.6b and 3.6f); during the ebb tides, significant seaward currents were observed with a maximum speed of ~ 0.55 m/s (e.g., Figures 3.6d and 3.6h). During the ebb tides, the currents tended to be slow and divided into two parts at the area around S5. At the beginning of the ebb tide, currents that flowed to the Tenma River were stronger than those that flowed to the downstream Kyu Ota River (e.g., Figure 3.6g), the domain of stronger currents which gradually change to the Kyu Ota River around the low water (e.g., Figure 3.6i). During the flood tides, the currents in the Kyu Ota River were stronger than those in the Tenma River (e.g., Figures 3.6b and 3.6f). A confluence of currents from both branches appeared near S5 during the flood tide (e.g., Figures 3.6b and 3.6f), and a separation of current occurred around S5 during the ebb tide (e.g., Figures 3.6a and 3.6d). Temporally, the current distribution at the tidal junction showed that the currents during the ebb tides were higher than those during the flood tides. Spatially, the behaviors of the velocity distribution at the tidal junction indicated that the currents in the Kyu Ota River were stronger than those in the Tenma River.

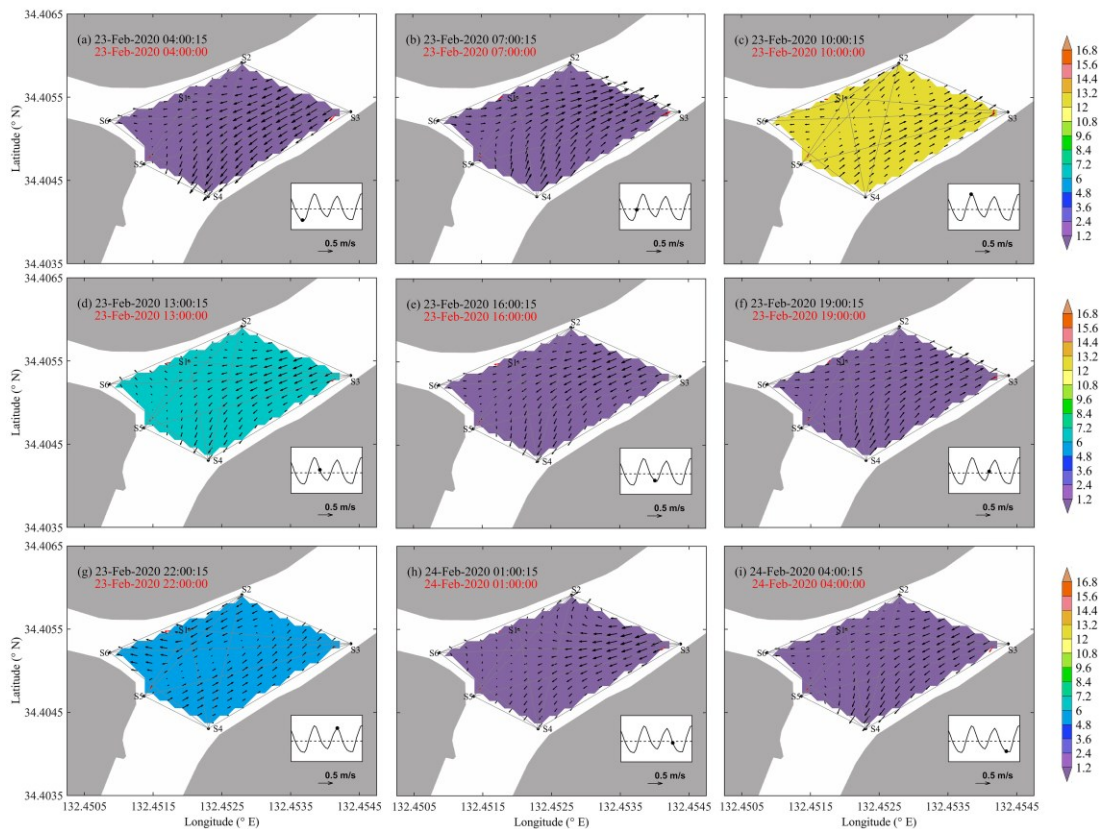


Figure 3.6 Depth-averaged currents and salinity distributions for two semi-

diurnal tide cycles during spring tide. The black and red arrows represent the velocities acquired by the fluvial acoustic tomography (FAT) system and the Acoustic Doppler Current Profiler (ADCP), respectively. The FAT stations are marked by black dots, and the actual acoustic transmission rays among the FAT stations are connected by solid lines. The tidal phase of each sub-figure is indicated by a black dot on the water level in the lower right corner.

3.3.2.2 2D currents and salinity distributions during neap tides

Figure 3.7 shows the behaviors of the depth-averaged currents and salinity during neap tides, where the process of salinity distribution differed from the reciprocating patterns observed during the spring tide. The salinity pattern began to develop landward from the low water and reached a mature phase around the high water. The difference was that the salinity did not disappear at low water (e.g., Figures 3.7e and 3.7f); instead, the salinity at the ebb slack remained high during the neap tide (Figure 3.7e). There was a small difference in salinity between the flood and ebb tide. Owing to the small change in the tidal range during the neap tide, the performances of the tidal current were not as obvious as during spring tide. During the flood tide, significant landward currents flowed from the downstream Kyu Ota River with a maximum speed of ~ 0.2 m/s (e.g., Figures 3.7b and 3.7f). A counter-clockwise circulation was revealed by inverted FAT results around low water during neap tide (e.g., Figures 3.7b–3.7e), the currents were divided into two parts, with one part flowing landward and the other part flowing into the western branch (S1–S2). During the ebb tides, significant seaward currents flowed from the Kyu Ota River to the Tenma River, with a maximum speed of ~ 0.45 m/s (e.g., Figures 3.7d and 3.7e). The currents continuously flowed landward and turned to the Tenma River from the downstream Kyu Ota River (S4–S5), and the behaviors of the currents varied slightly with the tide (Figure 3.7). The seaward flows appeared across the whole surveyed area at the lower water (Figure 3.7i).

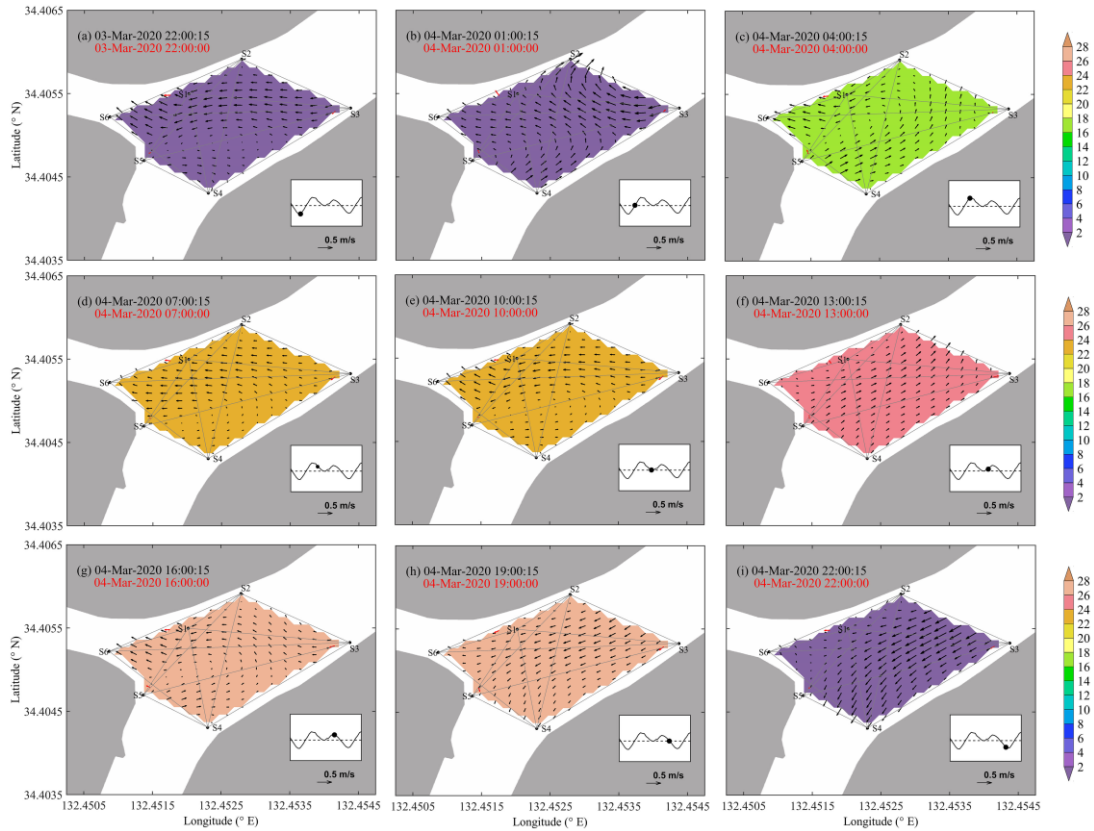


Figure 3.7 Depth-averaged currents and salinity distributions for two semi-diurnal tide cycles during a neap tide. Black and red arrows represent the velocities acquired by the fluvial acoustic tomography (FAT) system and Acoustic Doppler Current Profiler (ADCP), respectively. FAT stations are marked by black dots, and the actual acoustic transmission rays among the FAT stations are connected by solid lines. The tidal phase of each sub-figure is indicated by a black dot on the water level.

3.3.3 2D residual currents and tidal ellipse distributions

The inverse method calculates the depth-averaged velocity at each computational grid point. Thus, the inversed velocity results were directly applied to a point-by-point classical tidal harmonic analysis to acquire five tidal constituents (MS_f , O_1 , K_1 , M_2 , and M_4) and a temporal mean of the residual currents [82].

Figure 6 presents the temporal mean of the residual current, as well as the tidal ellipse spatial distributions of five tidal constituents. The residual currents flowed mainly seaward in the observation area, with a maximum value of 0.18 m/s, a minimum value of 0.01 m/s, and a mean residual current of 0.10 m/s (Figure 3.8f). The semi-diurnal tidal constituent M_2

(Figure 3.8c) dominated at the junction, the spatially averaged amplitudes of O_1 , K_1 , M_2 , M_4 , and MS_f follow the proportions of 1.00:1.13:4.52:0.61:1.28. The major axis directions of the tidal ellipses for the five constituents were generally northeast–southwest in the Kyu Ota River. The M_2 constituent was predominant in the Kyu Ota River (Figure 3.8c). The semi-major axes of the M_2 tidal ellipses were extended in a northeast–southwest direction in the Kyu Ota River, and the ellipses were in a slightly west–east direction in the Tenma River. The mean values of the semi-major and semi-minor axes of M_2 tidal currents were 0.15 and 0.01 m/s, respectively. The M_4 constituent was larger in the Kyu Ota River area, and the averaged semi-major and semi-minor axes of the M_4 were 0.05 and 0.007 m/s, respectively. The M_4 semi-major axis direction was slightly north–south in the west part of the observation region and became northeast–southwest in the lower right area (around S4) (Figure 3.8d).

Distributions of tidal ellipses for M_2 and M_4 tidal constituents and the residual currents during spring and neap tide corresponding to the current distributions of Figures 4 and 5 are shown in Figure 3.9. The residual currents flowed mainly seaward during spring and neap tides (Figures 3.9a and 3.9d), with maximum values of 0.22 m/s (Figure 3.9a) and 0.21 m/s (Figure 3.9d), minimum values of 0.003 m/s (Figure 3.9a) and 0.004 m/s (Figure 3.9d), and mean residual currents of 0.11 m/s (Figure 3.9a) and 0.10 m/s (Figure 3.9d), respectively. The mean residual currents, which most represent the river discharge, led to a ~22% increment and decrement of ebb and flood velocities at a reference velocity of 0.5 m/s, respectively.

The M_2 constituent was predominant in the Kyu Ota River (Figure 3.9b). The semi-major axes of the M_2 and M_4 tidal ellipses were extended in a northeast–southwest direction in the Kyu Ota River, and the ellipses were in a slightly west–east direction in the Tenma River. Different from the spring tide, during neap tide, the M_2 constituent was larger at the junction (Figure 3.9e), and the M_4 was weaker than that during spring tide (Figure 3.9f). The M_2 semi-major axis direction was northeast–southwest in the lower right area (around S4) and became slightly west–east in the left part of the observation region (Figure 3.9e).

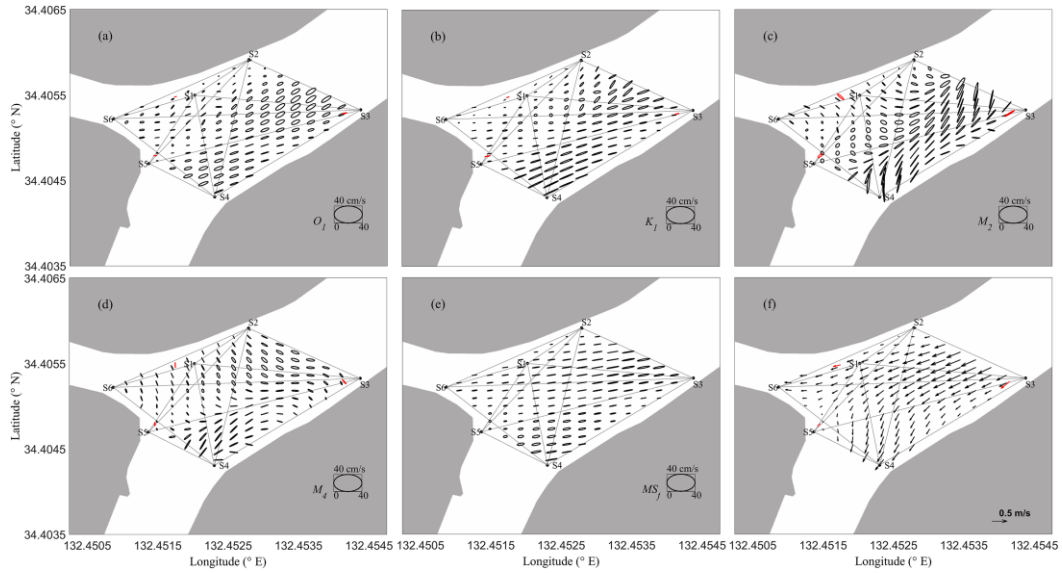


Figure 3.8 Distribution of tidal ellipses for five tidal constituents obtained by harmonic analysis during the whole observation period, (a) O_1 , (b) K_1 , (c) M_2 , (d) M_4 , (e) MS_7 ; and (f) the residual currents. The black arrows and ellipses are from FAT results, and the red arrow and ellipse indicate the Acoustic Doppler Current Profiler (ADCP) results.

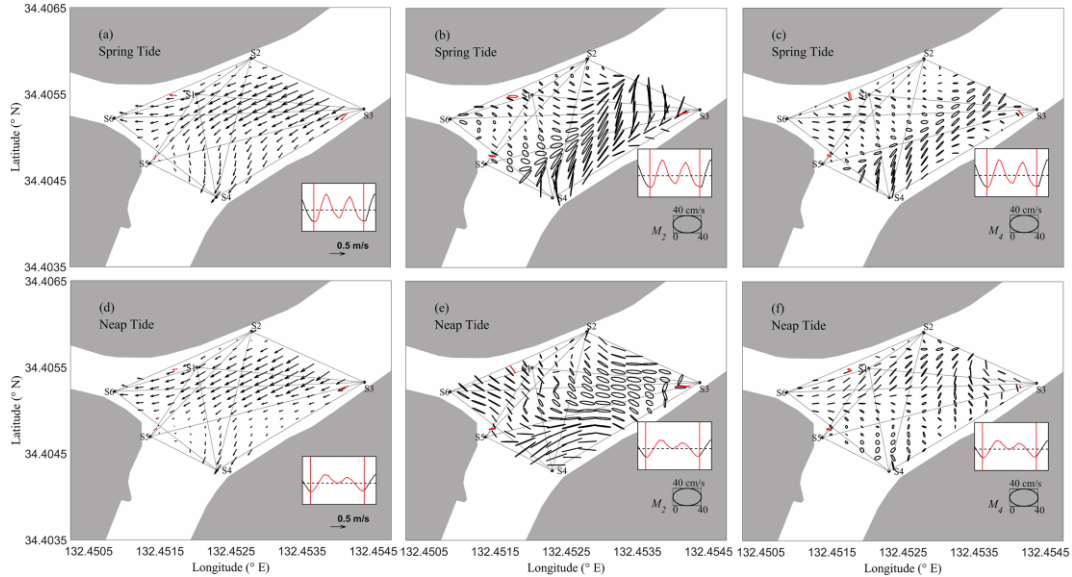


Figure 3.9 Distributions of tidal ellipses for M_2 and M_4 tidal constituents, and the residual currents during spring (a–c) and neap (d–f) tides corresponding to the current distributions shown in Figures 4 and 5. The black arrows and ellipses are from FAT results, and the red arrow and ellipse indicate the Acoustic Doppler Current Profiler (ADCP) results.

3.4. Discussion

3.4.1 Comparisons of FAT vs. ADCP and FAT vs. CT/CTD results

Further, to verify the performance of the tomographic results, we compared the inverse estimates with data for the three fixed ADCPs. As shown in Figures 3.11, 3.12, and 3.13, there were some differences between the magnitudes and directions of the velocities reconstructed by FAT and the ADCP velocities because the locations of the ADCPs were inappropriate as they were located near the boundary of the tomography area. The skill score (SS) [83], RMSD and MRE were used to evaluate the inverse results against the ADCP. The SSs at S1, S3, and S5-ADCP were from 0.52 to 0.73 and from 0.53 to 0.71 for the eastward and northward components, respectively. The MREs of both components at S1, S3, and S5-ADCP were from 10.5 to 12.9% and from 14.2 to 28.4 %, respectively. The RMSD of both components at S1, S3, and S5-ADCP were from 0.09 to 0.13 m/s and from 0.07 to 0.14 m/s, respectively. The large differences related to S3-ADCP and S5-ADCP showed an underestimation of the eastward and northward components, respectively. Overall, the behaviors of S3-ADCP were better in terms of velocity directions and values than those at S1-ADCP and S5-ADCP.

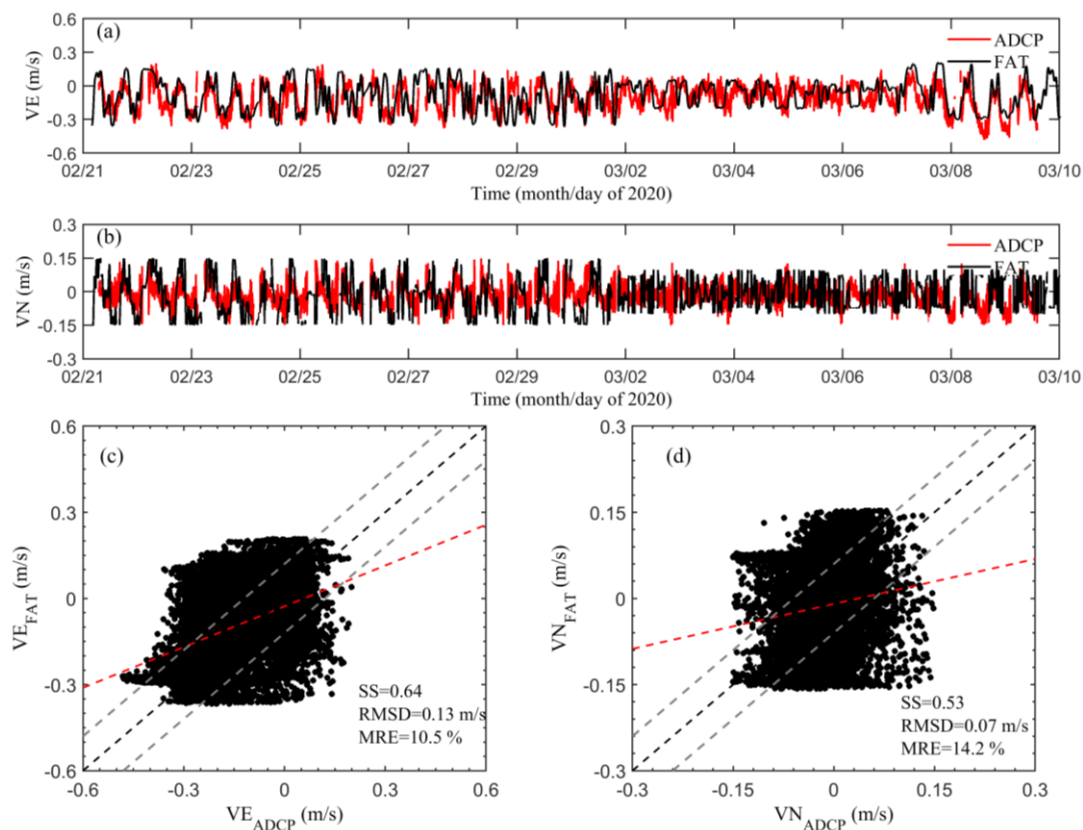


Figure 3.10 Relationships between fluvial acoustic tomography (FAT) system and station 1 Acoustic Doppler Current Profiler (S1-ADCP): (a) and (c) eastward; (b) and (d) northward velocity components. The red, black, and grey dashed lines denote the fitting line, the 1:1 line, and the 20% relative error line, respectively. The skill score (SS), the root mean squares difference (RMSD), and the mean relative error (MRE) are given at each panel.

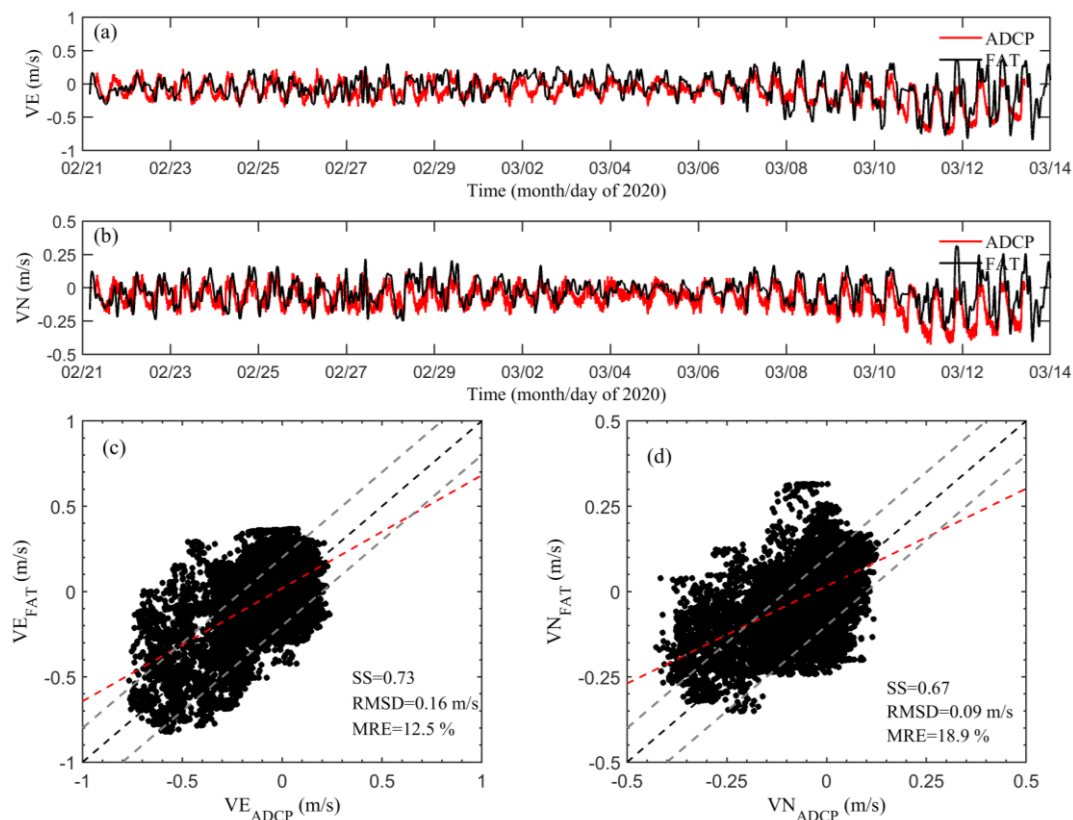


Figure 3.11 Relationships between fluvial acoustic tomography (FAT) system and station 3 Acoustic Doppler Current Profiler (S3-ADCP): (a) and (c) eastward; (b) and (d) northward velocity components. Red, black, and grey dashed lines denote the fitting line, the 1:1 line, and the 20% relative error line, respectively. The skill score (SS), the root mean squares difference (RMSD), and the mean relative error (MRE) are provided in each panel.

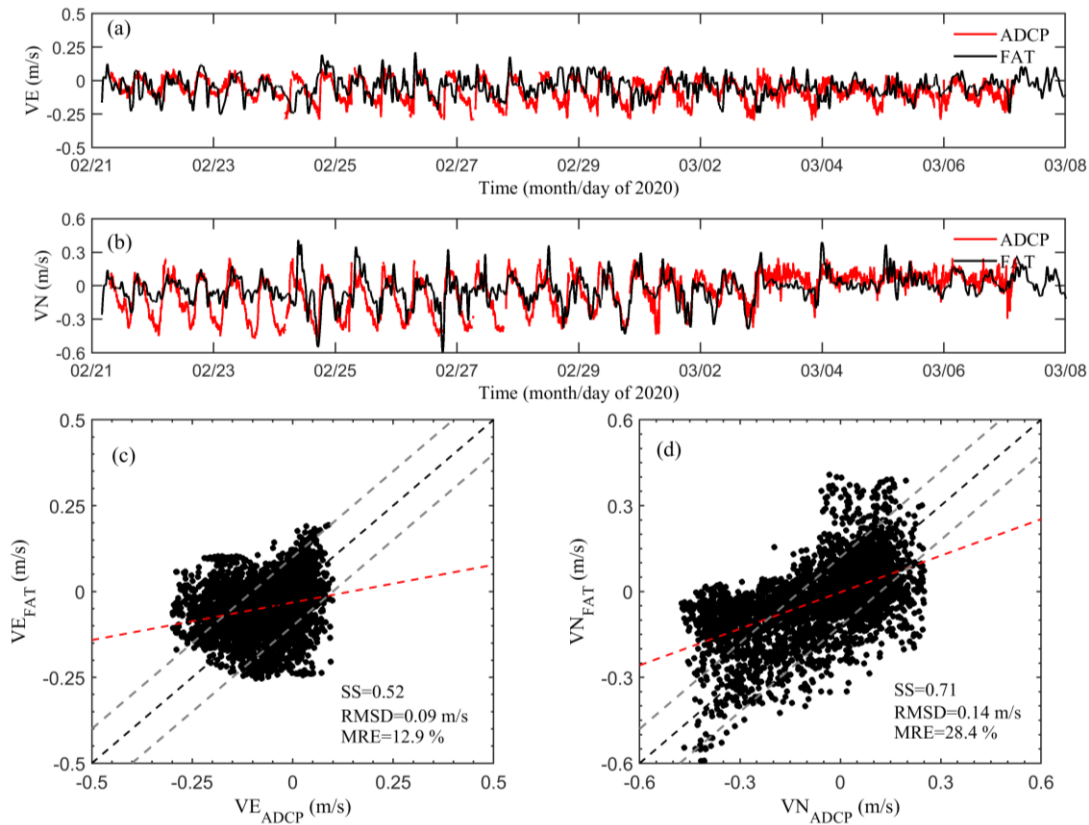


Figure 3.12 Relationships between fluvial acoustic tomography (FAT) system and station 5 Acoustic Doppler Current Profiler (S5-ADCP): (a) and (c) eastward; (b) and (d) northward velocity components. Red, black, and grey dashed lines denote the fitting line, the 1:1 line, and the 20% relative error line, respectively. The skill score (SS), the root mean squares difference (RMSD), and the mean relative error (MRE) are provided in each panel.

There are likely several reasons for the larger inconsistency of the velocity components between the inverse results and ADCP: 1) the fundamental and essential differences between ADCP and FAT, whereby the ADCP monitors the velocity profile at the fixed station, while the FAT results are the spatially and depth-averaged values; 2) the ADCP monitors much smaller spatial scales of velocities, while the highest spatial resolution of the inverse analysis was ~ 7.8 m in this study; 3) the enforced riverbank settings that constrain variations of the velocity direction with regard to the riverbank geometry; as three ADCPs were placed at the boundary of the tomography area, there may be some differences between FAT and ADCP; and 4) the solution of the inverse problem is sensitive to

the number of the transmission lines. The sound transmission data for S1–S6 and S2–S6 were missing a considerable amount, which resulted in the poor performance of S1-ADCP.

Current structure measurements by FAT and CAT with multi-stations were performed in pioneer works [73], [75]–[80]; some differences were noted when compared with the ADCP results [78]. The relative difference between the two techniques was within 20% for the velocity components [73]. In this work, more than 70% of the velocity component values at each station fell within 20% of the velocity components. However, as the most common method used to map the 2D currents, the accuracy of the inverse method in this work still needs to be improved. A coast-fitting method which considers the shoreline condition was introduced to improve the current inversion by CAT [84]. In future research, this method may need to be applied to improve the results of FAT; however, the applicability and accuracy of this method in this tidal junction must be verified first.

Moreover, Figure 3.13 compares the depth-averaged velocity directions obtained from StreamPro ADCP measurements against those derived from FAT. Despite the fundamental and essential differences between these techniques, the behaviors of tidal velocity shown in Figure 8 indicate that there was a good agreement between these two different techniques at the tidal junction, and the RMSD of eastward and northward velocity components varied from 0.06 to 0.12 m/s and 0.04 to 0.11 m/s, respectively.

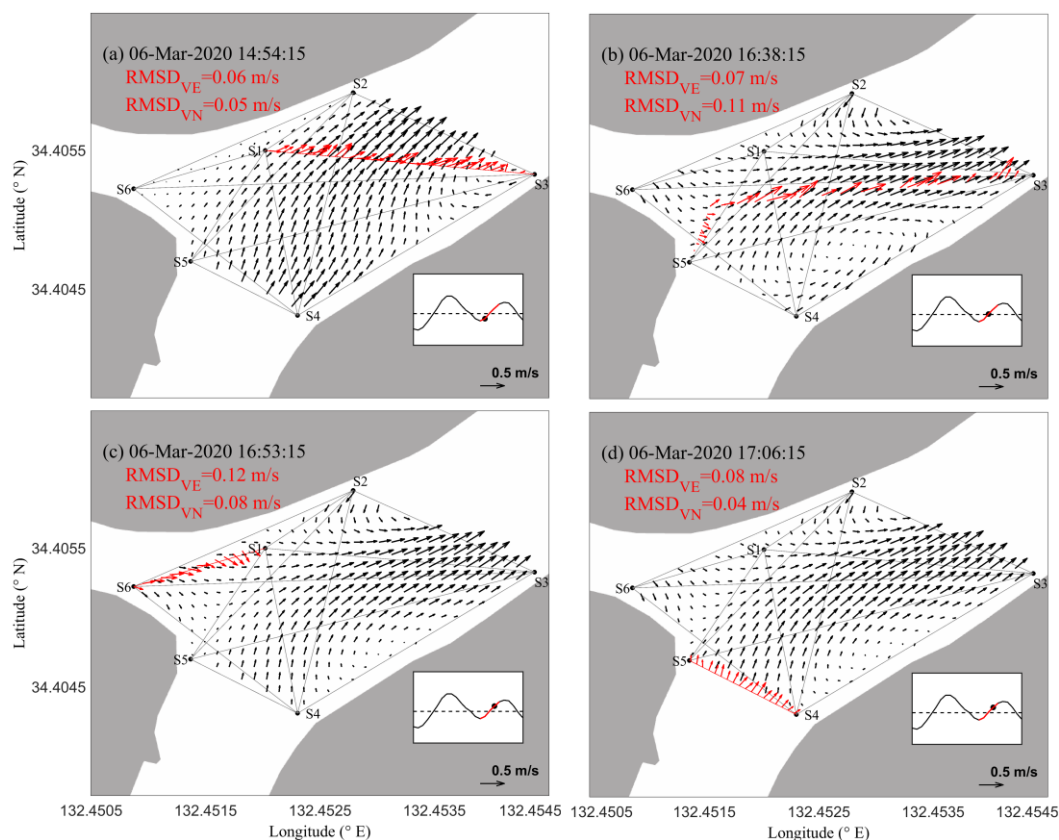


Figure 3.13 Typical depth-averaged currents from fluvial acoustic tomography (FAT) system during the StreamPro Acoustic Doppler Current Profiler (ADCP) observation period. The black and red arrows represent the velocities acquired by FAT and StreamPro ADCP, respectively. Red solid lines connecting the acoustic stations represent the StreamPro ADCP observation routes. The tidal phase of each sub-figure is indicated by a black dot on the water level. The root mean squares difference (RMSD) of the eastward and northward velocity components are given in each panel.

The temporal-spatial distributions of the tidal currents appeared realistic, considering the shape of the surveyed area (Figure 3.1b). The flow directions in the study area can be explained by the geometry of the junction, which leads to a large curvature in the current directions when they flow into the physical domain. Generally, streamlines within the tomography area obeyed the curvature of the riverbanks (Figures 3.6 and 3.7).

3.4.2 Evaluation of the inverse results

The range averaged currents along the 14 sound transmission lines

between inverted and observed FAT data are compared in Figure 3.14. The SS, RMSD, and MRE between inverted and observed FAT data ranged from 0.38 to 0.93, 0.08 to 0.22 m/s, and 1.2% to 37.5%, respectively. The results for the station pairs S1–S3, S1–S4, S1–S5, S2–S3, S2–S4, S3–S4, S3–S5, and S3–S6 show the best agreements between both results, while the inverted results underestimate the peak heights of the observed results. The spatial interpolation adopted in the inverse analysis may have caused the underestimation. The results for the station pairs S1–S2, S1–S6, S2–S5, and S2–S6 agree relatively well, while the results of S4–S5 and S4–S6 agree the least.

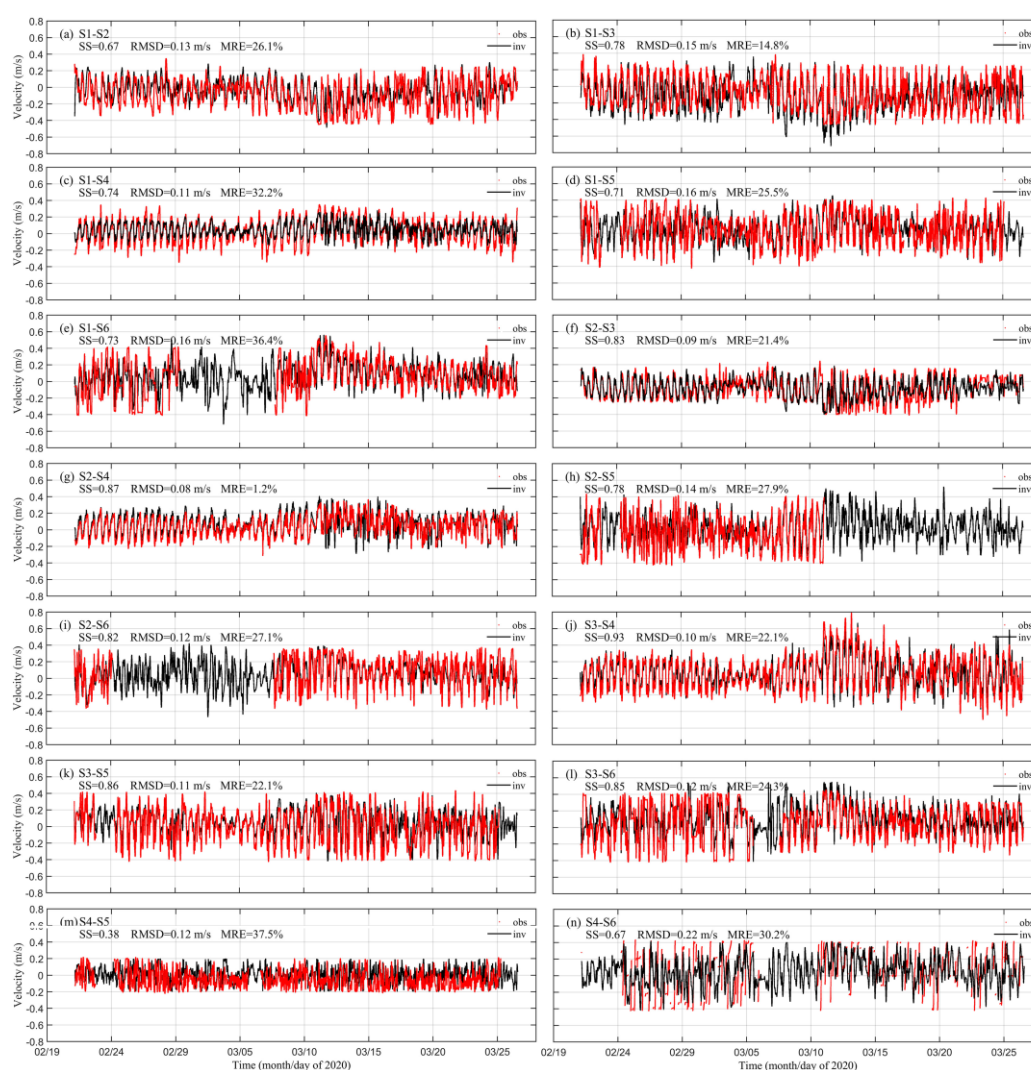


Figure 3.14 Time plots of the inverted (black lines) and observed (red dots) range averaged currents calculated along each transmission line. The skill score (SS), root mean squares difference (RMSD), and mean relative error (MRE) are provided in each panel.

Figure 3.15 shows the uncertainty maps of the inverse solutions of velocities corresponding to the currents in Figure 3.6. In most of the inverse area, the uncertainties were less than 0.1 m/s in the tomography domain (Figure 3.15). For a reference velocity of 0.5 m/s at the tidal junction, the uncertainties of velocity were $\sim 20\%$. A higher uncertainty occurred at the periphery, especially around S3 and S5 (e.g., Figures 3.15a and 3.15c). Although the successful acquisition rates of the 14 sound transmission rays varied widely (19–92%, Figure 3.2), the related data in Section 3.3.2 show satisfactory results for the currents. Overall, this study scheme performed well (considering the observation period and precision) adjacent to the tidal junction.

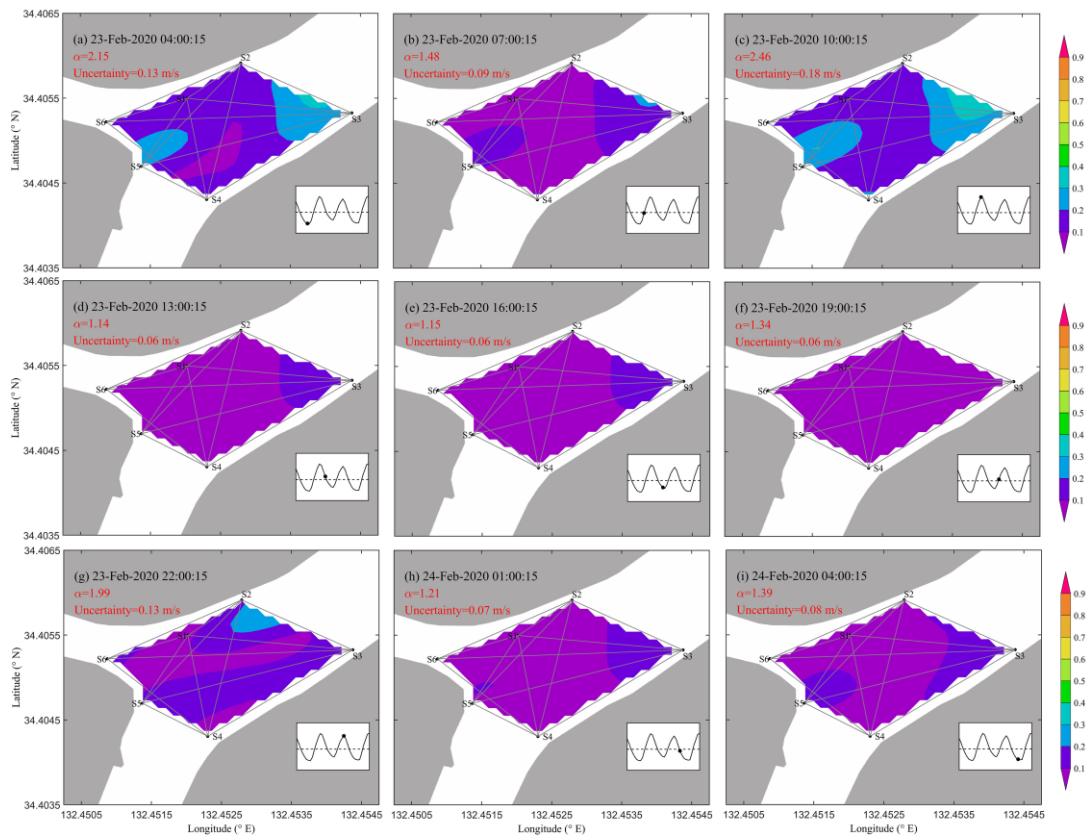


Figure 3.15 Uncertainty maps of inverse solutions during spring tide corresponding to the current distributions of Figure 3.6. The values of the damping factor α and the spatially averaged uncertainty of each figure are provided in the upper left corners of the respective figures.

3.4.3 River-tide interactions at the junction

In estuaries, due to the interactions of tidal harmonics and river flow, the tidal response is generally described by the progress of tidal distortion and asymmetry. Friedrichs and Aubrey (1988) proposed a mathematical relationship between M_2 and M_4 , which is utilized as the indicator of tidal distortion and asymmetry.

The tidal discharges (black line, Figure 3.16a) were calculated by two crossing transmission lines, S2–S4 and S3–S6, following the formula described in Kawanisi et al. (2013). Red lines indicate low pass filtered data of the tidal discharge (black line) with a cut-off period of 24.4 h (Figure 3.16a). Figure 13c reveals the higher M_2 amplitudes and phases during spring tides; although the fitting lines of M_4 amplitudes and phases show increasing and decreasing patterns, respectively (Figure 3.16d), the values of both did not change considerably. This revealed that the tidal range did not significantly impact the M_4 during our observation period. Like the relationships of tidal range, compared with M_4 , M_2 shows a more significant change under the effect of discharge. This revealed that the rate of increase of M_2 was higher than M_4 (Figures 3.16c–3.16f), whereas a slow increase slope of M_4/M_2 is shown in Figure 13g. This reflects the increased tidal wave deformation that occurred at the tidal junction with gradually increasing tidal range and discharge.

River flow can modify the interactions between tidal constituents and the subsequent generation of over-tides and compound tides [4]. River flow also plays a crucial role in river flow-enhanced subtidal friction, which significantly diminishes the tidal energy upstream while triggering tidal energy transfer from the primary tides to downstream over-tides [86]. According to the two parameters (M_4/M_2 , $2M_2-M_4$) shown in Figures 3.16g and 3.16h, a distorted and ebb-dominant system existed at the tidal junction, suggesting a higher ebb velocity. This demonstrated the role of river flow on the tidal asymmetry at the junction. There are likely several reasons for this phenomenon: 1) under normal conditions, the river discharge was limited; therefore, the river discharge cannot create the significant effects at the junction, and the junction is still under the tidal control; 2) the tidal channel junction is in the middle of the Ota River network, which is located ~5.8 km from the river mouth, implying that the tide needs to travel more

in the landward direction to generate over-tides.

Additionally, river-tidal interactions can significantly disturb the characteristics of tidal asymmetry. Some studies observed a landward increase of M_4/M_2 with a damping of the M_2 tide and noted a significant decline in M_4/M_2 from spring to neap tides [4], [87]. In this work, we also observed relatively larger M_4/M_2 values during spring tides (Figure 3.16g). The increase in the slope of M_4 was lower than that of M_2 with the gradually increasing discharge (Figures 3.16e–3.16f). This again supports the abovementioned argument: despite the role of rivers, tides still dominate at this junction. The significant tidal damping process may occur upstream of this tidal junction, especially during spring tide (Figures 3.9b–3.9c). The semi-major axes of the M_2 and M_4 tidal ellipses were similar and extended in a northeast–southwest direction in the Kyu Ota River.

The nonlinear tide M_4 and its related tidal asymmetry are one of the most important mechanisms causing residual suspended sediment transport in estuarine environments [16]. For this study, at the tidal junction of the Ota River, river flow is normally limited, such that the influences resulting from tide-induced asymmetric currents are noteworthy for suspended sediment transport [12]. This differs from the situation in the Yangtze River estuary because of the strong discharge (6000–92000 m³/s). Further, the enhanced ebb-directed sediment transport by the river flow is significant, while the role of tide-induced asymmetric currents is negligible in suspended sediment transport mechanisms [5]. The river-tidal interactions and the resultant tidal asymmetry require attention at the junction. The Ota River networks may cause some variations in water levels and bed frictions, which have continuous effects on sediment erosion, deposition, and transport processes; this theory requires support from further research.

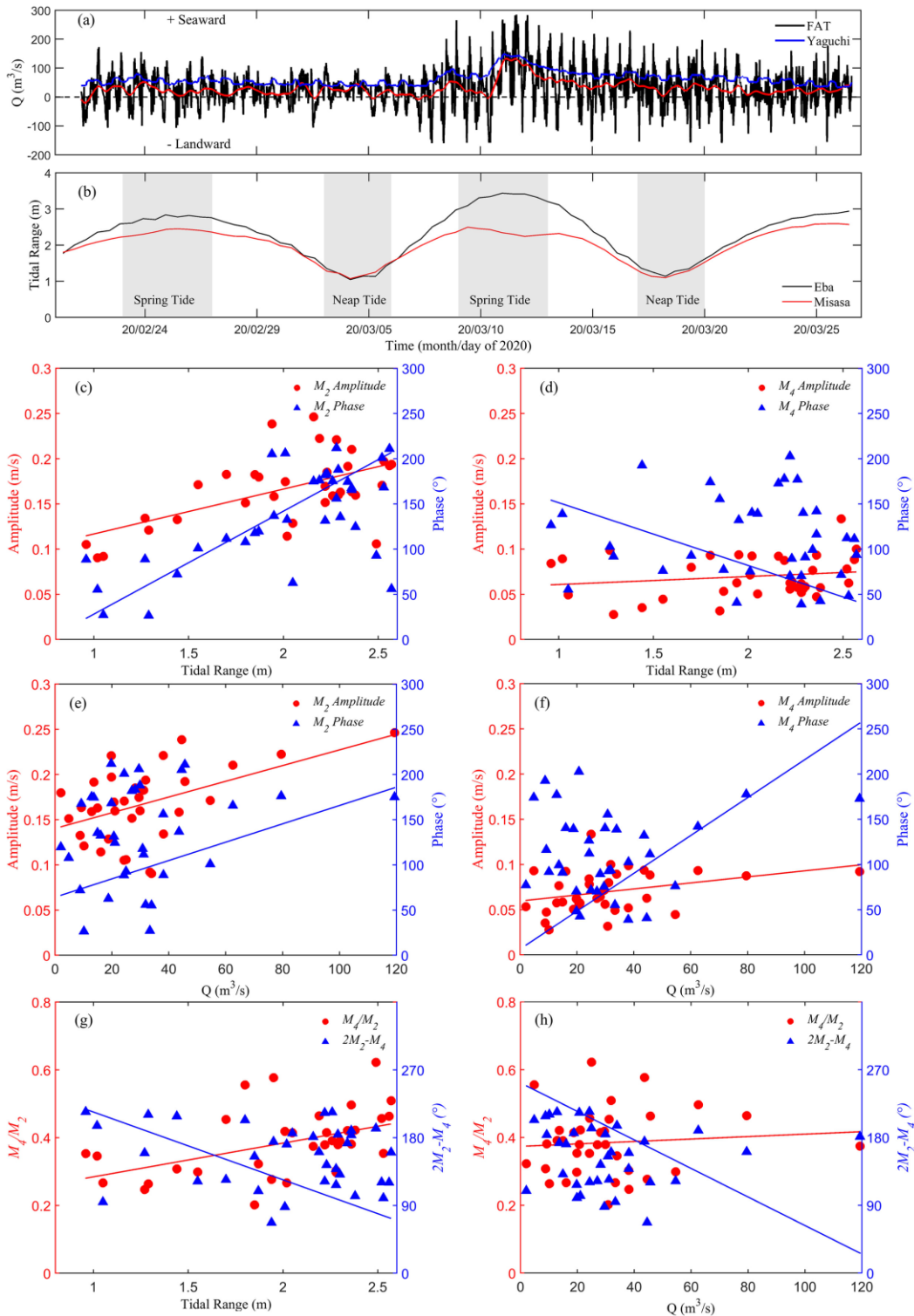


Figure 3.16 (a) Discharge at Yaguchi gauging station (blue line) and tidal discharge in the Kyo Ota River (black line), which was calculated from the two crossing transmission lines S2–S4 and S3–S6. Red lines indicate low-pass filtered data of the tidal discharge (black line) with a cut-off period of 24.4 h; (b) tidal ranges at two water level gauging stations (Eba and Misasa); (c) relationship between the daily spatially averaged amplitude and phase

of M_2 , and the daily tidal range; (d) relationship between the daily spatially averaged amplitude and phase of M_4 , and the daily tidal range; (e) relationship between the daily spatially averaged amplitude and phase of M_2 , and the daily tidal discharge; (f) relationship between the daily spatially averaged amplitude and phase of M_4 , and the daily tidal discharge; (g) relationship between the daily spatially averaged amplitude ratio of M_4/M_2 and the phase of $2M_2-M_4$, and the daily tidal range; and (h) relationship between the daily spatially averaged amplitude ratio of the M_4/M_2 and the phase of $2M_2-M_4$, and the daily tidal discharge.

3.4.4 2D current dynamics at the junction

The freshwater discharge at Yaguchi gauging station only varied by $\sim 20\text{--}60\text{ m}^3/\text{s}$ (Figure 3.16a) during low-flow periods. A previous study revealed that $\sim 10\text{--}20\%$ of the discharge was diverted into the Otagawa floodway [9]; the runoff flow into Kyu Ota River from the Oshiba gates contributed $\sim 20\text{--}90\%$ of the Yaguchi discharge during our observation period (red/blue lines, Figure 3.16a). The freshwater discharge at the junction was $\sim 29.2\%$ of the tidal discharge during the observation period (mean (red line/black line), Figure 13a). During the ebb tides, $\sim 29.2\%$ of freshwater discharge was added to the seaward currents; therefore, the ebb tides had larger velocities than the flood tides. Meanwhile, during the flood tides, a $\sim 29.2\%$ decrease resulting from the freshwater discharge would affect the flood velocities. The results in Section 3.3 demonstrate that the mean residual currents would lead to a $\sim 22\%$ increase and decrease of ebb and flood velocities, respectively, indicating the role of river discharge at the junction. The values of $\sim 22\%$ and $\sim 29.2\%$ did not differ much from the reference velocity 0.5 m/s .

The water discharge division is mainly controlled by the size of the bifurcation branches and downstream boundary conditions [88]. An asymmetric water division is usually associated with an asymmetric planform [88]. The topography at the junction (Figure 3.1b) shows that the mean bed level in the western part was shallower than that in the eastern part of the junction, and that the western part was narrower than the eastern part, demonstrating that the junction is an asymmetric planform. The geometry of the junction (width-to-depth ratio) mainly controlled the division of water [29], [88]; the widths at the entrance transects of the

western and eastern branches were ~ 70 m and ~ 112 m, respectively. Due to the shallow depth at the junction, the width-to-depth ratio at the western branch was smaller than that at the eastern branch; hence, the discharge tended to flow more toward the eastern branch. Hence, higher ebb currents occurred in the eastern branch than in the western branch.

During neap tides, the tidal range markedly decreased to ~ 1 m (Figure 13b); the flows at the junction were under the combination of weak tides and low river discharge. The salinity pattern behavior at the junction showed that the mean salinity during neap tides was higher than that during spring tides (Figures 3.6 and 3.7), indicating the existence of the density-driven current phenomenon. The tidal ranges at Eba and Misasa during neap tides were comparable (Figure 3.16b). This indicates that there were minimal changes in the tidal damping and that the role of river discharge was weak from the mouth to the junction. The significant tidal damping process may occur upstream of the tidal junction. Hence, the currents generated by the river runoff and the seaward pressure-driven currents were limited at the junction. The landward density-driven currents that led to the landward flow were more important and the density-driven component

$-\frac{g}{\rho_0} \int_z^\zeta \frac{\partial \rho}{\partial x} dz$ increased with depth. The mean water levels recorded at

three ADCPs during the neap tide were ~ 1.3 m, ~ 1.7 m, and ~ 2.0 m at S1, S3, and S5 ADCPs, respectively. The density gradient was higher at the downstream (S5) stations than that at the side (S1–S2, S3–S4) and upstream (S2–S3) stations. When we narrowed the range of salinity distributions in Figure 5 (figures not shown), it was evident that the salinity decreased from line S2–S5 to the sides, and the density gradient mainly resulted from the salinity gradient. Hence, higher density currents lead to continuous landward flow from the downstream Kyu Ota River (S4–S5) (e.g., Figures 3.7c and 3.7e). The density gradient perpendicular to the channel exhibited higher variations than that along the channel (figures not shown). Burchard et al. (2011) determined that tidal flow in a channel is subject to a constant longitudinal density gradient, and lateral advective straining and longitudinal gravitational circulation contribute to estuarine circulation. In addition, tidal mixing, which results from tidal straining [89], can significantly alter estuarine circulation, and the tidal currents interacting with the freshwater-induced longitudinal density gradient could

greatly affect tidal mixing. Therefore, we can infer that the lateral advective straining and longitudinal gravitational circulation contributed to the flow pattern of the counter-clockwise circulation at the junction. Ultimately, the currents showed two parts (e.g., Figures 3.7c and 3.7e): one that directly flowed into the Tenma River (longitudinal gravitational circulation dominant) and another that flowed upward from S4–S5 (density currents dominant). These currents experienced tidal mixing at the intersection zone of lines S1–S4 and S3–S5 (lateral advective straining being dominant), and then flowed into the western branch.

3.5. Conclusions

For the first time, continuous 2D current and salinity fields were measured at a shallow junction using FAT systems composed of six stations from February 21 to March 26, 2020. In total, actual reciprocal sound transmissions were performed for ~34.4 days along 14 transmission lines. The horizontal structures and the spatiotemporal variation of the velocities and salinity distributions were well revealed by FAT. Although some differences were noted, in general, the horizontal velocities estimated by the inverse analysis were very similar to the S3-ADCP and the moving-boat ADCP velocities. The patterns of the salinity reconstructed by FAT were very similar to the CT/CTD results.

During spring tides, temporally, the currents during ebb tides were higher than those during flood tides. Spatially, the currents in the Kyu Ota River were stronger than those in the Tenma River. In the area near S5, the current velocity reduced, and they separated into two directions. During the neap tides, the performances of the currents were not as obvious as those during spring tides. A counter-clockwise circulation generated around the low water during neap tide was noted, based on the inverted results. The current patterns were divided into two parts: one part of the river water directly flowed into the Tenma River and another part of the currents flowed upward from S4–S5. Behaviors of the currents during the neap tide at the junction were likely the result of the density-driven current phenomenon.

Furthermore, uncertainty maps were constructed to appraise the influence of the acoustical ray number and bathymetry on the inverse results. Overall, this work showed a good performance of the employed

methods at the tidal junction. Finally, the inversed velocities were applied to the classical tidal harmonic analysis and the effects of river-tidal interactions on tidal asymmetry at the junction were discussed. A distorted and ebb-dominant system existed at this tidal junction. The increasing tidal wave deformation that occurred with the gradually increasing tidal range and the role of the limited river flow on the tidal asymmetry at this tidal junction were revealed.

This study demonstrated that the application of FAT in conjunction with the inverse method presents an effective tool to map 2D current and salinity fields. Furthermore, the results herein can form the basis for conducting a more detailed investigation of river-tidal interactions in a shallow tidal junction.

Chapter 4: Mapping salinity distribution at a shallow tidal channel junction using the fluvial acoustic tomography system

4.1. Introduction

In the estuary, the residual water currents were significantly influenced by the spatial and temporal distribution of salinity, mainly resulted from the gravitational and tidal straining circulation induced by salinity difference [34], [62]. This circulation furtherly influences the tidal and residual transport of sediment, and other aquatic materials in the tidal environments. Hence, a deep understanding of salinity dynamics is crucial to simulating, forecasting, and controlling salt intrusion in estuarine environments, such as, to maintain sufficient freshwater import in deltas.

Tidal junctions act as one of the most important characters in the tidal channel network, which are generally located in the middle area of a delta and directly related to the estuaries. Tidal junctions are regions in which exchange between river flow and saltwater intrusion. In many tidal junctions, export of salinity by the freshwater discharge and import by the gravitational current control the mechanisms of the salt balance, and can take the form of the salt wedge along the tidal channel [90]. Partially mixed or stratified water environments are usually characterized by frontal zones, dividing the less-dense freshwater from the more-denser seawater [91], [92]. Thus, understanding the exchange mechanisms of salinity in the tidal junction system is therefore of great scientific value.

In a tidal junction, the residual circulation, tidal currents and mixing asymmetry, as well as freshwater discharge from upstream dominated the physical processes. Hence, the salinity structure is balanced by the competing influences of river discharge, which tends to drive saltwater seaward; the gravitational circulation, which tends to drive saltwater landward; and a down-gradient salt flux due to shear dispersion, tidal pumping, and other processes [93]. To classify the driving mechanisms of the salt flux in the estuarine environments, many researchers decomposed the current and salinity fields (spatially and temporally) using both short-

term and long-term time series data [91], [92]. However, most of these previous works were mainly rely on the model results [35], [90], [92], [94]–[96], some works were depending on the point and transect observation results from traditional observation methods [36], [97], such as acoustic Doppler current profiler (ADCP), CT sensor, Compact CTD. Fluvial acoustic tomography (FAT) system is a powerful technology that can be utilized to estimate current structure and sound speed (related to temperature and salinity) in the shallow mountain river [40] and estuary [9], [73]. Zhang et al. (2015) used coastal acoustic tomography (CAT) to observe the upwelling caused by typhoons at Hiroshima bay, and successfully obtained results consisting of temperature field and tidal currents of the observed area. Huang et al. (2019) used CAT to observe the artificial upwelling in an anechoic tank. To our knowledge, none of the experimental observation targets relate to salinity inversion in a small and shallow tidal junction by FAT. Moreover, continuous and long-term measurements of salinity and currents are less commonly available than water level records.

Tide-induced variability in the density field and turbulent mixing requires that the estuarine characteristics must be understood, for instance, the tidal cycle average of the time-dependent characters and their interaction along the tidal channel. In this study, six FAT systems were operated to obtain short-interval snap shots of the horizontal distribution of salinity in a shallow tidal junction in the Ota River network, Hiroshima, Japan. The remainder of this paper is structured as follows. Section 4.2 includes descriptions of the study area and methods. Section 4.3 details the inverse method of the sound speed field. Section 4.4 presents the inverse results at the junction. Section 4.5 further discusses the advection of salinity at the junction based on the tidal currents and salinity reconstructed by the FAT. Finally, Section 4.6 presents the main conclusions.

4.2. Study area and methods

4.2.1 Study area

The studied tidal junction in this work is well introduced in Chapter 3.2, here, we only briefly introduce it. The studied tidal junction is situated in the mid-reach of the Ota River network (Figure 3.1), almost 2.5 km

downstream from the Oshiba gates and almost 5.8 km upstream from the river mouth, which is under the influence of saltwater intrusion and the freshwater discharge flowing from upriver areas.

4.2.2 Instruments and Methods

The instruments and methods were well introduced in Chapter 3.2, here, we do not introduce their details. The FAT observation was carried out for ~34.4 days (February 21–March 26, 2020), which covered two fortnightly tidal cycles (spring/neap cycle). Six acoustic FAT transducers were placed along the riverbanks in an area approximately 310 m long and 170 m wide (Fig. 3.1c). The detail information of the FAT observation was described in Chapter 3. The successful percentages of sound transmission data along 14 rays varied from 19% to 92% (in Chapter 3). The summation of travel time series data was smoothed by a 30-min low-pass filter to remove high-frequency noise, and, subsequently, be utilized in the inverse analysis to reconstruct the sound speed fields.

As shown in Fig. 3.1c, three 2 MHz ADCPs (Aquadopp Profiler, Nortek) were placed to observe the 3D velocities in the water column, with a 60-second average interval and a 2-min sampling interval close to stations S1 and S3, and a 5-min sampling interval close to station S5. The detail information of ADCP observations were described in Chapter 3. During the observation period, S1-ADCP and S5-ADCP were attached a conductivity–temperature–depth sensor (Compact-CTD, JFE Advantech) near the bottom (~0.1 m) to collect salinity, temperature, and depth. S3-ADCP and station S2 (~0.1 m) were attached the CT (conductivity–temperature) sensor to collect salinity and temperature. Due to the difference in the battery life of each sensor, observations close to stations S1-ADCP, S2, S3-ADCP, and S5-ADCP were performed from February 21 to March 2, February 21 to March 26, February 21 to February 29, and February 21 to February 25, respectively.

The horizontal distributions of the depth-averaged velocity were mapped by the inverse method and detailed in section 3.2. Here, we only focus on the sound speed inversion.

4.3. Theoretical analysis

4.3.1 Forward problem

The sound travel time along the reciprocal ray path Γ_{\pm} between two acoustic transceivers can be written in Eq. 3.

Since this study requires the salinity calculation, it is necessary to eliminate the parameters that linked to the salinity. The summation of the travel time can be expressed by:

$$\delta t_i = t_i^+ + t_i^- - t_m \approx -2 \int \frac{\delta C}{c_m^2} ds \quad (8)$$

The Eq. (8) is a kind of integral equation with unknown variable δC and can be solved with the inverse analysis.

4.3.2 Inverse problem of 2D salinity fields

In the Cartesian coordinate system, the Fourier expansion formula of δC can be expressed as [99]:

$$\begin{aligned} \delta C(x, y) &= a + \sum_{k=0}^{N_x} \sum_{l=0}^{N_y} \left\{ A_{k,l} \cos 2\pi \left(\frac{kx}{L_x} + \frac{ly}{L_y} \right) + B_{k,l} \sin 2\pi \left(\frac{kx}{L_x} + \frac{ly}{L_y} \right) \right\} \\ &= \sum_{j=1}^{(N_x+1)(N_y+1)} D_j Q_j(x, y) \end{aligned} \quad (9)$$

Where:

$$D = \{D_j\} = \left\{ a, A_{00}, B_{00}, A_{01}, B_{01}, \dots, A_{N_x N_y}, B_{N_x N_y} \right\}$$

$$Q\{x, y\} = \{Q_j\}$$

$$\begin{aligned} &= \left\{ 1, 1, 0, \cos \frac{2\pi y}{L_y}, \sin \frac{2\pi y}{L_y}, \dots, \cos 2\pi \left(\frac{N_x x}{L_x} \right. \right. \\ &\quad \left. \left. + \frac{N_y y}{L_y} \right), \sin 2\pi \left(\frac{N_x x}{L_x} + \frac{N_y y}{L_y} \right) \right\} \end{aligned}$$

Where (x, y) represents the two-dimensional position coordinates, (L_x, L_y) is the size of inversion domain and N is the truncated number of the Fourier series. In order to decrease the periodicity effect in the solution, the inversion area should be taken larger than the tomography area [100]. In this work, the inversion domain was set to 620 m length by 340 m width.

The number of truncated Fourier series coefficients was set to 3 in this work. Substituting Eq. (9) into Eq. (8), we can obtain the following formula [99]:

$$\delta t_i = -\frac{2}{c_m^2} \sum_{j=1}^{(N_x+1)(N_y+1)} D_j \int_0^{L_i} Q_j ds \quad (10)$$

The Eq. (10) establishes the relationship between the summation of travel time δt and the sound speed deviation δC . By solving this equation, the sound speed in the calculated domain can be obtained. The corresponding salinity field can be calculated by substituting it into the empirical formula of sound speed which was proposed by Medwin (1975). This empirical formula is as follows

$$C = 1449.2 + 4.6T - 0.055T^2 + 0.00029T^3 + (1.34 - 0.010T)(S - 35) + 0.016D \quad (11)$$

In the Eq. (11), C indicates the sound speed, while T , S , and D represent temperature, salinity, and depth, respectively. Owing to the shallow water of the experimental area in this study, the acoustic signal path is approximated as a straight line, and therefore the change of depth item can be ignored.

In matrix notation, Eq. (10) can be written in the form of a general inverse problem as [99]:

$$y = Ex + e \quad (12)$$

In this equation, $y = \{\delta t_i\}$ represents the travel time information obtained from the FAT experiment, $x = \{D_j\}$ represents the unknown coefficient matrix, $E = \left\{ -\frac{2}{c_m^2} \sum_{j=1}^{(N_x+1)(N_y+1)} \int_0^{L_i} Q_j ds \right\}$ represents the know coefficient matrix, e represents the error.

The expected solution of Eq. (12) is obtained by the damped least-squares method described by Yamoaka et al. (2002) and Yamaguchi et al. (2005). Damped least-squares method accompanied by L-curve method is an optimal method and is suitable for function expansion method, which does not require a smoothing process in inverse analysis.

In this work, there were minimal differences between the temperature and salinity recorded at the four stations (S1-ADCP, S2, S3-ADCP, S5-ADCP). The relative errors of mean sound speed difference refer to the mean sound speed (1456 m/s) and the salinity error result from the sound

speed difference less than 0.5% and 1.85, respectively. The sound speed did not change considerably at the tomography area. Hence, we selected the temperature and salinity recorded at S2 as the reference data, because it recorded data over the longest time period.

Along one transmission line, we can assume that $u \ll C$, thus C can be calculated by L/t_m , where L denotes the station-to-station distances, and t_m denotes the average sound travel time along the reciprocal ray path. By taking the C -derivative of sound speed, and according to Medwin's formula for sound speed, we obtained $\delta C = 3.68 \delta S$, with $H=3$ m, $T=10$ °C, and $S=25$, denoting the water level, reference temperature, and salinity, respectively, for a particular observation area.

Sound speed inversion is sensitive to station-to-station distances, and the distance correction is required. First, the method for correcting distance proposed by Zhang et al. (2015) was applied. Second, an artificial fine-tuning method of distance was also considered by make sure the mean temperature difference between FAT and CT/CTD was minimized to <0.1 °C, because the sound speed/temperature profile remained constant in the water column within the period with no salinity. The original and final ranges of the 14 transmission lines are listed in Table 4.1.

Station pair	GPS distance (m)	Corrected distance (m)	Range offset (m)	Sound speed Offset (m/s)	Salinity Offset
S1-S2	84.29	84.54	0.25	4.30	1.17
S1-S3	216.59	217.09	0.50	3.40	0.92
S1-S4	134.75	135.71	0.96	10.20	2.77
S1-S5	105.94	105.38	0.56	7.70	2.09
S1-S6	108.18	107.58	0.60	8.20	2.22
S2-S3	159.34	158.69	0.65	5.90	1.60
S2-S4	183.98	185.08	1.10	8.60	2.33
S2-S5	188.54	187.84	0.70	5.40	1.46
S2-S6	191.87	192.67	0.80	6.10	1.65
S3-S4	220.95	221.78	0.83	5.40	1.46
S3-S5	285.88	284.58	1.30	6.70	1.82
S3-S6	315.23	318.13	2.9	13.2	3.58

S4-S5	95.46	94.76	0.7	11.1	3.01
S4-S6	164.42	165.21	0.79	7.0	1.90

Table 4.1 Comparison of the GPS-determined and corrected distances. The Salinity offset reference to the typical environment of $H = 3$ m, $T = 10$ °C, $S = 25$.

4.4. Results

4.4.1 Range averaged salinity

Range averaged salinity of three selected transmission lines (S2-S3, S4-S5 and, S3-S6) during the observation period were calculated from the averaged travel time data (Figure 4.1). Salinity varied within a range of 0-30. The salinity peak lags the high water during the spring tide. On the other hand, the salinity peak for neap tide is realized just at the high water. After the heavy rain, salinity waters were flushed out in the time plots during 10-19 March at the junction. Higher salinity occurred at the line S4S5 (downstream) than line S2S3 (upstream), indicated a salinity gradient of saltwater intrusion at the junction.

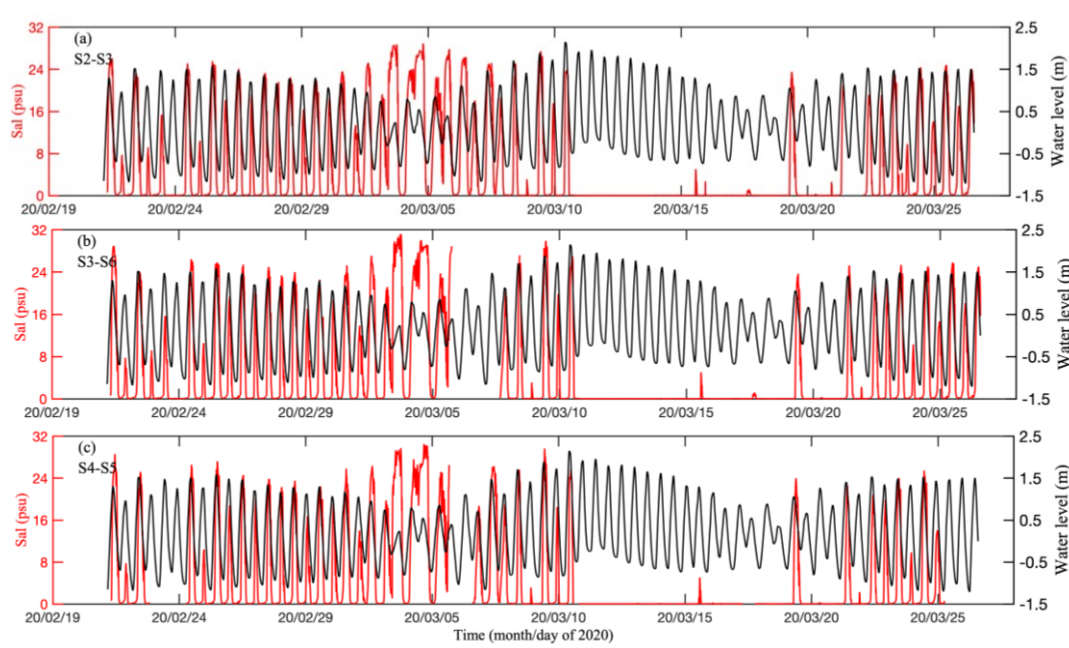


Figure 4.1 Time plots of the range averaged salinity calculated for the selected three transmission lines during the observation period.

Figure 4.2 shows the temperature and salinity obtained by CT sensors

and Compact-CTDs at four stations (S1-ADCP, S2, S3-ADCP, S5-ADCP, Figure 3.1). Range averaged salinity exhibits the same fluctuations of salinity compared with the salinity results obtained from four fixed-point observations and indicates the semi-diurnal variation of salinity at the junction. It can be confirmed that FAT estimates seem reasonable compared with the CT sensors and Compact-CTDs results (Figures. 4.1 and 4.2b). The slight differences between FAT and CT sensors and Compact-CTDs results mainly result of: i) CT sensor or Compact-CTD is one-point measurement while FAT measurement is cross-sectional averaged salinity; ii) The ray length of FAT changes due to the tide. Salinity estimated by FAT is highly sensitive to the relative error of ray length.

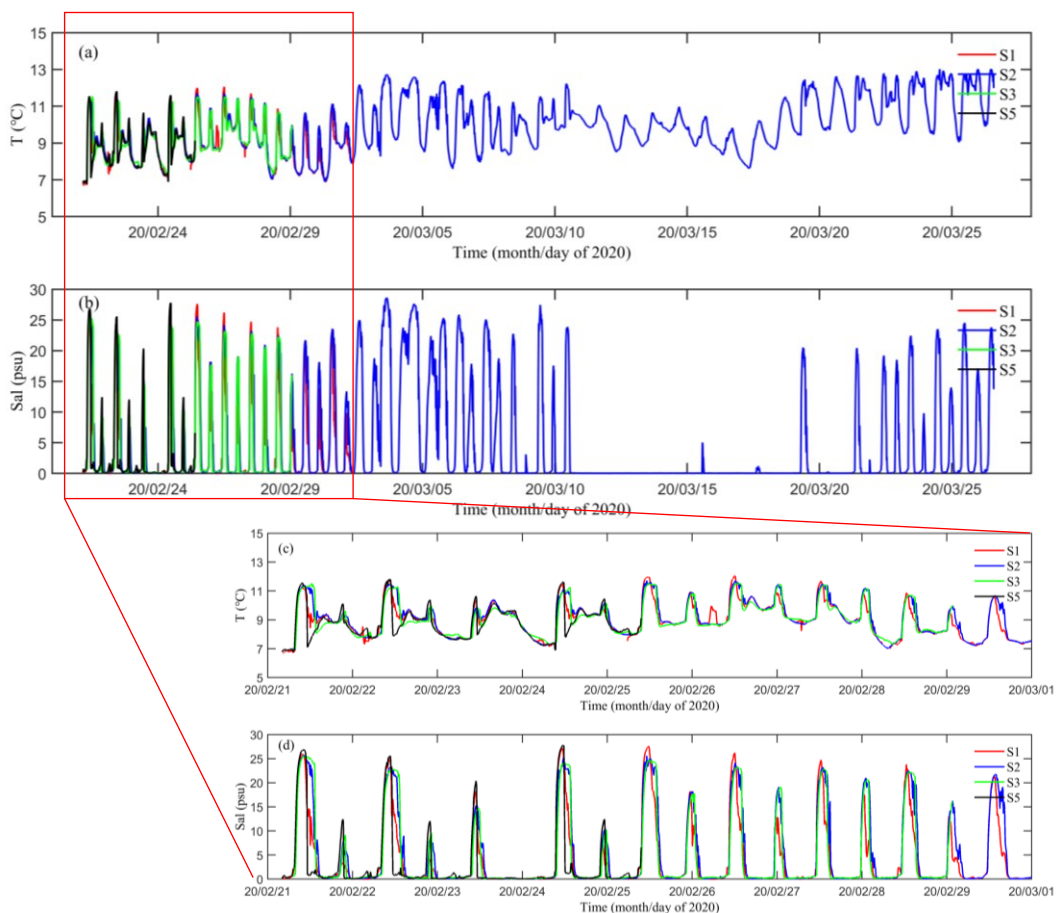


Figure 4.2 Time plots of the temperature and salinity obtained from the four fix stations during the observation period.

4.4.2 2D salinity distributions

The results of the 2D salinity distribution reconstructed by inverse analysis are shown at a 1-hour interval in Figures. 4.3 and 4.4. The salinity

distribution pattern responded well with the tide, high salinity occurred at the high water, whereas salinity was negligible at the low water. During spring tide, A tongue of saline water begun to develop landward from the line S4-S5 (Figure 4.3) and reached the maximum of salinity after the high water (Figure 4.3). After the mature phase, the saline tongue gradually retreated seaward up to the low water (Figure 4.3). From the appearance of saline wedge (Figure 4.3) to the mature phase (Figure 4.3), it took about 3 hours to complete the salinity pattern.



Figure 4.3 Temporal variations of the depth-averaged velocity and salinity distribution at a 1-hour interval during spring tide. The FAT stations are marked by black dots, and the actual acoustic transmission rays among the FAT stations are connected by the solid lines. The tidal phase of each sub-figure is signaled by a black dot on the water level at the lower right corner.

During neap tide, as shown in Figure 4.4, the process of salinity distribution differed from the reciprocating patterns observed during the spring tide. A tongue of saline water begun to develop landward from the line S4-S5 and reached a mature phase around the high water. The

difference was that the salinity did not decrease to zero with the decreased water level. During neap tide, the salinity distributions at flood slack and ebb slack were quite similar due to the small tidal currents. The difference of salinity value between flood and ebb tide were small due to the small tidal range during the neap tide.



Figure 4.4 Temporal variations of the depth-averaged velocity and salinity distribution at a 1-hour interval during neap tide. The FAT stations are marked by black dots, and the actual acoustic transmission rays among the FAT stations are connected by the solid lines. The tidal phase of each sub-figure is signaled by a black dot on the water level at the lower right corner.

4.4.3 Temporal salinity variations at the junction

The inverse salinity data correspond to a total of 33 full semi-diurnal tidal cycles. As shown in Figure 4.5, each tidal cycle starts at lower low water and finishes at the following lower low water to obtain one full semi-diurnal tidal cycle (1 min interval, 24.4 hours). Generally, three distinct

cases in salinity variations exhibited during the observation period at the junction, as shown in Figure 4.5a. Type I (black lines), salinity variabilities were characterized by two local maxima, corresponding to the appearance of high water. Type I, with the first maximum greater than the second maximum. From the appearance of salinity to the maximum salinity, then gradually decreases to zero, it took around 6 hours to complete the process (Figure 4.5a); Type II (red lines), similar to Type I, the maximum salinity occurred around the high water. The difference was that the salinity around the low water within Type I were greater than that within Type II. The second maximum salinity behaved a significant time lag of high water; Type III (green lines), behaviors of salinity pattern with Type III exhibited both two characters of Type I and Type II.

Corresponding three types to the water level time series, we can clearly identify the differences. Type II corresponds to the salinity variability during neap tide, type III corresponds to the period before and after neap tide, and type I corresponds to the period except the neap tide. Tidal-excursion distances calculated from the inversed depth-averaged velocities are given in Figure 4.5d. For type I, tidal-excursion distances were compared for the flood tide and ebb tide, so that the salinity variabilities were compared within the type I. For type II, tidal-excursion distances during flood tide showed a little greater than that during the ebb tide. The increase of salinity due to the flood tide did not been completely washed away when the tidal phase converted to ebb tide. Hence, the water was still saline at low water level.

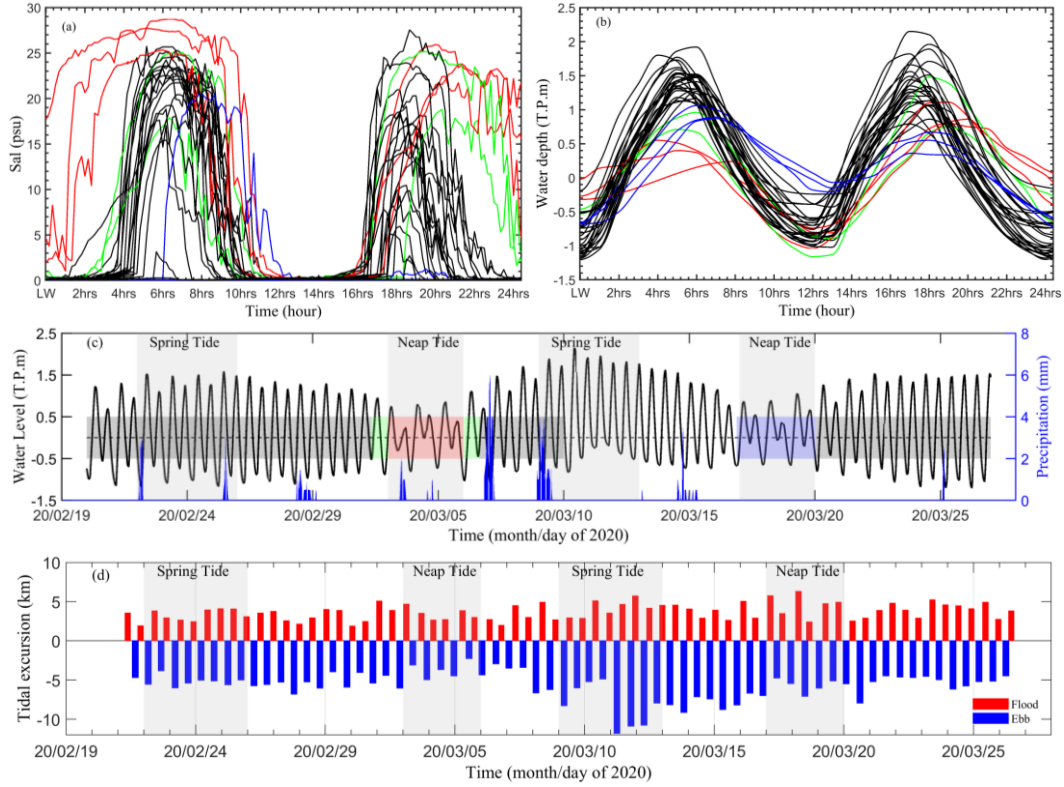


Figure 4.5 (a) salinity and (b) water level variations during the semi-diurnal tidal cycle; (c) the water level data monitored at the Misasa gauging station, and precipitation data were downloaded from the Japan Meteorological Agency; (d) spatially averaged tidal excursion of the flood and ebb tide during the observation period.

4.5. Discussions

4.5.1 Evaluation of the inversion results

As shown in Eq. 5, Sound speed is a function of temperature (T), salinity (S), and depth (D). Reference from the ray simulation results and CT/CTD results, when $T=10$ °C, $D=1.5$ m, the partial derivation of sound speed reduces to:

$$\delta C = \frac{\partial f(T,S,D)}{\partial S} \Big|_{D=1.5, T=10} \delta S \quad (76)$$

According to Medwin's formula for sound speed, we can obtain:

$$\delta C = 1.24\delta S \quad (87)$$

$$\delta C = 3.68\delta T \quad (98)$$

The effect of δT is transferred to δC with a factor of 3.68 within the tomography area, hence, the effect of δT is transferred to δS less than 2.9

psu within the observational area.

Further, to verify the performance of the tomographic results, we compared the inverse estimates with the fixed CT/CTD data. As shown in Figure 4.6, the patterns of the salinity reconstructed by FAT were well agreement with the fixed CT/CTD results (Figure 4.6). The magnitudes of the salinity acquired by FAT were a little less than the fixed CT/CTD values, which result from the reason that the fixed CT/CTD monitors the salinity close the bottom, however, the inverse results were the depth-averaged values.

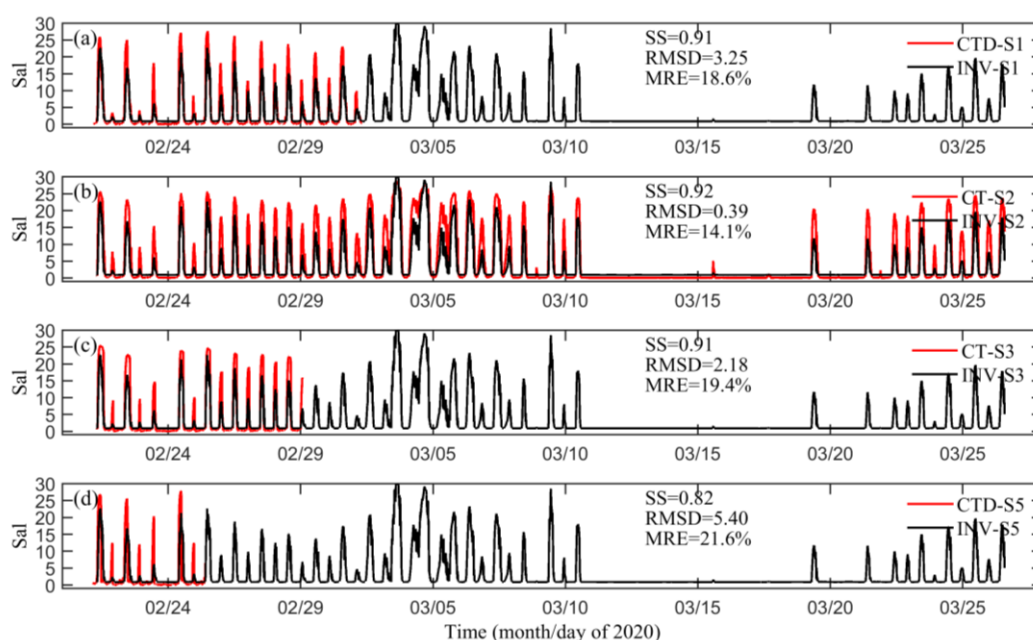


Figure 4.6 Relationships of salinity between fluvial acoustic tomography (FAT) system and conductivity-temperature-depth (CTD)/conductivity-temperature (CT) sensors: (a) S1-ADCP, (b) S2, (c) S3-ADCP, and (d) S5-ADCP. The skill score (SS), the root mean squares difference (RMSD), and the mean relative error (MRE) are given at each panel. S1, S2, S3, S5 are station 1, 2, 3, and 5, respectively; ADCP - Acoustic Doppler Current Profiler. Comparisons of salinity obtained from inverse results and CT/CTD results.

Similar to the currents, the range averaged sound speed along the 14 sound transmission lines between inverted and observed FAT data are compared in Figure 4.7. The SS, RMSD, and MRE between inverted and observed FAT data ranged from 0.75 to 0.92, 3.07 to 5.55 m/s, and 0.02%

to 0.17%, respectively. The results for all station pairs showed good agreements between the inverted and observed FAT data. Furthermore, the uncertainty maps of the inverse solutions of sound speed were also calculated and are shown in Figure 4.8. The uncertainties of sound speed were ~ 1 m/s in the tomography domain (Figure 4.8). The effect of sound speed uncertainty results in the salinity uncertainty were ~ 0.27 ($\delta C = 3.68 \delta S$), for the environment of $H = 3$ m, $T = 10$ °C, and $S = 25$.

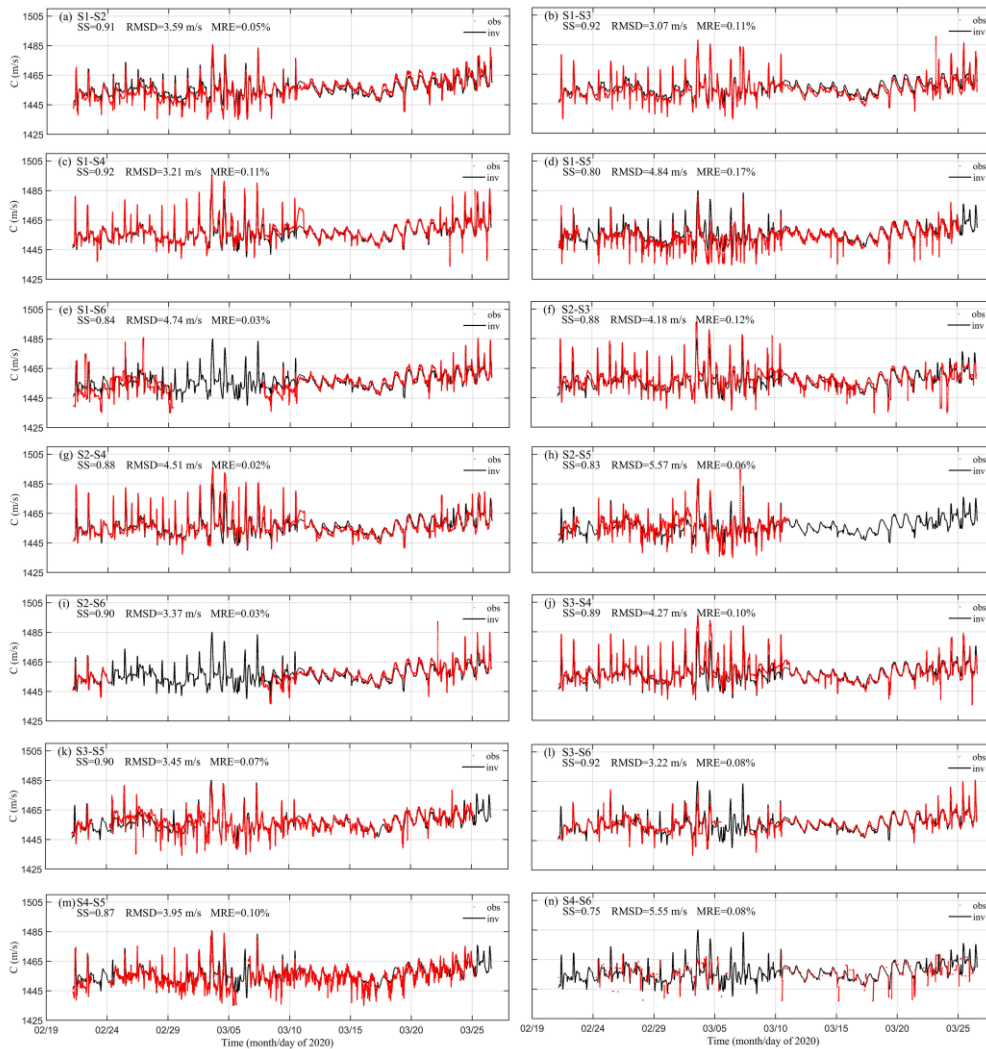


Figure 4.7 Time plots of the inverted (black lines) and observed (red dots) range averaged sound speed calculated along each transmission line. The skill score (SS), root mean squares difference (RMSD), and mean relative error (MRE) are provided in each panel.

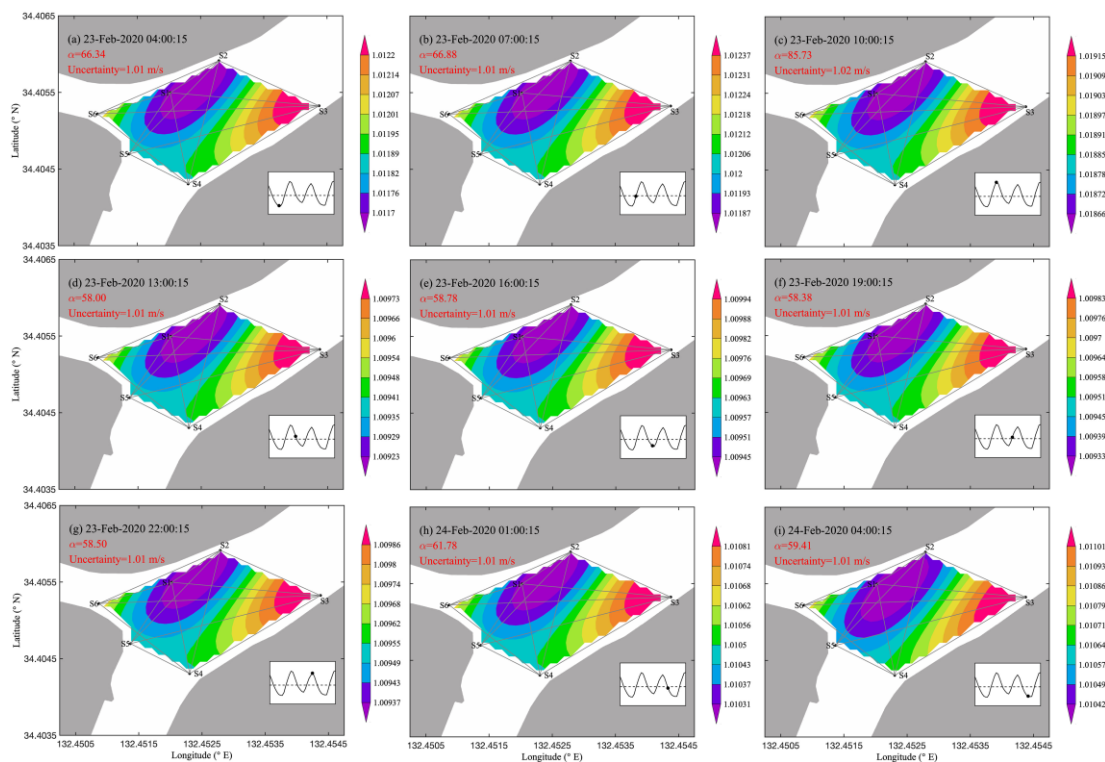


Figure 4.8 Uncertainty maps of inverse solutions of sound speed during spring tide corresponding to the salinity distributions given in Figure 3.6. The values of the damping factor α and the spatially averaged uncertainty of each figure are provided in the upper left corners of the respective figures.

The comparison of sound speed calculated by CT sensor at S2 and inversed sound speed was shown in Figure 4.9. During the salinity calculation, the data recorded at S2 was used as the reference data and it recorded the longest data, hence, here one comparison of sound speed between inverse result and calculated sound speed at S2-CT was shown. The patterns of sound speed reconstructed by FAT were well agreement with the fixed CT results (Figure 4.9). The maximum magnitudes of sound speed acquired by FAT were a less than the fixed CT values, which mainly result from the reason that the fixed CT monitors the data close the bottom, however, the inverse results were the depth-averaged values.

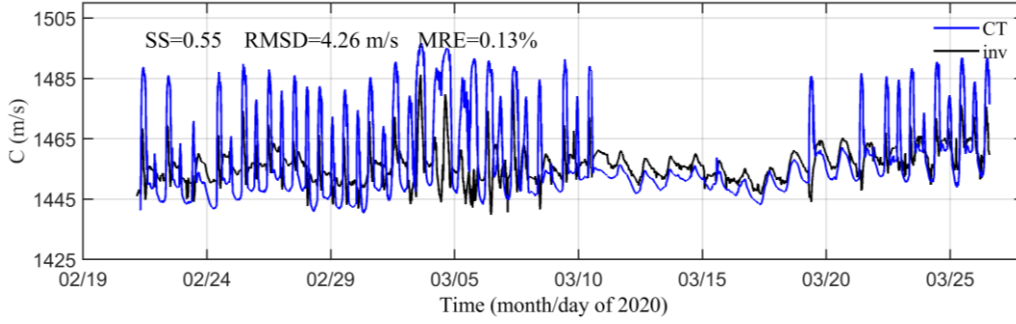


Figure 4.9 Time plots of the inverted sound speed (black line) and the sound speed calculated by the CT sensor at S2 (blue line). The skill score (SS), root mean squares difference (RMSD), and mean relative error (MRE) are provided in each panel.

4.5.2 Advection of salinity at the junction

The total salinity change was divided into three parts which were controlled by advection, upwelling and mixing [102].

$$\frac{\partial S}{\partial t} = - \left(u \cdot \frac{\partial S}{\partial x} + v \cdot \frac{\partial S}{\partial y} \right) - w \cdot \frac{\partial S}{\partial z} + \frac{\partial \left(k_v \frac{\partial S}{\partial z} \right)}{\partial z} \quad (13)$$

where S is salinity, u , v , and w are east, north and vertical velocity components, respectively, and k_v is the vertical eddy diffusivity coefficient. Here, the salinity and velocities were taken from the inverse analysis and were the depth-averaged values. In this work, we only discuss the advection of salinity based on the inversed depth-averaged salinity and velocity in Chapter 3.

During the spring tide, the negative advection (seaward) of salinity occurred in the upstream of the junction, while the positive advection (landward) of salinity occurred at the downstream of the junction (Figure 4.10a). The residual currents during the spring tide verified that the flow velocities at the upstream showed higher velocities (Figure 4.10a). During the neap tide, the pattern of the advection of salinity almost similar to that during spring tide, the different place is the positive advection of salinity dominated at the downstream of the junction (Figure 4.10b), and the positive area larger than that during the spring tide. Behaviors of salinity pattern at the junction exhibited that the maximum salinity during neap tide is higher than that during the spring tide, and the higher advection of salinity also higher than that during the neap tide. The main reason results from the density-driven current phenomenon at the junction. During the

spring tide, the water was well mixing, the seaward pressure-driven currents and the landward density-driven currents both controlled the river-tidal dynamics. The seaward advection of salinity mostly results from the ebb-dominant system and the river flow. However, during the neap tide, significant stratification was existing, landward density-driven currents dominated the river-tidal dynamics, which would result in a longer salinity intrusion and higher salinity at the bottom. There seems to be a balance of salinity at the junction during the spring tide, while during the neap tide, due to the density-driven currents, significant intrusion and accumulation of salinity happened at the junction.

As shown in Figure 4.11, the vertical velocity profiles closed to station S3 during spring and neap tide verified it. The ebb/flood velocities decrease from the surface to the bottom in the water column during the spring tide (Figure 4.11a), while the ebb velocities appeared distinct stratification during the neap tide (Figure 4.11b).

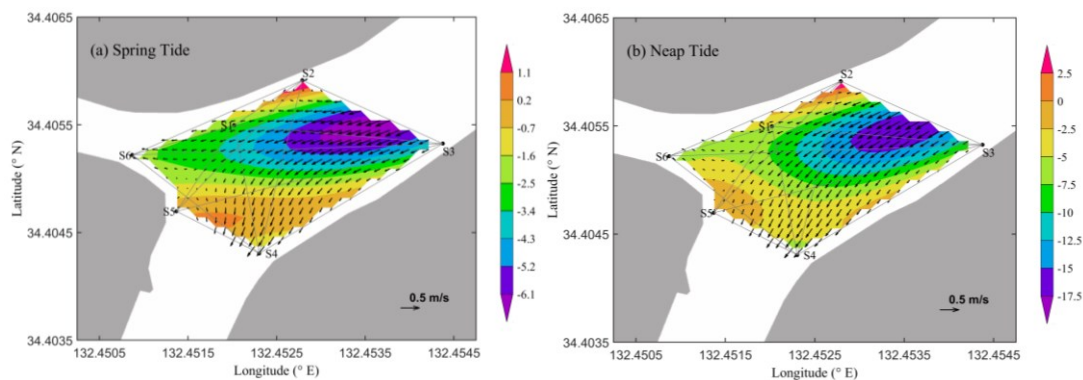


Figure 4.10 (a) The distribution of advection of salinity and residual currents at the junction during spring tide; (b) The distribution of salinity and residual currents at the junction during neap tide.

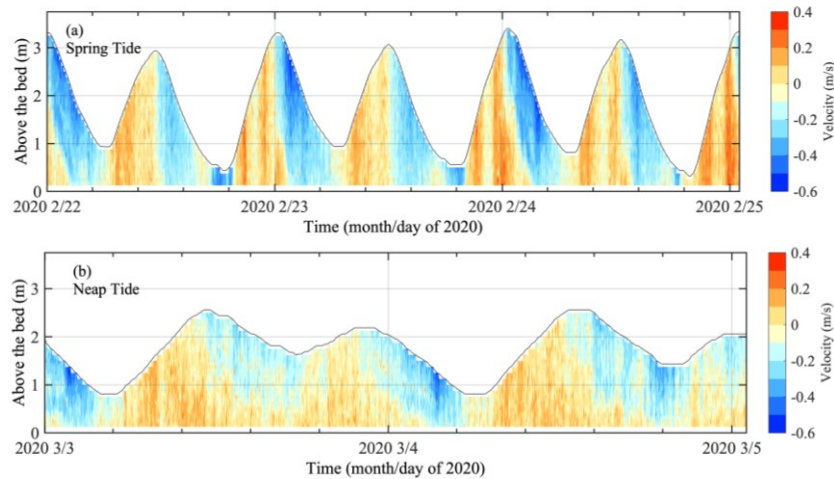


Figure 4.11 Temporal variations of the velocity profiles (positive indicates flood, upstream) at Station S3-ADCP during spring and neap tide.

4.5.3 Comparison of other estuaries

In single-channel estuaries, saltwater wedge usually develops in the along-channel direction. However, in bifurcated estuaries, lateral saltwater intrusion may be noteworthy and can play an important role in determining the phase of peak salinity in the spring/neap tidal cycle. Numerous studies have revealed that the distribution of salinity in estuaries is affected primarily by the volume of river discharge and the magnitude of tidal current [62], [103], [104].

The Cape Fear River Estuary (approx. 50 km in length with a mean tidal range of 1.3 m) located in the southeast Atlantic coast of the USA, which is representative of a river-dominated estuary. The freshwater discharge was an important cause of variability in salinity intrusion [97]. Besides, they also found that intra-tidal and tidal range differences significantly influenced salinity structure along the channel: increased stratification occurred on the ebb tide compared with the flood tide and increased stratification resulted from reduced vertical mixing at lower tidal ranges.

The Yangtze River Estuary (120 km long and 90 km wide) as a mesotidal estuary with a mean tidal range of 2.66 m at the mouth, which exhibits multilevel bifurcations [94]. Due to the multilevel bifurcations of the Yangtze River Estuary, saltwater intrusion from one outlet to another can be expected. In particular, the saltwater spilling over from the North Branch to the South Branch is a well-known phenomenon and it is mostly

due to the recent evolution of the topography [104], [105].

The Ota River estuary is characterized as a mixed-semidiurnal and mesotidal network system with the tidal range varying from 2 to 4 m [9], [11]. Kawanisi et al. (2015) investigated the salinity intrusion in the Otagawa floodway (the western branch of the Ota River network) using FAT. They revealed that the semidiurnal variations of salinity were diminished owing to the Gion gates opening because the saltwater was flushed out by the freshwater discharge. In this instance, the recovering time of the salinity along the channel ranged from 9.5 days to 27 days and the recovering time was independent on the flood discharge. In the Ota River estuary, the freshwater discharge is limited during the normal conditions, the salinity dynamics and saltwater intrusion are more sensitive to the tide than discharge.

4.6. Conclusions

In this study, for the first time, continuous 2D salinity fields were measured at a shallow junction using fluvial acoustic tomography (FAT) systems composed of six fixed acoustic stations from February 21 to March 26, 2020. The horizontal structure and the spatiotemporal variation of the salinity were well revealed by FAT. Totally, actual reciprocal sound transmissions were performed during ~ 34.4 days along 14 transmission lines. The salinity estimated by inverse analysis agreed well with the fixed CT sensor and Compact CTD results.

Temporally, salinity during ebb neap tide was higher than that during flood spring tide. Spatially, salinity in the downstream was higher than upstream, suggested a salinity gradient of saltwater at the junction. Further, the advection of salinity during spring and neap tide showed two distinct results. During the spring tide, the water was well mixing. It leads to a balance of salinity transport at the junction. Nevertheless, during the neap tide, significant stratification was existing, density-driven currents dominated the river-tidal dynamics and resulted in a salinity accumulation at the junction.

This study demonstrated that the application of FAT in conjunction with the inverse method presents an effective tool to map the 2D salinity field and to investigate the advection of salinity in a shallow tidal junction in detail.

Chapter 5: Continuous measurements of tidal discharge at a shallow tidal channel junction using the fluvial acoustic tomography system

5.1. Introduction

It is a difficult task to measure tidal discharge in tidal rivers. Due to the complex flow conditions generated by interaction of the saltwater and riverine influences, discharge measurement in tidal rivers should seek an accurate and reliable estimation of the real-time discharge. However, conventional acoustic methods such as acoustic velocity meters (AVMs), horizontal acoustic Doppler current profilers (H-ADCPs), and rating curves lack spatial or temporal resolution [9] and hence fail to meet requirements mentioned above, acoustic tomography method seems to be a potential method for real-time and long-term river discharge measurement, especially in tidal rivers. For one transmission line, such as, a long-term measurement of stream flow and salinity in a tidal river by the fluvial acoustic tomography (FAT) system had been conducted [9]. In addition, some studies have presented various applications of FAT using two crossing paths to reconstruct velocity magnitude and direction; for example, in observations of the dam flush and low flow rate in a mountainous river [40], [107] and in measurements of the tidal flow in a shallow tidal channel [11]. For one transmission line, the flow direction is assumed as a constant value, and there is a considerable error in calculating the tidal discharge. For two crossing transmission lines, the mean flow direction is calculated by the depth- and range-averaged velocity and is changed with the flow conditions, however the mean flow direction cannot well represent the cross-section velocities.

As we discussed in previous chapters, FAT is a potential tool for continuously mapping variable 2D currents in shallow water environments. series data of the 2D flow velocity are helpful to better estimate the flow direction and the tidal discharge. Hence, in this chapter, we applied the inverse velocities to estimate the tidal discharge at the tidal junction.

5.2. Theoretical analysis

The discharge estimated from the FAT with one transmission line and two crossing transmission lines were described clearly in Kawanisi et al. (2010) and Kawanisi et al. (2013), respectively. In this work, the one transmission line and two crossing transmission lines were selected as S2S3, S2S4 and S3S6, as show in Figure 5.1a.

Here, we only introduce the method of how to estimate the tidal discharge from the inverse velocity. The highest spatial resolution of the inversion zone was ~ 7.8 m. In view of the spatial resolution, we selected the velocity along the horizontal transect with the spatial resolution of ~ 15 ($\sim 7.8 \times 2$) m and the selected transect was divided into 11 sub area (Figure 5.1b).

As shown in Figure 5.1c and 5.1d, the velocities along the transect during flood tide or ebb tide, showing a significant spatially variations. The velocity in the direction of flow v is estimated from the eastward and northward velocity components (Figure 5.1a), which are the inverse velocity components. Finally, the tidal discharge is calculated by the summation of tidal discharge at each sub area (Figure 5.1b):

$$Q = Q_1 + Q_2 + \dots + Q_{11} = A_1 v_1 + A_2 v_2 + \dots + A_{11} v_{11} \quad 14$$

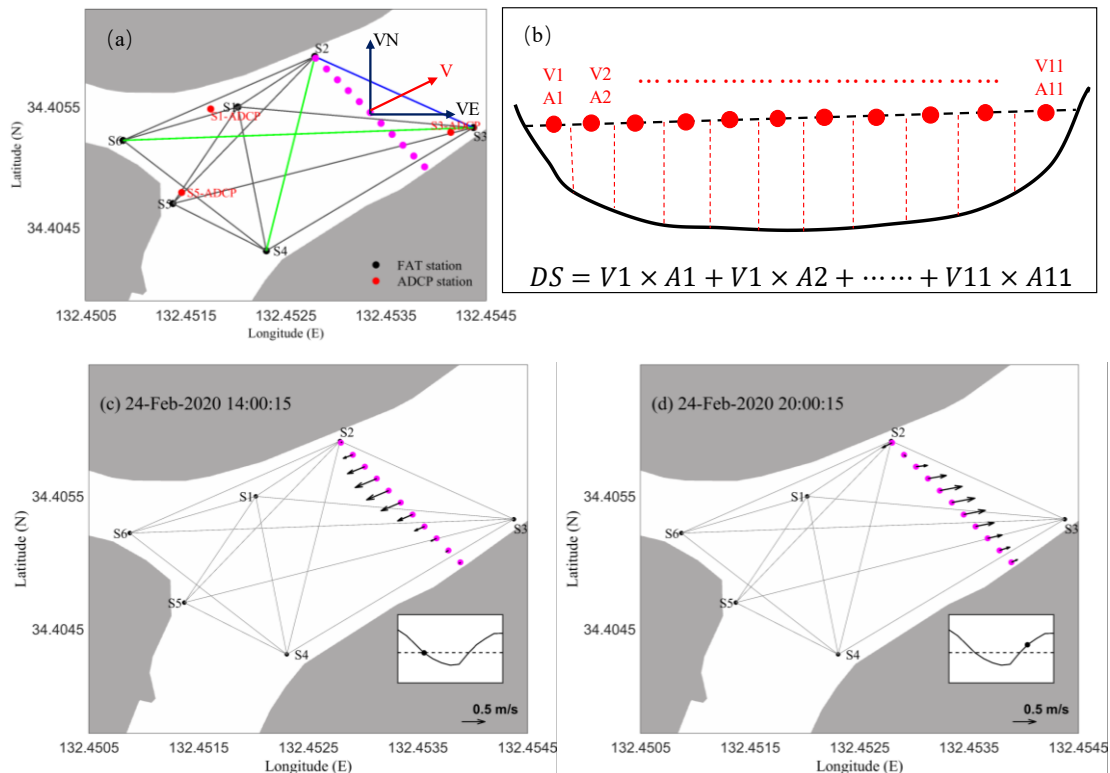


Figure 5.1 (a) Schematic map of the tidal junction, (b) sketch of the tidal discharge measurement, examples of the depth-averaged tidal currents along the selected transect (c) ebb tide and (d) flood tide.

5.3. Results and discussion

5.3.1 Cross-sectional average velocity

Figure 5.2 shows the time series of cross-sectional average velocity of S2S3, S2S4 and S3S6. The velocities from ADCP and FAT show high similarity during low flow period, while during high flow period, FAT shows underestimate results compared to ADCP results. This is result from the difference that FAT calculates the cross-sectional average velocity, whereas ADCP results are the depth-averaged values at one point.

Figure 5.3 shows the time series of inverse velocity at each sub area. Similar to the cross-sectional average velocity, during low flow period, the differences between inverse velocity and ADCP velocity were small; while, during high flow period, the underestimate results of the cross-sectional average velocity were improved, although there were some differences between two technologies.

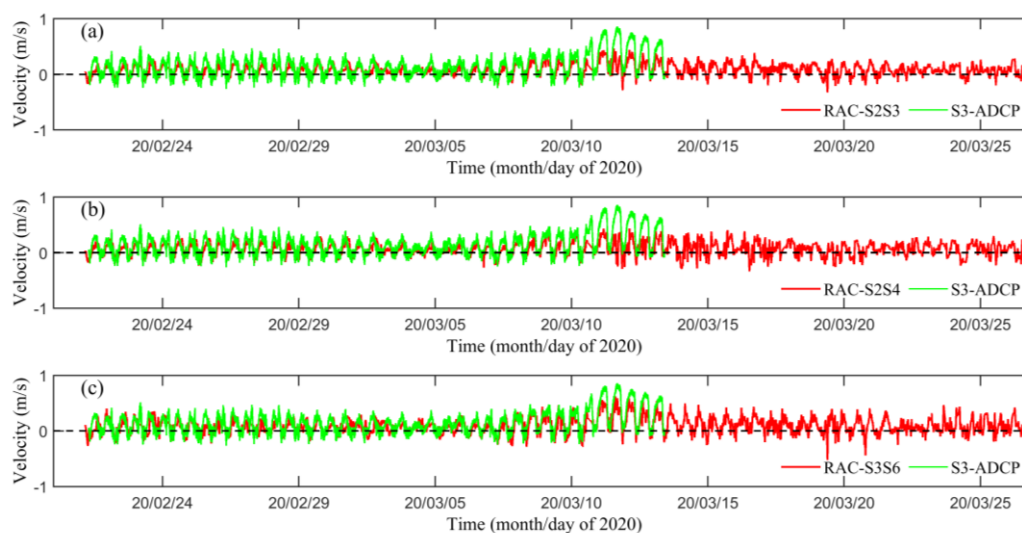


Figure 5.2 Time plots of the range averaged currents for Lines S2S3, S2S4 and S3S6; the green line represents the depth averaged currents obtained at S3-ADCP. (Positive indicates seaward).

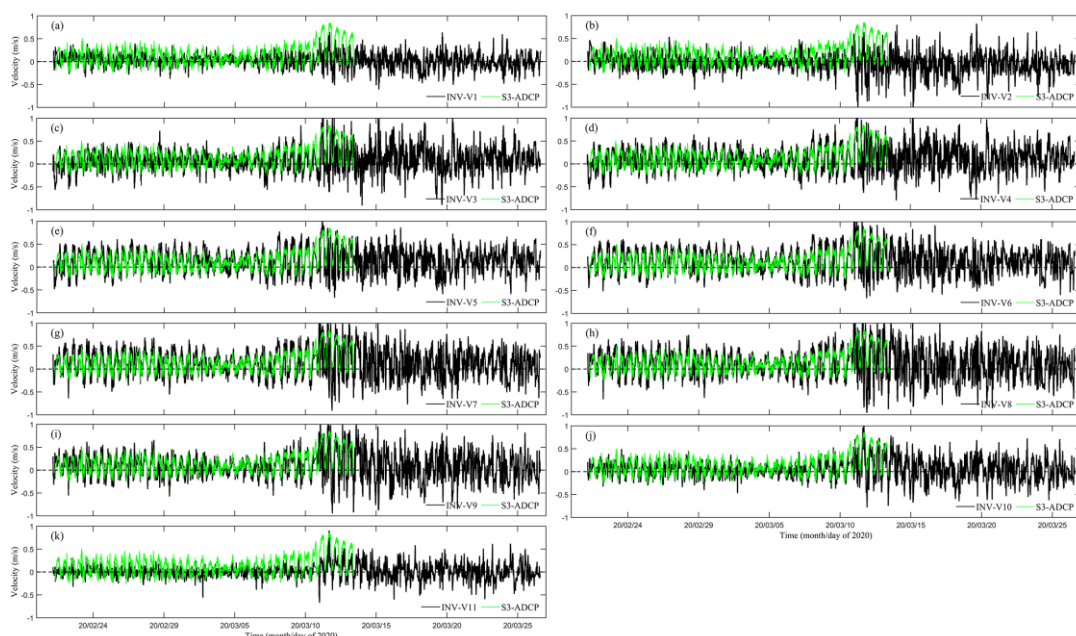


Figure 5.3 Time plots of the sub area currents obtained from the inverse method; the green line represents the depth averaged currents obtained at S3-ADCP. (Positive indicates seaward).

5.3.2 Temporal variations of the flow direction

The FAT mean flow direction is computed from the two crossing paths S2S4 and S3S6, as shown in Figure 5.4a. The flow direction at each sub area is shown in Figure 5.4b - 5.4l. All the flow directions are respected to north direction. Note that the mean flow direction averaged over a bulk of flow (about 220 m long, 150 m wide, and variable river depth), while the flow direction within each sub area covers the distance with ~ 15 m.

Due to high spatial variability of flow distribution, stationary ADCP measurements and moving boat ADCP methods were not likely to provide reference data for the cross section. FAT is an innovative acoustic technology that utilizes the time-of-travel method to determine velocity and direction from multiple ray paths that traverse the entire cross-section of stream. Moreover, inverse velocity of FAT provided another way that 2D data can provide a visual means of determining flow division and spatiotemporal difference of velocity and direction.

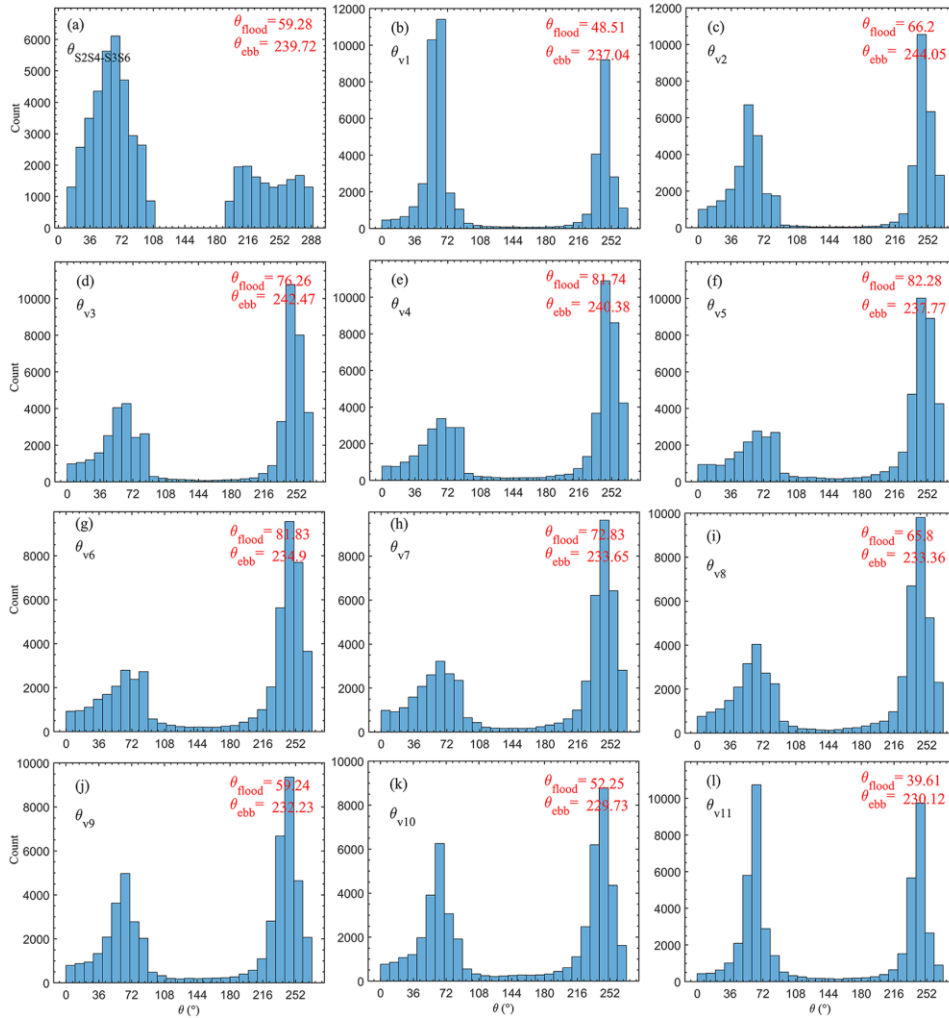


Figure 5.4 Histogram of the flow direction calculated from (a) the range averaged velocity of S2S4 and S3S6; (b) - (l) the inverse velocity at each sub area.

5.3.3 Temporal variations of the tidal discharge

Figure 5.5 shows the temporal variations of the tidal discharges calculated by three methods at the junction. The tidal discharge calculated by three methods show the similar patterns. The tidal discharge shows the semidiurnal characteristic and range from -150 to 270 m^3/s .

Figure 5.6a shows the compare results of three methods, all methods show the high coefficients of determination ($R^2 > 0.9$) and the low root mean square error (RMSE). Moreover, Figure 5.6b shows the relative differences (RE) between Q_{FAT} and Q_{ADCP} ranged approximately between -25% and 25% . The results of two crossing transmission lines and the summation of tidal discharge at each sub area exhibit high accuracy than

the results of one transmission line. The results of two crossing transmission lines and the results of the summation of tidal discharge at each sub area exhibit similar variations, and the latter exhibit a litter improve of the high values.

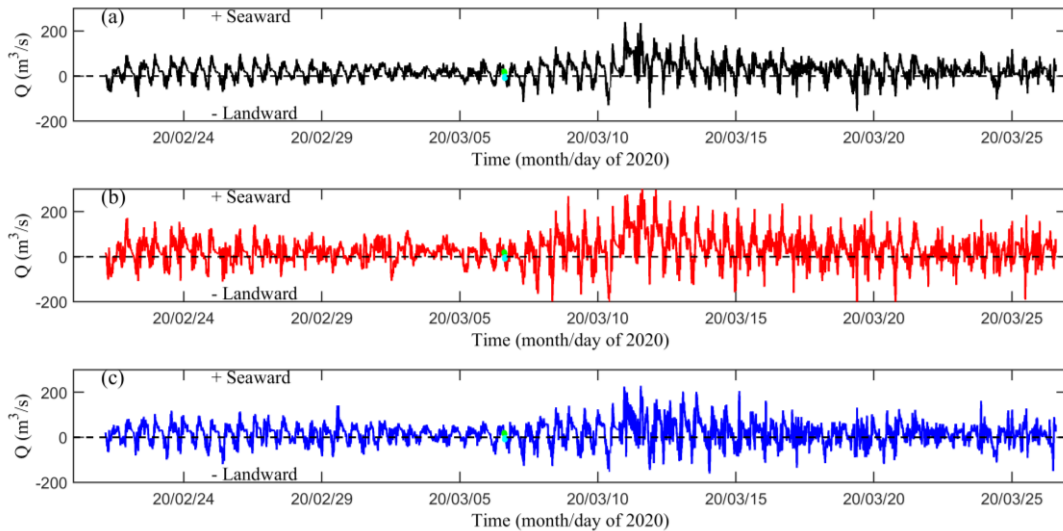


Figure 5.5 Time plots of the tidal discharge obtained from three methods (a) one transmission line S2S3; (b) two crossing transmission lines S2S4 and S3S6; (c) summation of tidal discharge at each sub area. The green dots denote the tidal discharge obtained using StreamPro ADCP.

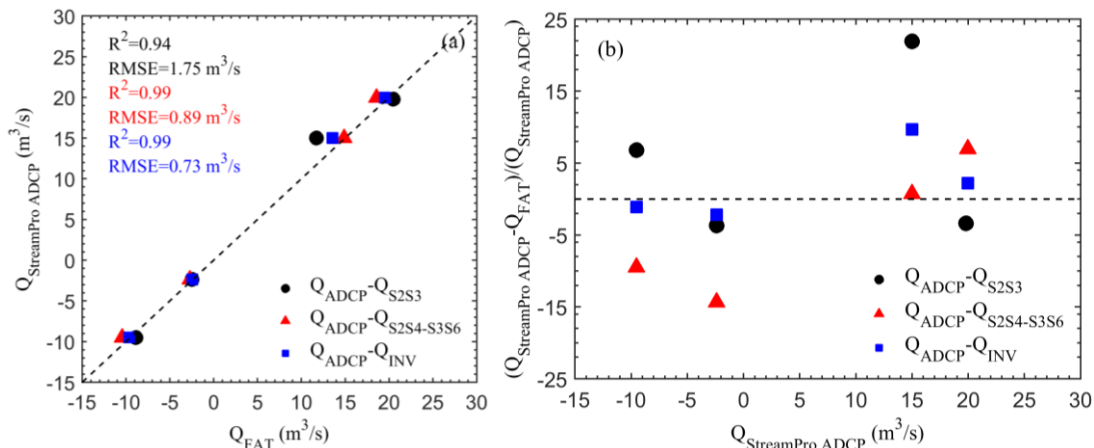


Figure 5.6 Comparisons between the tidal discharge measure by FAT and StreamPro ADCP.

The most important reason for the difference of the tidal discharges between three methods is the calculation of flow direction. For one transmission line, the flow direction was assumed as a constant value; for

two crossing transmission line, the flow direction was calculated by cross-section averaged velocity, although the flow direction was changed with the flow conditions, it was the cross-section averaged values; while for the inverse velocity method, the flow direction was calculated at each node (Figures 5.1c and 5.1d, Figure 5.4), the flow direction shows the spatial and temporal variations.

5.4. Conclusions

For long-term monitoring purposes, FAT equipped with six 30 kHz transducers was deployed to estimate 2D velocities by inverse method and tidal discharge at a shallow tidal junction. In spite of complexity of the flow pattern, it was concluded that FAT represents a promising method/sensor for the continuous monitoring of tidal discharge and 2D tidal currents.

The tidal discharge measured by three methods (one transmission line, two crossing transmission lines and the summation of tidal discharge at each sub area), varied from -150 to 270 m³/s during the experiment period. The results calculated from the two crossing transmission lines and the summation of tidal discharge at each sub area exhibit high accuracy than the results estimated from the one transmission line. The results of two crossing transmission lines and the results of the summation of tidal discharge at each sub area exhibit similar variations, but the latter exhibit a little improve of the high values (~6% improve).

Chapter 6: Conclusions and Future works

6.1 Main conclusions

Although this study dealt with the Ota River network as a case-specific example, the presented results and discussion are not limited to demonstrate the dynamic of SSC, flow patterns, and salinity patterns with the effects of the interactions between river flow and tide, but also take the advantages of utilizing the innovative hydro-acoustic system (FATs) for measuring 2D tidal currents, 2D salinity, and tidal discharge in high temporal resolution and exploring the hydrodynamic process at a tidal junction. Moreover, the findings should increase the knowledge for common hydrodynamic processes in small multi-channel estuaries that have nearly similar environments over the world.

This study focus on: 1) the spatiotemporal variations of suspended sediment by three ADCPs in a tide-controlled channel for around one month, 2) the spatiotemporal variations of 2D tidal currents, salinity and tidal discharge at the tidal junction using six FATs more than one month. The specific conclusions and contributions of this study can be summarized as:

- 1) The relative effects of environmental forcings on the SPMC were evaluated on a seasonal scale by SSA. In summer, the ebb/flood velocities forcing explained 9.6% of the variance, together with the contribution of the spring-neap tide oscillation (81.9%). In winter, the discharge was low and controlled by the Gion gates at upstream, the spring-neap tide oscillation contributed 73.6% of the SPMC variance, together with the 19.5% of variance from the ebb/flood velocities.
- 2) The role of river flow transport at less than $110 \text{ m}^3/\text{s}$ ($Q_{\text{Gion}} \approx 24 \text{ m}^3/\text{s}$) (winter and summer) revealed that tidal pumping has a domain influence on sediment shifting, while significant sediment seaward shifting results from flood events. Furthermore, the convergence zone between tidal and river forcings were detected in the floodway. Upstream transport was observed with tidal pumping in most cases, while significant seaward transport corresponded to episodic flood

events.

- 3) At the tidal junction, during spring tides, temporally, the currents during ebb tides were higher than those during flood tides. Spatially, the currents in the Kyu Ota River were stronger than those in the Tenma River. During the neap tides, the performances of the currents were not as obvious as that during spring tides. A counter-clockwise circulation generated around the low water during neap tide was found by the inverted results. Behaviors of the currents during the neap tide at the junction were likely to be the result of the density-driven currents.
- 4) Tidal harmonic analysis of the reconstructed currents was performed to clarify the interactions between river flow and tide at the tidal junction. A relative larger M_4/M_2 values were observed during spring tides, the increase in the slope of M_4 was lower than that of M_2 with the gradually increased discharge and tidal range. The results reflected the increased tidal wave deformation that occurred with the gradually increased tidal range and demonstrated the role of the limited river flow on the tidal asymmetry at the tidal junction.
- 5) The runoff flow into Kyu Ota River from the Oshiba gates contributed ~20-90% of the Yaguchi discharge during the observation period at the junction. The freshwater discharge was ~29.2% of the tidal discharge during the observation period. During the ebb tides, ~29.2% freshwater discharge would add to the seaward currents, therefore, the ebb tides had the larger velocities than that during the flood tides; while during the flood tides, ~29.2% decrement resulted from the freshwater discharge would affect the flood velocities. The mean residual currents obtained by tidal harmonic analysis demonstrated that the residual currents (river flow) would lead ~22% increment and decrement of ebb and flood velocities, respectively, which also revealed the role of river discharge at the junction, the values of ~22% and ~29.2% were not big difference with the reference velocity 0.5 m/s.
- 6) Temporally, salinity during neap tide was higher than that during spring tide. Further, the advection of salinity during spring and neap tide showed two distinct results. During the spring tide, the water was well mixing. It leads to a balance of salinity transport at the junction. Nevertheless, during the neap tide, significant stratification was existing, density-driven currents dominated the river-tidal dynamics and resulted

in a salinity accumulation at the junction.

6.2 Answers for the research questions

Q1: How does the tidal motion acts to reduce the asymmetric division of flow or sediment over the small multi-channels?

For tidal junction (~5.8 km from the river mouth), the geometry of the junction (width-to-depth ratio) mainly controlled the division of water, the width-to-depth ratio at the western branch was smaller than that at the eastern branch; hence, the discharge tended to flow more toward the eastern branch. However, during neap tide, the counter-clockwise circulation generated at the junction, the asymmetric division at the junction was reduced. This is because the tidal propagation is quicker at the eastern branch than that at the western branch, and gradually become to standing wave at the junction.

Q2: How does the planform remain stability with the interactions between river flow and tide in small multi-channel systems?

The critical river discharge value ($110 \text{ m}^3/\text{s}$) was presented here to demonstrate the effect of tidal pumping and river flow on sediment dynamics in small estuary, reference to the environment of mesotidal range (~1-3 m), mean channel width of ~200 m, and mean river discharge of ~50-60 m^3/s . The tidal pumping effects resulted sediment deposition occurs along the area located between 2.8 km and 4.8 km from the mouth. The convergence between tide and river flow occur at this area and slow down the tidal and river flow effects.

For tidal junction (~5.8 km from the river mouth), the contributions of river flow on tidal currents were ~22%, reference to the environment of mesotidal range (~1-3 m), mean channel width of ~150 m, and mean river discharge of ~50-60 m^3/s . Under the critical value, the environment remains for the stability with tidal domain; higher river flow would destroy the regime and become short river flow domain.

6.3 Future work

The research does not stop, enormous number of points must be investigated in future research:

- Since the convergence area was captured in the tidal dominated channel and explained some of its potential dynamics. It is important to investigate to what effect will it have on the channel in the long term, and what is the intrinsic dynamics of the river flow-tide interactions at the convergence area. Hence, in the future, more detail and longer observations equipped with not only ADCP, but also FATS would help to obtain more systematic data, so that it can facilitate the understanding of the intrinsic mechanism.
- Six FATS with 30 kHz were deployed at the tidal junction to investigate the hydrodynamic of tidal currents and salinity, however the successful percentages of reciprocal sound transmission varied from 19–92%, this leads to some errors in the inverse results at some moments. In the future work, it is recommended to conduct more stable and long-term monitoring by FATS with higher frequency that would help to acquire more reliable data. In addition, to improve the accuracy of the inverse results by assimilating the FATS data into a 3D numerical model is needed. Finally, a holistic understanding of the hydrodynamic of the water circulation at the tidal junction is also need with the more systematic observation data.

Appendix

This dissertation contains of several publications, as follows:

1. Journal publication:

- a) **Xiao, C.**, Kawanisi, K., & Al Sawaf, M. B. (2020). Suspended particulate matter concentration in response to tidal hydrodynamics in a long mesotidal floodway. *Estuarine, Coastal and Shelf Science*, 233, 106525.
- b) Al Sawaf, M. B., Kawanisi, K., & **Xiao, C.** (2020). Measuring Low Flowrates of a Shallow Mountainous River Within Restricted Site Conditions and the Characteristics of Acoustic Arrival Times Within Low Flows. *Water Resources Management*, 34(10), 3059-3078.
- c) **Xiao, C.**, Kawanisi, K., Torigoe, R., Al Sawaf, M.B., Mapping tidal current and salinity at a shallow tidal channel junction using the fluvial acoustic tomography system, *Estuarine, Coastal and Shelf Science* (2021), doi: <https://doi.org/10.1016/j.ecss.2021.107440>.

2. Conference publication:

- a) **Xiao, C.**, Kawanisi, K., & Al Sawaf, M. B. (2020). Mapping tidal currents at a tidal channel junction using fluvial acoustic tomography system. 8th International Conference on the Application of Physical Modelling in Coastal and Port Engineering and Science, Dec. 9th - 12th, 2020, Zhoushan, China. Coastlab2020.
- b) Al Sawaf, M. B., Kawanisi, K., & **Xiao, C.** (2019). Improving the Resolution of Shallow-River Discharge Measurement by Denoising Outliers Using Binarized Image Subtraction Feature. *Journal of Japan Society of Civil Engineers, Ser. B1 (Hydraulic Engineering)*, 75(2), I_619-I_624.

References

- [1] B. F. McCarthy, G. M. de Kruijffa, E. M. Nuijena, and K. M. Cohenb, “The Rhine Meuse delta: an aspired UNESCO Global Geopark,” *NCR DAYS 2018*, p. 106, 2018.
- [2] M. Hiatt *et al.*, “Drivers and impacts of water level fluctuations in the Mississippi River delta: Implications for delta restoration,” *Estuar. Coast. Shelf Sci.*, vol. 224, pp. 117–137, 2019.
- [3] A. Smajgl *et al.*, “Responding to rising sea levels in the Mekong Delta,” *Nat. Clim. Chang.*, vol. 5, no. 2, pp. 167–174, 2015.
- [4] L. Guo *et al.*, “River-tide dynamics: Exploration of nonstationary and nonlinear tidal behavior in the Yangtze River estuary,” *J. Geophys. Res. Ocean.*, vol. 120, no. 5, pp. 3499–3521, 2015.
- [5] L. Guo, M. Van der Wegen, J. A. Roelvink, and Q. He, “The role of river flow and tidal asymmetry on 1-D estuarine morphodynamics,” *J. Geophys. Res. Earth Surf.*, vol. 119, no. 11, pp. 2315–2334, 2014.
- [6] H. Cai *et al.*, “Seasonal behaviour of tidal damping and residual water level slope in the Yangtze River estuary: identifying the critical position and river discharge for maximum tidal damping,” *Hydrol. Earth Syst. Sci.*, vol. 23, no. 6, pp. 2779–2794, 2019.
- [7] B. Wang, J. Zhu, H. Wu, F. Yu, and X. Song, “Dynamics of saltwater intrusion in the Modaomen Waterway of the Pearl River Estuary,” *Sci. China Earth Sci.*, vol. 55, no. 11, pp. 1901–1918, 2012.
- [8] H. Cai, Q. Yang, Z. Zhang, X. Guo, F. Liu, and S. Ou, “Impact of river-tide dynamics on the temporal-spatial distribution of residual water level in the Pearl River channel networks,” *Estuaries and Coasts*, vol. 41, no. 7, pp. 1885–1903, 2018.
- [9] K. Kawanisi, M. Razaz, A. Kaneko, and S. Watanabe, “Long-term measurement of stream flow and salinity in a tidal river by the use of the fluvial acoustic tomography system,” *J. Hydrol.*, vol. 380, no. 1–2, pp. 74–81, 2010.
- [10] M. M. Danial, K. Kawanisi, and M. B. Al Sawaf, “Characteristics of tidal discharge and phase difference at a tidal channel junction investigated using the fluvial acoustic tomography system,” *Water*,

- vol. 11, no. 4, p. 857, 2019.
- [11] M. Razaz, K. Kawanisi, I. Nistor, and S. Sharifi, “An acoustic travel time method for continuous velocity monitoring in shallow tidal streams,” *Water Resour. Res.*, vol. 49, no. 8, pp. 4885–4899, 2013.
- [12] C. Xiao, K. Kawanisi, and M. B. Al Sawaf, “Suspended particulate matter concentration in response to tidal hydrodynamics in a long mesotidal floodway,” *Estuar. Coast. Shelf Sci.*, vol. 233, 2020, doi: 10.1016/j.ecss.2019.106525.
- [13] P. Matte, D. A. Jay, and E. D. Zaron, “Adaptation of classical tidal harmonic analysis to nonstationary tides, with application to river tides,” *J. Atmos. Ocean. Technol.*, vol. 30, no. 3, pp. 569–589, 2013.
- [14] D.-G. Yoo, N.-H. Koo, H.-Y. Lee, B.-Y. Kim, Y.-J. Kim, and S. Cheong, “Acquisition, processing and interpretation of high-resolution seismic data using a small-scale multi-channel system: an example from the Korea Strait inner shelf, south-east Korea,” *Explor. Geophys.*, vol. 47, no. 4, pp. 341–351, 2016.
- [15] M. Soltaniasl, K. Kawanisi, and M. Razaz, “Investigation of Salinity Variability in a Small Multi-Channel Estuary,” *J. Japan Soc. Civ. Eng. Ser. B1 (Hydraulic Eng.)*, vol. 68, no. 4, p. I_265-I_270, 2012.
- [16] A. J. F. Hoitink and D. A. Jay, “Tidal river dynamics: Implications for deltas,” *Rev. Geophys.*, vol. 54, no. 1, pp. 240–272, 2016.
- [17] S. Murphy and G. Voulgaris, “Identifying the role of tides, rainfall and seasonality in marsh sedimentation using long-term suspended sediment concentration data,” *Mar. Geol.*, vol. 227, no. 1–2, pp. 31–50, 2006.
- [18] M. Baeye, M. Fettweis, G. Voulgaris, and V. Van Lancker, “Sediment mobility in response to tidal and wind-driven flows along the Belgian inner shelf, southern North Sea,” *Ocean Dyn.*, vol. 61, no. 5, pp. 611–622, 2011.
- [19] E. Garel, L. Pinto, A. Santos, and Ó. Ferreira, “Tidal and river discharge forcing upon water and sediment circulation at a rock-bound estuary (Guadiana estuary, Portugal),” *Estuar. Coast. Shelf Sci.*, vol. 84, no. 2, pp. 269–281, 2009.
- [20] J. R. French, H. Burningham, and T. Benson, “Tidal and meteorological forcing of suspended sediment flux in a muddy

- mesotidal estuary,” *Estuaries and Coasts*, vol. 31, no. 5, p. 843, 2008.
- [21] S. Arndt, J. Vanderborght, and P. Regnier, “Diatom growth response to physical forcing in a macrotidal estuary: Coupling hydrodynamics, sediment transport, and biogeochemistry,” *J. Geophys. Res. Ocean.*, vol. 112, no. C5, 2007.
- [22] V. N. de Jonge, H. M. Schuttelaars, J. E. E. van Beusekom, S. A. Talke, and H. E. de Swart, “The influence of channel deepening on estuarine turbidity levels and dynamics, as exemplified by the Ems estuary,” *Estuar. Coast. Shelf Sci.*, vol. 139, pp. 46–59, 2014.
- [23] N. Geleynse, J. E. A. Storms, D.-J. R. Walstra, H. R. A. Jagers, Z. B. Wang, and M. J. F. Stive, “Controls on river delta formation; insights from numerical modelling,” *Earth Planet. Sci. Lett.*, vol. 302, no. 1–2, pp. 217–226, 2011.
- [24] J. Z. Shi, “Tidal resuspension and transport processes of fine sediment within the river plume in the partially-mixed Changjiang River estuary, China: a personal perspective,” *Geomorphology*, vol. 121, no. 3–4, pp. 133–151, 2010.
- [25] Y. Yuan, H. Wei, L. Zhao, and W. Jiang, “Observations of sediment resuspension and settling off the mouth of Jiaozhou Bay, Yellow Sea,” *Cont. Shelf Res.*, vol. 28, no. 19, pp. 2630–2643, 2008.
- [26] D. A. Jay and E. P. Flinchem, “Interaction of fluctuating river flow with a barotropic tide: A demonstration of wavelet tidal analysis methods,” *J. Geophys. Res. Ocean.*, vol. 102, no. C3, pp. 5705–5720, 1997.
- [27] T. Kukulka and D. A. Jay, “Impacts of Columbia River discharge on salmonid habitat: 1. A nonstationary fluvial tide model,” *J. Geophys. Res. Ocean.*, vol. 108, no. C9, 2003.
- [28] N. Leonardi, A. S. Kolker, and S. Fagherazzi, “Interplay between river discharge and tides in a delta distributary,” *Adv. Water Resour.*, vol. 80, pp. 69–78, 2015.
- [29] F. A. Buschman, A. J. F. Hoitink, M. Van Der Vegt, and P. Hoekstra, “Subtidal flow division at a shallow tidal junction,” *Water Resour. Res.*, vol. 46, no. 12, 2010.
- [30] M. G. Sassi, A. J. F. Hoitink, B. de Brye, B. Vermeulen, and E. Deleersnijder, “Tidal impact on the division of river discharge over

- distributary channels in the Mahakam Delta,” *Ocean Dyn.*, vol. 61, no. 12, pp. 2211–2228, 2011.
- [31] Z. Yang and T. Khangaonkar, “Modeling tidal circulation and stratification in Skagit River estuary using an unstructured grid ocean model,” *Ocean Model.*, vol. 28, no. 1–3, pp. 34–49, 2009.
- [32] M. G. Sassi, A. J. F. Hoitink, B. de Brye, and E. Deleersnijder, “Downstream hydraulic geometry of a tidally influenced river delta,” *J. Geophys. Res. Earth Surf.*, vol. 117, no. F4, 2012.
- [33] H. H. G. Savenije, *Salinity and tides in alluvial estuaries*. Gulf Professional Publishing, 2005.
- [34] W. R. Geyer and P. MacCready, “The estuarine circulation,” *Annu. Rev. Fluid Mech.*, vol. 46, pp. 175–197, 2014.
- [35] H. Wu, J. Zhu, and B. H. Choi, “Links between saltwater intrusion and subtidal circulation in the Changjiang Estuary: A model-guided study,” *Cont. Shelf Res.*, vol. 30, no. 17, pp. 1891–1905, 2010.
- [36] M. A. J. de Nijs, J. D. Pietrzak, and J. C. Winterwerp, “Advection of the salt wedge and evolution of the internal flow structure in the Rotterdam Waterway,” *J. Phys. Oceanogr.*, vol. 41, no. 1, pp. 3–27, 2011.
- [37] D. H. Schoellhamer, “Factors affecting suspended-solids concentrations in south San Francisco Bay, California,” *J. Geophys. Res. Ocean.*, vol. 101, no. C5, pp. 12087–12095, 1996.
- [38] W. Munk, P. Worcester, and C. Wunsch, “Ocean acoustic tomography, Cambridge Univ,” *Pr.*, Cambridge UK, 1995.
- [39] A. Kaneko, G. Yuan, N. Gohda, and I. Nakano, “Optimum design of the ocean acoustic tomography system for the Sea of Japan,” *J. Oceanogr.*, vol. 50, no. 3, pp. 281–293, 1994.
- [40] K. Kawanisi, M. Razaz, J. Yano, and K. Ishikawa, “Continuous monitoring of a dam flush in a shallow river using two crossing ultrasonic transmission lines,” *Meas. Sci. Technol.*, vol. 24, no. 5, p. 55303, 2013.
- [41] X.-H. Zhu, Y. Takasugi, M. Nagao, and E. Hashimoto, “Diurnal cycle of sound scatterers and measurements of turbidity using ADCP in Beppu Bay,” *J. Oceanogr.*, vol. 56, no. 5, pp. 559–565, 2000.
- [42] A. Kaneko, X.-H. Zhu, and M.-H. Radenac, “Diurnal variability and

- its quantification of subsurface sound scatterers in the western equatorial Pacific,” *Oceanogr. Lit. Rev.*, vol. 44, no. 4, p. 300, 1997.
- [43] A. M. Ferreira, M. Martins, and C. Vale, “Influence of diffuse sources on levels and distribution of polychlorinated biphenyls in the Guadiana River estuary, Portugal,” *Mar. Chem.*, vol. 83, no. 3–4, pp. 175–184, 2003.
- [44] G. Voulgaris and S. T. Meyers, “Temporal variability of hydrodynamics, sediment concentration and sediment settling velocity in a tidal creek,” *Cont. Shelf Res.*, vol. 24, no. 15, pp. 1659–1683, 2004.
- [45] D. H. Schoellhamer, “Variability of suspended-sediment concentration at tidal to annual time scales in San Francisco Bay, USA,” *Cont. Shelf Res.*, vol. 22, no. 11–13, pp. 1857–1866, 2002.
- [46] S. A. Moore, J. Le Coz, D. Hurther, and A. Paquier, “Using multi-frequency acoustic attenuation to monitor grain size and concentration of suspended sediment in rivers,” *J. Acoust. Soc. Am.*, vol. 133, no. 4, pp. 1959–1970, 2013.
- [47] F. G. Latosinski, R. N. Szupiany, C. M. García, M. Guerrero, and M. L. Amsler, “Estimation of concentration and load of suspended bed sediment in a large river by means of acoustic Doppler technology,” *J. Hydraul. Eng.*, vol. 140, no. 7, p. 4014023, 2014.
- [48] J. J. Duncker, K. K. Johnson, and J. B. Sharpe, “Bathymetric survey of Lake Calumet, Cook County, Illinois,” US Geological Survey, 2015.
- [49] M. G. Moura, V. S. Quaresma, A. C. Bastos, and P. Veronez, “Field observations of SPM using ADV, ADP, and OBS in a shallow estuarine system with low SPM concentration—Vitória Bay, SE Brazil,” *Ocean Dyn.*, vol. 61, no. 2–3, pp. 273–283, 2011.
- [50] K. Kawanisi and S. Yokosi, “Characteristics of suspended sediment and turbulence in a tidal boundary layer,” *Cont. Shelf Res.*, vol. 17, no. 8, pp. 859–875, 1997.
- [51] M. Razaz and K. Kawanisi, “Tide-driven controls on maximum near-bed floc size in a partially-mixed estuary,” *J. Japan Soc. Civ. Eng. Ser. B1 (Hydraulic Eng.)*, vol. 68, no. 4, p. I_7-I_12, 2012.
- [52] W. Van Leussen and J. Dronkers, “Physical processes in estuaries: An introduction,” in *Physical processes in estuaries*, Springer,

- 1988, pp. 1–18.
- [53] M. Razaz, K. Kawanisi, and I. Nistor, “Tide-driven controls on maximum near-bed floc size in a tidal estuary,” *J. Hydro-environment Res.*, vol. 9, no. 3, pp. 465–471, 2015.
- [54] K. Kawanisi, T. Yokoyama, M. Razaz, S. Fukuoka, and T. Abe, “Observations of Effect of Wind on Sediment Transport in Ohtagawa Estuary,” in *Proceedings of Coastal Engineering, JSCE*, 2008, vol. 55, pp. 386–390.
- [55] P. D. Thorne and D. M. Hanes, “A review of acoustic measurement of small-scale sediment processes,” *Cont. Shelf Res.*, vol. 22, no. 4, pp. 603–632, 2002.
- [56] D. H. Schoellhamer, “Singular spectrum analysis for time series with missing data,” *Geophys. Res. Lett.*, vol. 28, no. 16, pp. 3187–3190, 2001.
- [57] R. Vautard, P. Yiou, and M. Ghil, “Singular-spectrum analysis: A toolkit for short, noisy chaotic signals,” *Phys. D Nonlinear Phenom.*, vol. 58, no. 1–4, pp. 95–126, 1992.
- [58] I. Jalón-Rojas, S. Schmidt, and A. Sottolichio, “Evaluation of spectral methods for high-frequency multiannual time series in coastal transitional waters: advantages of combined analyses,” *Limnol. Oceanogr. Methods*, vol. 14, no. 6, pp. 381–396, 2016.
- [59] K. Kawanisi, M. Bahrainimotlagh, M. B. Al Sawaf, and M. Razaz, “High-frequency streamflow acquisition and bed level/flow angle estimates in a mountainous river using shallow-water acoustic tomography,” *Hydrol. Process.*, vol. 30, no. 13, pp. 2247–2254, 2016.
- [60] M. B. Al Sawaf, K. Kawanisi, J. Kagami, M. Bahreinimotlagh, and M. M. Danial, “Scaling characteristics of mountainous river flow fluctuations determined using a shallow-water acoustic tomography system,” *Phys. A Stat. Mech. its Appl.*, vol. 484, pp. 11–20, 2017.
- [61] M. Razaz, “Turbulence structures and transport processes of suspended sediment in the Ōta diversion channel.” Hiroshima University, doctoral thesis, 2010.
- [62] H. Burchard, R. D. Hetland, E. Schulz, and H. M. Schuttelaars, “Drivers of residual estuarine circulation in tidally energetic estuaries: Straight and irrotational channels with parabolic cross

- section,” *J. Phys. Oceanogr.*, vol. 41, no. 3, pp. 548–570, 2011.
- [63] J. Ge *et al.*, “Formation of concentrated benthic suspension in a time-dependent salt wedge estuary,” *J. Geophys. Res. Ocean.*, vol. 123, no. 11, pp. 8581–8607, 2018.
- [64] M. Razaz and K. Kawanishi, “Long-term observations of flow and suspended sediment in a tidally-dominated estuary,” in *Proceedings Of Coastal Dynamics 2009: Impacts of Human Activities on Dynamic Coastal Processes (With CD-ROM)*, World Scientific, 2009, pp. 1–11.
- [65] R. J. Uncles, J. A. Stephens, and R. E. Smith, “The dependence of estuarine turbidity on tidal intrusion length, tidal range and residence time,” *Cont. Shelf Res.*, vol. 22, no. 11–13, pp. 1835–1856, 2002.
- [66] N. Wang, K. Chen, P. Lu, Y. Chen, J. Zhang, and Y. Wang, “Impact of a water–sediment regulation scheme on the hydrodynamics and sediment conditions in the Sheyang Estuary,” *Estuar. Coast. Shelf Sci.*, vol. 218, pp. 349–358, 2019.
- [67] M. E. Scully and C. T. Friedrichs, “The influence of asymmetries in overlying stratification on near-bed turbulence and sediment suspension in a partially mixed estuary,” *Ocean Dyn.*, vol. 53, no. 3, pp. 208–219, 2003.
- [68] I. Grabemann, R. J. Uncles, G. Krause, and J. A. Stephens, “Behaviour of turbidity maxima in the Tamar (UK) and Weser (FRG) estuaries,” *Estuar. Coast. Shelf Sci.*, vol. 45, no. 2, pp. 235–246, 1997.
- [69] K. Kawanishi, T. Tsutsui, S. Nakamura, and H. Nishimaki, “Influence of tidal range and river discharge on transport of suspended sediment in the Ohta flood-way,” *J. Hydrosoci. Hydraul. Eng.*, vol. 24, no. 1, pp. 1–9, 2006.
- [70] L. L. Brothers, D. F. Belknap, J. T. Kelley, and C. D. Janzen, “Sediment transport and dispersion in a cool-temperate estuary and embayment, Saco River estuary, Maine, USA,” *Mar. Geol.*, vol. 251, no. 3–4, pp. 183–194, 2008.
- [71] F. A. Buschman, A. J. F. Hoitink, M. Van Der Vegt, and P. Hoekstra, “Subtidal water level variation controlled by river flow and tides,” *Water Resour. Res.*, vol. 45, no. 10, 2009.

- [72] A. E. Hill and A. J. Souza, “Tidal dynamics in channels: 2. Complex channel networks,” *J. Geophys. Res. Ocean.*, vol. 111, no. C11, 2006.
- [73] M. Razaz, K. Kawanisi, A. Kaneko, and I. Nistor, “Application of acoustic tomography to reconstruct the horizontal flow velocity field in a shallow river,” *Water Resour. Res.*, vol. 51, no. 12, pp. 9665–9678, 2015.
- [74] H. Zheng, H. Yamaoka, N. Gohda, H. Noguchi, and A. Kaneko, “Design of the acoustic tomography system for velocity measurement with an application to the coastal sea,” *J. Acoust. Soc. Japan*, vol. 19, no. 3, pp. 199–210, 1998.
- [75] H. Yamaoka *et al.*, “Coastal acoustic tomography system and its field application,” *IEEE J. Ocean. Eng.*, vol. 27, no. 2, pp. 283–295, 2002.
- [76] X.-H. Zhu, A. Kaneko, Q. Wu, C. Zhang, N. Taniguchi, and N. Gohda, “Mapping tidal current structures in Zhitouyang Bay, China, using coastal acoustic tomography,” *IEEE J. Ocean. Eng.*, vol. 38, no. 2, pp. 285–296, 2013.
- [77] X.-H. Zhu *et al.*, “Measurement of tidal and residual currents and volume transport through the Qiongzhou Strait using coastal acoustic tomography,” *Cont. Shelf Res.*, vol. 108, pp. 65–75, 2015.
- [78] C. Zhang *et al.*, “High-precision measurement of tidal current structures using coastal acoustic tomography,” *Estuar. Coast. Shelf Sci.*, vol. 193, pp. 12–24, 2017.
- [79] K. Yamaguchi *et al.*, “A continuous mapping of tidal current structures in the Kanmon Strait,” *J. Oceanogr.*, vol. 61, no. 2, pp. 283–294, 2005.
- [80] Z.-N. Zhu, X.-H. Zhu, and X. Guo, “Coastal tomographic mapping of nonlinear tidal currents and residual currents,” *Cont. Shelf Res.*, vol. 143, pp. 219–227, 2017.
- [81] J.-H. Park and A. Kaneko, “Computer simulation of coastal acoustic tomography by a two-dimensional vortex model,” *J. Oceanogr.*, vol. 57, no. 5, pp. 593–602, 2001.
- [82] R. Pawlowicz, B. Beardsley, and S. Lentz, “Classical tidal harmonic analysis including error estimates in MATLAB using T_TIDE,” *Comput. Geosci.*, vol. 28, no. 8, pp. 929–937, 2002.

- [83] T. Conroy, D. A. Sutherland, and D. K. Ralston, “Estuarine exchange flow variability in a seasonal, segmented estuary,” *J. Phys. Oceanogr.*, vol. 50, no. 3, pp. 595–613, 2020.
- [84] M. Chen *et al.*, “Mapping Current Fields in a Bay Using a Coast-Fitting Tomographic Inversion,” *Sensors*, vol. 20, no. 2, p. 558, 2020.
- [85] C. T. Friedrichs and D. G. Aubrey, “Non-linear tidal distortion in shallow well-mixed estuaries: a synthesis,” *Estuar. Coast. Shelf Sci.*, vol. 27, no. 5, pp. 521–545, 1988.
- [86] H. Cai, H. H. G. Savenije, and M. Toffolon, “Linking the river to the estuary: influence of river discharge on tidal damping,” *Hydrol. Earth Syst. Sci.*, vol. 18, no. 1, p. 287, 2014.
- [87] S. Lu *et al.*, “Propagation of tidal waves up in Yangtze Estuary during the dry season,” *J. Geophys. Res. Ocean.*, vol. 120, no. 9, pp. 6445–6473, 2015.
- [88] K. Kästner and A. J. F. Hoitink, “Flow and suspended sediment division at two highly asymmetric bifurcations in a river delta: Implications for channel stability,” *J. Geophys. Res. Earth Surf.*, vol. 124, no. 10, pp. 2358–2380, 2019.
- [89] J. H. Simpson, J. Brown, J. Matthews, and G. Allen, “Tidal straining, density currents, and stirring in the control of estuarine stratification,” *Estuaries*, vol. 13, no. 2, pp. 125–132, 1990.
- [90] X. Wei, G. P. Schramkowski, and H. M. Schuttelaars, “Salt dynamics in well-mixed estuaries: Importance of advection by tides,” *J. Phys. Oceanogr.*, vol. 46, no. 5, pp. 1457–1475, 2016.
- [91] M. M. Bowen and W. R. Geyer, “Salt transport and the time-dependent salt balance of a partially stratified estuary,” *J. Geophys. Res. Ocean.*, vol. 108, no. C5, 2003.
- [92] J. A. Lerczak, W. R. Geyer, and R. J. Chant, “Mechanisms driving the time-dependent salt flux in a partially stratified estuary,” *J. Phys. Oceanogr.*, vol. 36, no. 12, pp. 2296–2311, 2006.
- [93] P. MacCready, “Toward a unified theory of tidally-averaged estuarine salinity structure,” *Estuaries*, vol. 27, no. 4, pp. 561–570, 2004.
- [94] E. Zhang, H. H. G. Savenije, H. Wu, Y. Kong, and J. Zhu, “Analytical solution for salt intrusion in the Yangtze Estuary,

- China,” *Estuar. Coast. Shelf Sci.*, vol. 91, no. 4, pp. 492–501, 2011.
- [95] K. Haralambidou, G. Sylaios, and V. A. Tsihrintzis, “Salt-wedge propagation in a Mediterranean micro-tidal river mouth,” *Estuar. Coast. Shelf Sci.*, vol. 90, no. 4, pp. 174–184, 2010.
- [96] J.-H. Moon, N. Hirose, J.-H. Yoon, and I.-C. Pang, “Offshore detachment process of the low-salinity water around Changjiang Bank in the East China Sea,” *J. Phys. Oceanogr.*, vol. 40, no. 5, pp. 1035–1053, 2010.
- [97] M. L. Becker, R. A. Luettich Jr, and M. A. Mallin, “Hydrodynamic behavior of the Cape Fear River and estuarine system: A synthesis and observational investigation of discharge–salinity intrusion relationships,” *Estuar. Coast. Shelf Sci.*, vol. 88, no. 3, pp. 407–418, 2010.
- [98] C. Zhang, A. Kaneko, X. Zhu, and N. Gohda, “Tomographic mapping of a coastal upwelling and the associated diurnal internal tides in Hiroshima Bay, Japan,” *J. Geophys. Res. Ocean.*, vol. 120, no. 6, pp. 4288–4305, 2015.
- [99] H. Huang, Y. Guo, Z. Wang, Y. Shen, and Y. Wei, “Water Temperature Observation by Coastal Acoustic Tomography in Artificial Upwelling Area,” *Sensors*, vol. 19, no. 12, p. 2655, 2019.
- [100] J. Park and A. Kaneko, “Assimilation of coastal acoustic tomography data into a barotropic ocean model,” *Geophys. Res. Lett.*, vol. 27, no. 20, pp. 3373–3376, 2000.
- [101] H. Medwin, “Speed of sound in water: A simple equation for realistic parameters,” *J. Acoust. Soc. Am.*, vol. 58, no. 6, pp. 1318–1319, 1975.
- [102] J. Xuan, D. Huang, F. Zhou, X. Zhu, and X. Fan, “The role of wind on the detachment of low salinity water in the Changjiang Estuary in summer,” *J. Geophys. Res. Ocean.*, vol. 117, no. C10, 2012.
- [103] R. J. Uncles and J. A. Stephens, “The effects of wind, runoff and tides on salinity in a strongly tidal sub-estuary,” *Estuaries and Coasts*, vol. 34, no. 4, pp. 758–774, 2011.
- [104] L. Li, J. Zhu, H. Wu, and Z. Guo, “Lateral saltwater intrusion in the North Channel of the Changjiang Estuary,” *Estuaries and coasts*, vol. 37, no. 1, pp. 36–55, 2014.
- [105] P. Xue *et al.*, “Saltwater intrusion into the Changjiang River: A

- model-guided mechanism study,” *J. Geophys. Res. Ocean.*, vol. 114, no. C2, 2009.
- [106] K. Kawanisi, M. Razaz, and M. B. Motlagh, “Monitoring flow rate and salinity intrusion in a tidal floodway using fluvial acoustic tomography,” in *Proceeding of the 36th IAHR World Congress*, 2015, pp. 6634–6641.
- [107] M. B. Al Sawaf, K. Kawanisi, and C. Xiao, “Measuring Low Flowrates of a Shallow Mountainous River Within Restricted Site Conditions and the Characteristics of Acoustic Arrival Times Within Low Flows,” *Water Resour. Manag.*, vol. 34, no. 10, pp. 3059–3078, 2020.